

Helmholtz Institute Jena

Annual Report 2011

Contents

<u>Introduction</u>	7
<u>High power laser development</u>	
A new pump profile homogenization method for the POLARIS-amplifier A4	11
S. Keppler, A. Kessler, A. Sävert, M. Hornung, M. Hellwing, J. Hein, and M. C. Kaluza	
A closed-loop adaptive optics system for POLARIS	12
M. Hornung, R. Bödefeld, S. Keppler, A. Sävert, J. Hein, and M. C. Kaluza	
POLARIS contrast improvement by post pulse suppression	13
S. Keppler, M. Hornung, R. Bödefeld, A. Kessler, M. Hellwing, M. Kahle, F. Schorcht, J. Hein, M. C. Kaluza	
Development of the pump laser for the contrast boosting stage at PHELIX	14
V. Bagnoud, J. Fils, F. Wagner, T. Gottschall, J. Limpert, C. João, J. Körner, J. Hein, T. Stöhlker	
Creating circularly polarized light with a fully reflective wave-plate assembly	15
B. Aurand, S. Kuschel, C. Rödel, M. Wünsche, H. Zhao, O. Jäckel, M. Kaluza, M. Heyer, F. Wunderlich, G. G. Paulus, T. Kühl	
Laser diode performance under cryogenic conditions	16
M. Kahle, J. Hein, J. Körner, H. Liebetrau, R. Seifert, D. Klöpfel, M. Kaluza	
Concept and current status for a cryogenic CPA-burst mode-laser	17
H. Liebetrau, J. Hein, M. Kahle, J. Körner, R. Seifert, D. Klöpfel, M. C. Kaluza	
Current state and first results of the 5th POLARIS amplifier	18
A. Kessler, F. Schorcht, M. Hellwing, S. Keppler, M. Hornung, R. Bödefeld, A. Sävert, J. Körner, J. Hein, and M. C. Kaluza	
A new class of few-cycle parametric amplifiers and their application	19
J. Rothhardt, S. Hädrich, S. Demmler, M. Krebs, T. Eidam, F. Stutzki, F. Jansen, C. Jauregui, J. Limpert, A. Tünnermann	
Coherent combination of femtosecond fiber amplifiers for performance scaling	20
A. Klenke, E. Seise, S. Demmler, J. Rothhardt, J. Limpert, A. Tünnermann	

High repetition rate Optical Parametric Chirped Pulse Amplifier system for FEL applications 21

F. Tavella, A. Willner, M. Schulz, R. Riedel, M. Prandolini, A. Hage, M. A. Seise, T. Gottschall, S. Düsterer, J. Rossbach, J. M. Drescher, J. Limpert, A. Tünnermann, J. Feldhaus

Laser particle acceleration

Absorption of circularly polarized laser pulses in near-critical plasmas 25

J. Polz, A. P. L. Robinson, R. M. G. M. Trines, and M. C. Kaluza

A cryogenic liquid micro droplet source for laser plasma interactions 27

J. Polz, R. A. Costa Fraga, A. Kalinin, M. Kühnel, D. C. Hochhaus, A. A. Schottelius, P. Neumayer, R. E. Grisenti, and M. C. Kaluza

Water micro droplets for laser ion acceleration 28

J. Polz, A. Sävert, M. Schwab, M. Reuter, A. K. Arunachalam, O. Jäckel, S. Herzer, D. Klöpfel, W. Ziegler, F. Ronneberger, B. Beleites, A. Gopal, A. P. L. Robinson, R. A. Costa Fraga, A. Kalinin, R. E. Grisenti, G. G. Paulus, and M. C. Kaluza

Implications for the electron distribution from the stationary hydrodynamic model of one-dimensional plasma expansion into vacuum 29

T. Kiefer and T. Schlegel

Radiation pressure assisted ion acceleration using multi-component targets 30

S. Kuschel, B. Aurand, C. Rödel, S. Herzer, J. Polz, A. E. Paz, O. Jäckel, P. Gibbon, A. Karmakar, B. Elkin, G. G. Paulus, T. Kühl, and M. C. Kaluza

Tuning of a laser wake field accelerator: Recent experiments and simulations 32

A. Sävert, S. P. D. Mangles, M. Schnell, M. Reuter, M. Nicolai, O. Jäckel, C. Spielmann, M. C. Kaluza

Photon and particle spectroscopy and diagnostics: Experiments and theory

Laser driven x-ray parametric amplification in neutral gases: a new brilliant light source in the XUV 35

J. Seres, E. Seres, B. Ecker, B. Landgraf, D. Hochhaus, D. Zimmer, V. Bagnoud, B. Aurand, B. Zielbauer, T. Kühl, and C. Spielmann

Towards seeded X-ray lasers at PHELIX 36

B. Ecker, E. Oliva, B. Aurand, D. C. Hochhaus, T. Kühl, P. Neumayer, H. Zhao, B. Zielbauer, K. Cassou, S. Daboussi, O. Guilbaud, S. Kazamias, D. Ros, T. Le, and P. Zeitoun

Efficiency of relativistic surface harmonic generation	37
J. Bierbach, A. Galestian Pour, C. Rödel, O. Jäckel, M. C. Kaluza, M. Zepf, and G. G. Paulus	
Polarization effects detected with the high purity x-ray polarimeter	39
K. S. Schulze, B. Marx, I. Uschmann, E. Förster, G. G. Paulus, and T. Stöhlker	
Properties of the bremsstrahlung linear polarization in polarized electron-atom collisions	40
R. Martin, R. Barday, J. Enders, Y. Fritzsche, U. Spillmann, A. Surzhykov, G. Weber, V. A. Yerokhin, Th. Stöhlker	
PEBSI - a Monte Carlo simulator for polarized-electron bremsstrahlung	41
G. Weber, R. Martin, A. Surzhykov, M. Yasuda, V. A. Yerokhin, Th. Stöhlker	
Time resolved x-ray diffraction on indium antimonide (InSb) crystals	42
S. Höfer, T. Kämpfer, I. Uschmann, E. Förster	
Laser-excited acoustical phonons in germanium probed by ultrashort pulses from a laser-driven x-ray diode	43
T. Kämpfer, K. S. Schulze, I. Uschmann, S. Höfer, R. Löttsch, E. Förster	
Optical Coherence Tomography using broad-bandwidth XUV and soft x-ray radiation	44
S. Fuchs, A. Blinne, C. Rödel, U. Zastra, V. Hilbert, M. Wünsche, J. Bierbach, E. Förster, G. G. Paulus	
Laser Driven X-ray Radiography on Warm Dense Matter	46
D. C. Hochhaus, B. Aurand, M. Basko, B. Ecker, T. Kühl, T. Ma, F. Rosmej, B. Zielbauer, D. Zimmer, and P. Neumayer	
X-Ray Diffraction Topography of optical waveguides written in YAG single crystals using fs-laser	47
J. Kräußlich, H. Marschner, E. Förster, J. Siebenmorgen, T. Calmano, and G. Huber	
Generation of picosecond narrow bandwidth X-ray pulses from a Laser-Thomson-Backscattering source at HZDR	48
A. Irman, A. Jochmann, S. Trotsenko, U. Lehnert, J. P. Couperus, M. Kuntzsch, A. Wagner, A. Debus, H. P. Schlenvoigt, K. D. Ledingham, T. E. Cowan, R. Sauerbrey, Th. Stöhlker, and U. Schramm	
Nonlinear Thomson scattering of ultraintense laser light on relativistic electrons with the account for radiation friction	49
T. Schlegel and V. T. Tikhonchuk	

Vacuum polarization in inhomogeneous fields	50
N. Roessler, H. Gies	
The photon polarization tensor in a homogeneous external field revisited	51
B. Döbrich, F. Karbstein	
New constraints on minicharged particles from tunneling of the 3rd kind	52
B. Döbrich, H. Gies, N. Neitz, F. Karbstein	
Relativistic ionization dynamics of highly charged ions	53
P. Wustelt, T. Rathje, A. M. Saylor, D. Hoff, S. Trotsenko, Th. Stöhlker, G. G. Paulus	
A dedicated Penning trap for studies with particles in extreme laser fields	54
M. Vogel, W. Quint, Th. Stöhlker, G.G. Paulus	
Lifetime measurement of the 2^3P_0 state in He-like uranium	55
R. Reuschl, T. Gassner, U. Spillmann, A. Bräuning-Demian, A. Ananyeva, H. Beyer, K.-H. Blumenhagen, W. Chen, S. Hagmann, M. Hegewald, P. Indelicato, M. Schwemlein, S. Toleikis, M. Trassinelli, S. Trotsenko, D. Winters, N. Winters, and Th. Stöhlker	
The High Voltage Electron Beam Ion Trap (S-EBIT) for SPARC	56
Y. Ke, I. Orban, M. Hobein, S. Tashenov, S. Trotsenko, S. Mahmood, O. Kamalou, A. Safdar, Th. Stöhlker, H. Zhang, and R. Schuch	
SPARC experiments in the high-energy storage ring HESR	57
Th. Stöhlker, C. Dimopoulou, A. Dolinskii, T. Katayama, Yu. A. Litvinov, R. Maier, D. Prasuhn, M. Steck, R. Schuch, H. Stockhorst	
An x-ray laser beamline to the ESR	58
V. Bagnoud, B. Ecker, U. Eisenbarth, S. Götte, Th. Kühl, P. Neumayer, Th. Stöhlker, D. F. A. Winters, B. Zielbauer	
Cryogenic Current Comparator for FAIR	59
R. Geithner, F. Kurian, R. Neubert, W. Vodel, and P. Seidel	
<u>Publications</u>	60

Introduction

The Helmholtz Institute Jena (HI-Jena) is located on the campus of the Friedrich Schiller University Jena as a branch of the GSI Helmholtz Center for Heavy Ion Research with the University and the Helmholtz Centers DESY and HZDR as partner institutions. The institute's mission is excellence in fundamental and applied research, in particular research on structure of matter by means of high-power lasers, accelerated particles, and x-ray science. Emphasis is placed on research at the interface of particle accelerators and lasers in order to harvest well-established and yet to discover synergies.

Within the three years following its foundation in July 2009, the Helmholtz Institute Jena has matured to a very productive research institute, and has established a link between the Helmholtz Centers running accelerator based research programs and the local university groups specialized on laser physics and x-ray science. As a consequence of this strategic position, significant progress of its research activities has been realized during the last year as documented by the present annual report.

Figure 1 displays the general structure of the scientific program pursued within the Helmholtz Institute Jena. During recent years, the five research areas as defined initially at the foundation of the institute have been merged into the three main pillars.

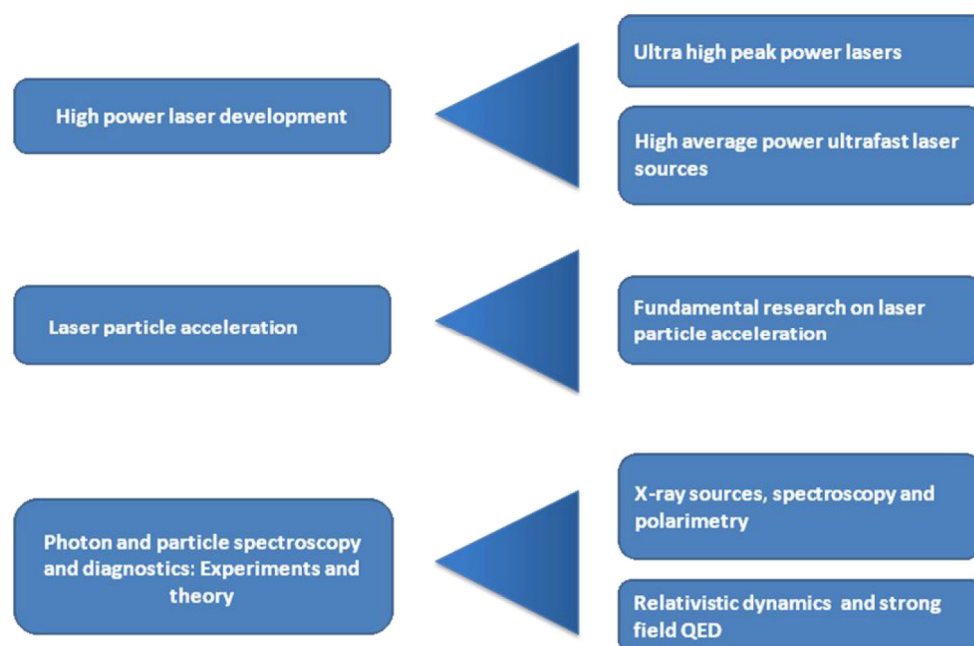


Fig. 1: *The five research areas initially defined during the foundation phase of the institute have been merged into the three central research fields, strongly interlinked.*

The strong overlap between the three research pillars displayed in Fig. 1 fosters strong collaborations within the institute itself and also combines with the expertise from different Helmholtz research centers (GSI, DESY and HZDR). Thus the institute provides valuable support for the planning and development of the two large-scale accelerator projects for electrons and ions, the European XFEL and the International FAIR facilities. In addition it has assumed a significant role for the ongoing research programs at the partner institutions.

A very significant milestone in developing the institute was achieved in 2011 with the new building at Fröbelstieg 3 (see the cover page). The reconstruction of this building was completed in October 2011 and provides about 1200 m² of office, seminar, and laboratory space. The extensive reconstruction of the building was financed with the help of the “Konjunkturpaket II” and a substantial contribution from the Friedrich Schiller University and allows the various research groups of the institute to work closely together.

Substantial progress was achieved also in the recruitment of leading researchers for the institute. Prof. Dr. Matt Zepf, Queens University Belfast, was appointed as the leader of a research group concentrating on “relativistic laser particle interaction“. In addition the appointment for the W3 theory position, attached to the institute and the physics faculty of Friedrich-Schiller-University is progressing well. Finally, the W3 appointments of Prof. Dr. Malte Kaluza as well as of Prof. Dr. Thomas Stöhlker at the FSU have been finalized.

Finally, the new Research School for Advanced Photon Science of the Helmholtz Institute has been established for the benefit of young researchers who will be receiving a broadly based, high level education and will contribute to the scientific program. With this background a further increase of the already highly visible scientific output of the institute can be secured, also providing the necessary high level of input and support for the final planning and preparation phase of the international research projects FAIR and XFEL.

High power laser development

A new pump profile homogenization method for the POLARIS - amplifier A4

S. Keppler¹, A. Kessler^{1,2}, A. Sävert¹, M. Hornung^{1,2}, M. Hellwing¹, J. Hein^{1,2} and M.C. Kaluza^{1,2}

¹Institute of Optics and Quantum Electronics, FSU Jena, Germany; ²Helmholtz-Institute Jena, Germany

High intensity laser systems have high requirements on the beam quality. On the one hand, a maximum energy has to be deposited within a certain beam diameter, without exceeding the damage threshold, and on the other hand, the focusability has to be as good as possible. Since the beam profile is mainly determined by the amplifier's pump profile, a perfect flat-top profile would be desirable. The pump profile of the POLARIS amplifier A4 is composed out of 40 different spots of 40 diode stacks with different spot characteristics in size and intensity, thus each single spot has to be adjusted to its very individual position. We developed a new adjustment method for the homogenization of the pump profile, which leads to a higher accuracy and a significantly simplified adjustment, since intermediate steps during the iteration process can be skipped.

For the characterization of the pump profile, the pumped glass was imaged onto a CCD, which was equipped with an edge-filter. This filter blocked the pump light at 940nm while the fluorescence at 1030nm was transmitted. Additionally, the exposure time was reduced to its minimum and the profile was measured directly after the pump pulse of the diode stacks had ended. With all these constraints it was possible to calculate the overall pump profile by the sum of the recorded images of the individual spots. Furthermore, the different diode stacks are arranged symmetrically on both sides of the amplifier medium [1]. For symmetry reasons it is important to optimize the spots from each side separately. Thus two times 20 spots had to be optimized to a desired pump profile, but the overall pump profile has to be very smooth as well. For a best possible result the starting arrangement of the 20 spots is very important. It is determined by the arrangement of the pump optics [1] and includes the spots to be placed along an inner and an outer circle and a fixed single spot in the middle. Due to the limited acceptance area of the last focusing lens [1] a maximum displacement area of each spot has to be defined.

For the optimization of the individual spot positions, the LabView (National Instruments) based „adaptive strategy“-algorithm of the LAB2 [2] package was applied. This routine is a genetic algorithm that varies the query parameters (genes, e.g. the spot positions) randomly within the defined query limits (e.g. the allowed displacement area) and thus generates mutations. A second program evaluates these mutations with respect to a defined figure of merit, and returns the best attempts (elites), which are used in the next generation. As the figure of merit we used the root mean square of the difference between the sum of the individual pump spots and the desired pump profile defined by a target function. The optimization is stopped when the difference between successive generations becomes negligibly small. As the target function a

4th-order Super-Gaussian with a FWHM of 18mm has proven to be suitable. Additionally we introduced a weighting function, which rates the squared difference between the current mutation and the target function in the center higher than in the outer region. As a result of this algorithm, we get the calculated best approximation to the desired pump profile and the position of the individual spots, which could then be adjusted afterwards.

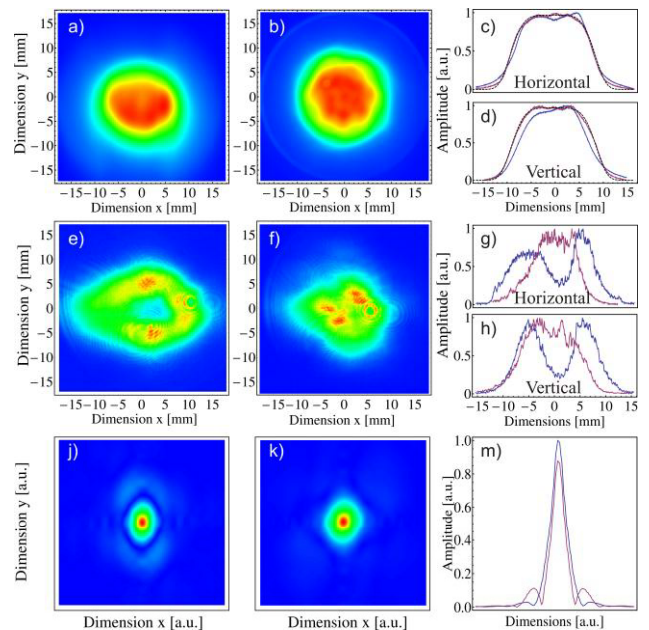


Figure 1: Pump profile a) before and b) after the optimization with the new algorithm; c) horizontal and d) vertical lineout of (a) (purple), (b) (blue) and the target function (dashed); beam profile d) before and e) after the optimization routine; f) horizontal and g) vertical lineout of (d) (purple) and (e) (blue); calculated far-field j) before and k) after the optimization routine; m) lineout of (j) (purple) and (k) (blue) at an angle of 45° to the horizontal.

With this new method, we reached an accuracy of the pump-profile of $\pm 2\%$ (PV) (Fig. 1 (a) – (d)) within 2 actually set iterations. It represents the intrinsic limitation due to the size and number of the pump-spots. As a further result, the amplified laser beam profile (Fig. 1 (e) – (h)) was improved by turning the doughnut shape into a more top-hat like shape, which was proven to provide a 15% higher intensity (Fig 1(j) – (m)) of the POLARIS laser system for experiments.

References

- [1] M. Siebold, S. Podleska, J. Hein, R. Bödefeld, M. Hornung, R. Sauerbrey, IOQ Annual Report, 2004
- [2] B. Schmidt, M. Hacker, G. Stonrawa, T. Feurer LAB2 - a virtual fs laser lab, <http://www.lab2.de>

A closed-loop adaptive optics system for POLARIS

M. Hornung^{1,2}, R. Bödefeld^{1,2}, S. Keppler², A. Sävert², J. Hein^{1,2} and M. C. Kaluza^{1,2}

¹Helmholtz-Institute Jena, ²Institute of Optics and Quantum Electronics Jena.

The peak intensity of a high-power short-pulse laser system is one of most important parameters for performing laser-matter experiments. Here we report on the implementation of a closed-loop adaptive optics system in the diode-pumped multi-TW POLARIS laser. This system is able to optimize and flatten the wavefront of the amplified and compressed laser pulses in order to decrease the focal spot size and increase the energy contained inside the focal spot.

Experimental Setup

The adaptive optics system consists of a deformable mirror which is located under vacuum conditions behind the pulse compressor and a wavefront-sensor with an imaging telescope in front of the target chamber. A detailed overview of the POLARIS architecture is given in [1].

The deformable mirror has a 170-mm clear aperture with 150 mm active area and 48 actuators. The device is based on the bimorph mirror technology and was manufactured from *Active Optics NightN Ltd.* (Russia, [2]).

To measure the wavefront of the amplified and compressed laser pulses a commercially available high-resolution lateral shearing interferometer is used (SID4HR, *Phasics S.A.* (France) [3]). The laser pulses are imaged with an 18-times size reduction telescope onto the interferometer. For this purpose, the leakage through a mirror of the transport beamline in front of the target chamber is used. The wavefront-sensor is connected to a PC and able to communicate with the deformable mirror in order to realize the wavefront-correction in a closed-loop configuration.

The final focussing optic of the POLARIS laser system is currently a silver coated $f/2$ off-axis parabola ($f=300$ mm). In order to observe and align the focal spot in the POLARIS target chamber a focal-spot diagnostic consisting of an $f/2$ -lens ($f=100$ mm), a high-quality vacuum window and a high-dynamic CCD was used.

Optimization Strategy

Our strategy to realize the highest possible peak-intensity with a given near-field distribution of the laser-pulses is to generate an optimized wavefront behind the focussing parabola. With this goal-setting we correct the wavefront of the amplified laser pulses for all aberrations originating in the laser amplifiers, transport beamline-mirrors and the final focussing optics.

Once pulses with an optimized wavefront behind the focussing parabola are available, the measured wavefront of the aforementioned leakage-pulses in front of the target chamber are set as reference for further operation of the laser system. This reference includes all significant opti-

cal components and is set as a target wavefront for the aberration correction in daily operation.

To achieve an undistorted wavefront behind the focussing parabola the wavefront sensor was placed inside the focal-spot diagnostic where the beam-diameter and the divergence of the laser pulses fit to the wavefront-sensor. The beam diameter of the laser pulses has been adjusted to fill the whole aperture of the beamline and the pulses have been attenuated massively in the front-end of the laser system to avoid optical damage of the wavefront sensor. In this configuration the adaptive optics system is able to generate laser pulses with an optimized wavefront behind the focussing parabola. These pulses can then be used to set the reference in front of the target chamber.

Results & Conclusions

To characterize the quality of the focussed laser pulses we use the spot area where the intensity is higher than 50% of the peak intensity and the included energy (q-factor). For a spatial Gaussian shape this q-factor could theoretically be as high as 0.5.

Before the installation of the adaptive optics system a focal spot size of $13.0 \mu\text{m}^2$ and a q-factor of 0.29 were achieved. This was possible by detuning the parabola to compensate for low-order wavefront aberrations. After commissioning and characterisation of the adaptive optics system we currently achieve a focal spot size of $8.7 \mu\text{m}^2$ with a q-factor of 0.31 (cf. Figure 1.).

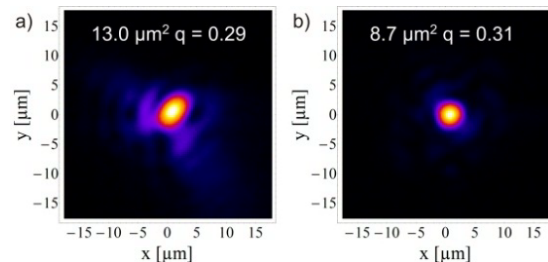


Figure 1: Focal spot of POLARIS before (a) and after (b) installation of the adaptive optics system.

Under the assumption of identical laser parameters, this means that the peak intensity of the POLARIS laser system could be increased by more than 60% due to the installation of the adaptive optics system.

References

- [1] M. Hornung et al., “Temporal pulse control of a Multi-10-TW diode-pumped Yb:Glass laser”, *Applied Physics B*, 101, March 2010, p. 93-101.
- [2] www.nightn.ru
- [3] www.phasics.fr

POLARIS contrast improvement by postpulse suppression

S. Keppler¹, M. Hornung^{1,2}, R. Bödefeld^{1,2}, A. Kessler^{1,2}, M. Hellwing¹, M. Kahle^{1,2}, F. Schorcht^{1,2}, J. Hein^{1,2} and M.C. Kaluza^{1,2}

¹Institute of Optics and Quantum Electronics, FSU Jena, Germany; ²Helmholtz-Institute Jena, Germany

High-intensity short-pulse laser which are used in laser-plasma experiments require a very high temporal intensity contrast (TIC). Intense prepulses as well as a quasi-continuous energy level over a certain duration (ASE) have to be reduced to a minimum [1]. In 2008, Didenko *et. al.* [2] described the generation of prepulses due to the nonlinear phase (B-Integral) accumulated by the pulses in the amplifiers in the presence of postpulses, therefore the complete suppression of prepulses as well as postpulses becomes important.

Postpulses are mainly generated by double reflection of the pulses at the surfaces of thin plan parallel optics, e.g. halfwave-plates (HWPs). Anti-reflection (AR) coatings with a typical residual reflectivity of 0.6% cannot improve such TIC of the postpulses below 4×10^{-5} .

Each regenerative amplifier (RA) of the POLARIS system [3] is built as a ring cavity. It therefore typically contains a 1.2mm thick HWP for pulse switching. Additionally, the plan-parallel windows of the Pockels cells (PCs) and the multi-order waveplates (MOWPs) used for spectral filtering were identified as sources of postpulses and hence also of potential prepulse. Due to the generation of these postpulses with every round trip, a TIC of up to 2×10^{-3} at the respective temporal positions of 12ps, 24ps and 35ps after the main pulse was measured (see Fig. 1).

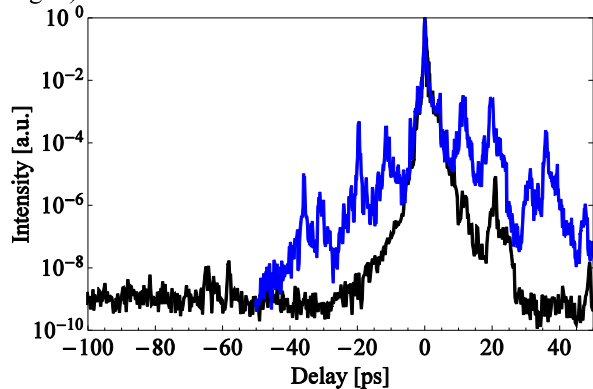


Figure 1: Intensity contrast of the POLARIS front-end before (blue) and after (black) the postpulse suppression by the implementation of the polarization rotation device, the spectrally shaping mirrors and the wedged Pockels cell windows.

In order to suppress the postpulses of the HWP in each RA, we adapted a polarization rotation device (PRD) for the application in high-power lasers [4]. Due to the purely reflective principle of the polarization rotation using three special mirrors, this configuration generates no postpulses, provides a higher damage threshold and a broad band capability. Furthermore it is easily scalable for larger

beam diameters and its spectral reflectivity as well as the acceptance angle depend on the coating design only.

To avoid postpulses due to the MOWP we use newly designed spectrally shaping mirrors (SSMs), which compensates the spectral dependency of the gain as depicted in Fig. 2. The entire spectral compensation is provided by the combination of two mirrors, carefully aligned to the design angle of incidence of 46° . The resulting bandwidth of the POLARIS front-end, including the first two amplifiers, with the SSMs was measured to 15nm. By exchanging plane parallel PC windows with wedged ones this additional source of postpulses could also be avoided. Finally the seed pulse of each RA was adjusted in size and divergence with respect to the cavity mode. Herewith the seed energy could be maximized and thus the ASE-level further improved.

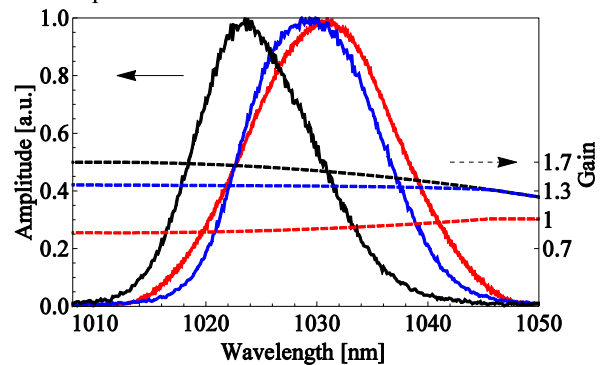


Figure 2: Injected (red) and amplified spectrum of the first regenerative amplifier with (blue) and without (black) spectrally shaping mirrors. The gain characteristics are shown by the dashed lines in the corresponding colour. The red dashed line represents the calculated spectral reflectivity of one mirror.

In conclusion, the prepulses at -12ps, -24ps and -35ps could be suppressed completely as shown in Fig. 1. Furthermore the ASE of the POLARIS laser system was improved to a level of 10^{-9} and no prepulses above a level of 10^{-8} are present even in the extended measured temporal range of up to 3.5ns.

References

- [1] M. C. Kaluza, J. Schreiber, M.I.K. Santala, G.D. Tsakiris, K. Eidmann, J. Meyer-ter-Vehn, K.J. Witte, *Phys. Rev. Lett.* 93 (2004) 045003
- [2] N.V. Didenko, A.V. Konyashchenko, A.P. Lutsenko, S.Yu. Tenyakow, *Opt. Express*, 16 (2008) 3178
- [3] S. Keppler, R. Bödefeld, M. Hornung, A. Sävert, J. Hein and M.C. Kaluza, *Appl. Phys. B*, 104 (2011) 11
- [4] S. Keppler, M. Hornung, R. Bödefeld, M. Kahle, J. Hein and M.C. Kaluza, to be submitted to *Opt. Lett.*

Development of the pump laser for the contrast boosting stage at PHELIX*⁺

V. Bagnoud^{1,2}, J. Fils¹, F. Wagner³, T. Gottschall^{2,4}, J. Limpert^{2,4}, C. João⁶, J. Körner⁵, J. Hein^{2,5} and T. Stöhlker^{1,2}

¹GSI Darmstadt; ²Helmholtz Institute Jena; ³IKP TU Darmstadt; ⁴Institute of Applied Physics, Jena; ⁵Institute of Optics and Quantum Electronics, Jena; ⁶Instituto Superior Técnico, Lisbon;

The temporal contrast of laser pulses is a concern in nowadays high-intensity lasers and ways to improve it are being investigated around the world. For petawatt-class high-energy lasers, this area of research suffers from additional constraints due to the use of glass as an amplification medium. This requires specific developments that the HI-Jena has undertaken and will demonstrate on the PHELIX laser used as a test-bed facility. This strategy is being strongly supported by the PHELIX and Plasma Physics Program Advisory Committee (PPAC) that met in November 2010 and recommends the effort to improve the temporal contrast of the PHELIX short pulse be strengthened.

The temporal contrast of short laser pulses is affected by many sources that must be addressed independently. The PHELIX team together with HI-Jena has boiled this theme down to three projects that address different aspects of the temporal contrast issue. The main project deals with the reduction of the sub-nanosecond and nanosecond temporal noise by use of an ultrafast parametric amplifier (uOPA project)¹. This project was started in 2010 at HI-Jena and was continuing in collaboration with the PHELIX team. The main milestone for 2011 has been the delivery at GSI of the laser amplifier necessary for the uOPA. The amplifier is made of a fibre pre-amplifier and a laser-diode-pumped regenerative amplifier.

Delivery of the laser fibre amplifier to GSI

The fibre amplifier is the first step to generate millijoule-level pump pulses necessary for the uOPA module. It consists of a first fibre used as wavelength shifter that is seeded by pulses from the PHELIX short pulse oscillator. This first stage is necessary to deliver light pulses centred at 1040 nm and it takes advantage of the broad spectral width of the Mira laser: about 5% of its energy lies in a 5-nm wide band around 1040 nm. The frequency shifting fibre is pumped by a 0.7 W laser diode and runs in saturation mode to deliver about 170 mW at 72 MHz that are enough for seeding the second stage. The second stage is run at a lower repetition rate of 1 MHz and uses a double-cladding Ytterbium-doped fibre that outputs ~ 500 nJ pulses. The setup has been built at the IAP in Jena and used at the IOQ for the development of the regenerative amplifier. It was finally delivered to GSI in May 2011.

At GSI, the setup has been re-engineered to meet the PHELIX standards and it is now a turn-key well documented device synchronized to PHELIX. In particular, the

* The acronym stands for Petawatt High Energy Laser for heavy Ion eXperiments.

+ This work is supported by LASERLAB, the Helmholtz Institute Jena and GSI

need of a 1 MHz trigger signal puts strong requirements on the PHELIX timing system that has been updated to deliver that signal.

Initial results with the regenerative amplifier

The parts necessary for the regenerative amplifier have been received early in the year. The regenerative amplifier is based on Ytterbium-doped crystals that can operate as close to 1054 nm as possible. It was decided to test Yb:KGW and Yb:KYW that have broad emission bands and can be run at 1040 nm. The Ytterbium-doped materials are pumped by a commercial 2kW laser diode module working a 940 nm.

The amplifier is built as a ring cavity seeded by the first fibre amplification stage. Because gain is generally low in Ytterbium-doped materials, the first amplifier stage provides a significant gain and allows reducing the number of round trips in the amplifier significantly. The regenerative amplifier delivers up to 10 mJ, which is the expected energy and aside from spectral modulation performs satisfactorily.

This amplifier has been delivered and installed at PHELIX in the spring. When the fibre amplifier was successfully coupled to PHELIX, a dedicated machine beamtime has been granted to complete the characterization of the amplifier. In particular, the pulse compression after the regenerative amplifier was investigated; and one could find for instance that the volume Bragg grating (Opti-grate, USA) used in the setup can run at high (10 mJ) input energy, a level much higher that reported before. However, the pulse compression also showed that the spectral modulations appearing during the amplification significantly degrade the pulse shape and must be addressed. That work will continue in 2012.

Conclusion

The pump laser for the uOPA project has been delivered and successfully installed at PHELIX. Following this step a first test run of the uOPA has been done to gain insight on issues like gain and timing drifts that have been reported by others. During this run, gains of 10^4 have been measured. The next steps include the demonstration of effect of the uOPA on the temporal contrast and early commissioning experiments.

References

- ¹ C. Dorrer et al., Optics Lett. **32**, 2143 (2007)

Creating circularly polarized light with a fully reflective wave-plate assembly

B. Aurand^{1,2,3,4}, S. Kuschel^{1,5}, C. Rödel^{1,5}, M. Wünsche^{1,5}, H. Zhao⁶, O. Jäckel^{1,5}, M. C. Kaluza^{1,5}, M. Heyer⁷, F. Wunderlich⁷, G. G. Paulus^{1,5}, and T. Kuehl^{1,2,3,4}

¹Helmholtz Institute Jena; ²GSI Helmholtz Center for heavy ion research GmbH; ³Johannes Gutenberg University;

⁴EMMI ExtreMe Matter Institute; ⁵Friedrich Schiller University; ⁶Institut of Modern Physics; ⁷Layertec GmbH

Introduction

Circularly polarized light is typically created using a quarter-wave plate made of mica, quartz glass or other crystalline material. However, this method is not generally applicable to ultra-high intensity short-pulse lasers due to nonlinear effects, the damage threshold of the material, and the fact that ultra-thin wave-plates have a chromaticity that prevents their usage for broadband laser sources. An alternative way is the use of reflective elements using the polarization dependent phase shift on the surface. We developed and tested a system which can easily be implemented in the laser system enabling to switch the polarization between linear- and circular- polarized within seconds [1, 2].

Setup

Dielectric coatings are a well-known technique to produce e.g. mirrors with a high reflectivity. Advanced designing of the layer stack allows an influence of the reflected phase behavior. Within an optimization process we designed a mirror inducing a phase shift of 90° between the s- and the p- polarized component for a broad wavelength range of (800 ± 40) nm having a reflectivity of 98%. Benchmarking this mirror we realized an ellipticity of $(98.3 \pm 0.6)\%$ for a 10 cm diameter beam. This method will be well applicable even for ultra-short pulses in the range of a few femtoseconds, since the calculated group-delay-dispersion (GDD) amounts to only 40 fs^2 . By implementing three mirrors specially designed without a phase shift, we developed in a second step a reflective wave-plate assembly (Fig. 1), which can be implemented in a laser-system creating circular polarized light without major changes.

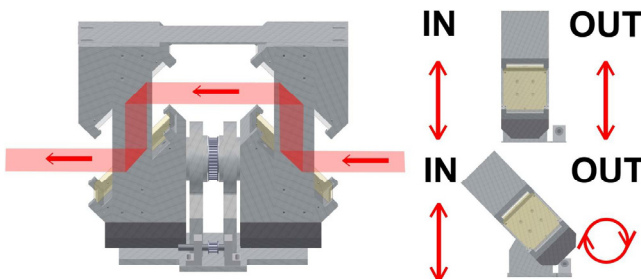


Figure 1: : Setup of the reflective wave-plate using four mirrors. Depending on the polarization of the assembly, linear polarized light stays linear polarized, or becomes circular polarized.

Experiment

All tests of the single PSM and the reflective wave-plate assembly were done on a Ti-Sapphire laser-system delivering pulses of 27 fs and a multi-kilohertz repetition rate. The bandwidth of the system $[(800 \pm 50) \text{ nm}]$ is within the design range of the device. Using polarizing beam splitters we measured the angular dependent intensity variation and calculated the field distribution in front and behind the mirror. The maximum ellipticity for the full setup was found to be $(90.0 \pm 0.1)\%$ (Fig. 2). The pulse broadening of a 27 fs pulse in the PSM and the full reflective wave-plate assembly was smaller than the measurement accuracy of 1 fs of the autocorrelator used in the experiment, which is in agreement with the calculated value GDD of 40 fs^2 . Comparison of the spectrum in front and behind the assembly showed no changes due to interferences in the complex layer design. Another big advantage of the reflective design is the high damage threshold, measured to be $5 \cdot 10^{12} \text{ W/cm}^2$, which is a factor of 400 higher compared to typical transmissive quartz retardation-plates [3].

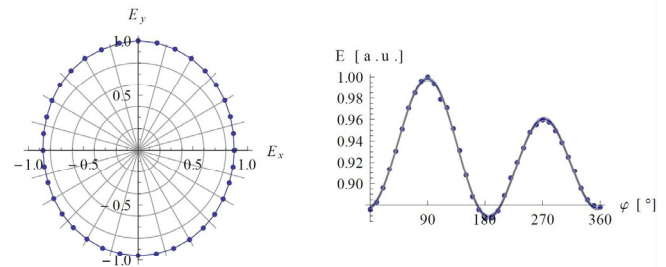


Figure 2: Field distribution for the maximum achievable ellipticity of the full system is $(90.0 \pm 0.1)\%$.

Outline

Phase modulation systems based on this idea are proposed to be implemented into the new POLARIS system at Jena University, and will be used for a proposed experiment at the PHELIX laser facility at GSI in the next year

References

- [1] B. Aurand, *et al.* Optics Express, Vol. 19, Issue 18, 17151, (2011).
- [2] B. Aurand, *et al.* Review of Scientific Instruments, Vol. 83, Issue 3, 036104, (2012).
- [3] A. A. Said, *et al.* Opt., Vol. 34, Issue. 18, 3374-3376, (1995)

Laser Diode Performance under Cryogenic Conditions

M. Kahle^{1,2}, J. Hein^{1,2}, J. Körner², H. Liebetrau², R. Seifert^{1,2}, D. Klöpfel^{1,2}, M. Kaluza^{1,2}

¹Helmholtz-Institut Jena, Germany

²Institute of Optics and Quantum Electronics, Jena, Germany

Currently, the main investment for large scale diode pumped systems like POLARIS are the pump diodes. Every measure to rise their efficiency becomes important. Cooling semiconductor lasers to low temperature as in the early days of microchips could be an interesting way to go. Here we investigated the performance of standard laser diodes under vacuum and cryogenic cooling conditions.

For this purpose laser diode samples emitting at 940nm were supplied by Jenoptik Laserdiode GmbH. The diodes were mounted on top of a cooling finger inside a vacuum chamber. Controlling the operating current we recorded the voltage, energy output and time-resolved spectra for conditions between room temperature/normal pressure and -188°C/vacuum. From these data the lasing threshold, the slope efficiency, the temperature-wavelength-shift and the energy distribution in the pulses were extracted.

Figure 1 shows an example of the time resolved pulse spectrum. The wavelength shifts occurring during the pulse are caused by the temperature rise in the semiconductor material. Since the temperature dependent output wavelength of the diode is determined by the different baseplate temperatures, this pulse-measurement is an indirect measure for the p-n-junction temperature increase. For a 300A, 1ms pulse at -184°C baseplate temperature a wavelength shift of 4nm during the pulse was measured. This corresponds to a temperature increase of 22K. For comparison the wavelength shift at room temperature is 4,7nm but the temperature increase is only 14K. This is due to the fact that the relation between temperature and wavelength is not constant over the temperature range.

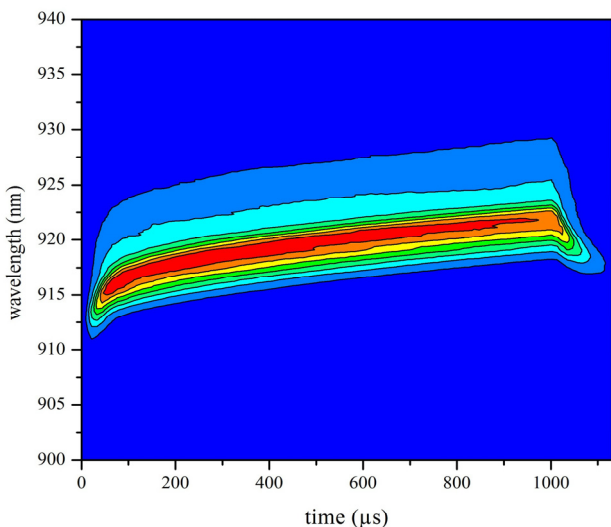


Figure 1: time-resolved spectrum of a laser diode pulse

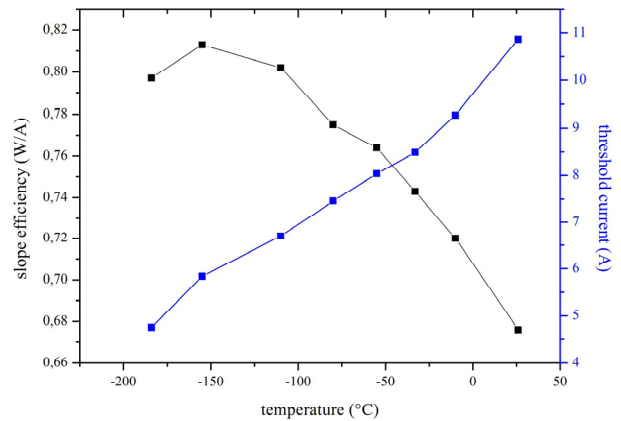


Figure 2: slope efficiency and threshold current of a laser diode as a function of temperature

Furthermore, it could be observed that the necessary voltage for a fixed current value increased with decreasing temperature. This could be explained by a decreasing number of charge carriers. At higher currents and lower temperatures the necessary voltage was not constant during the pulse despite an actively stabilized current. This indicates that heating changes the electrical resistance.

A main result was that the lasing threshold could be suppressed by lowering the temperature. Additionally the slope efficiency rises significantly. These measurements are plotted in fig 2. Here the slope efficiency is given as a relative change because we were not able to collect all radiation from the diode. Just by cooling the diode the pulse energy was increased by about 15%. The voltage change of only 5% indicates an electrical-to-optical efficiency improvement of about 10% at maximum.

For the lowest investigated temperature of -187°C the performance is reduced again. So far we could not identify the reason, but we suspect this effect to be caused by the lack of charge carriers.

As a side result, the ambient pressure did not seem to have any effect on the operation of the laser diodes. Moreover since degradation of semiconductor lasers are known to depend strongly on temperature an additional benefit may be gained.

Conclusion and Outlook

Laser diodes were operated at low temperatures and vacuum conditions which led to a higher efficiency and increased pulse energy. Choosing such operating conditions may result in a substantial benefit for diode pumped large scale lasers. Further investigations are needed in order to prove the assumption of an impact on diode laser life time.

Concept and current status for a cryogenic CPA-burst mode-laser *

H. Liebetrau², J. Hein², M. Kahle^{1,2}, J. Koerner², R. Seifert¹, D. Kloepfel², and M.C. Kaluza^{1,2}

¹Helmholtz-Institute Jena, Germany; ²Institute of Optics and Quantum Electronics, Jena, Germany

Motivation

Burst-mode lasers are capable of combining the advantages of high-power- and those of high-energy-femtosecond lasers, providing pulses at a medium energy but a high repetition rate within the burst. Hence, this approach offers advanced options in many application, e.g. higher doses of radiation or synchronization with particle beams at higher energies per pulse. Currently we are performing design studies and preliminary research for realizing such a system.

System design

The complete system will consist of a CPA-frontend delivering stretched pulses around 100 ps at a repetition rate of 1 MHz. After a first amplification (S0 in Fig.1), a Pockels-cell, which can switch at the pulse repetition rate, will generate bursts at a repetition rate of 10 Hz, each burst consisting of several hundred pulses (variable). Followed by two cryogenically cooled amplifier stages (S1 and S2 in Fig.1) and a compression stage the laser will provide bursts containing a total energy of 5 J at a repetition rate of 10 Hz.

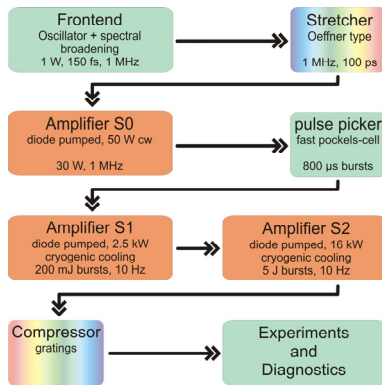


Figure 1: Sketch of the complete burst-mode laser system.

Amplifier development

The relay imaging implemented in all amplifiers allows multiple material passes with only a few optical parts. This scheme also allows to reduce the footprints of the amplifier stages resulting in a table-top laser system. As the laser material (Yb:CaF₂) is cooled down to liquid nitrogen temperature by means of vibration-reduced microscope cryostats in

the amplifiers S1 and S2, it need to be placed in a vacuum environment. The cooling is required to improve the spectral features (absorption, gain etc.) of the laser material [1]. Additionally to avoid distortions by air, e.g. turbulences, the complete last stage S2 will be operated under vacuum, where the imaging optics will be set up in a vertical assembly yielding a rather small footprint (see Fig.2).

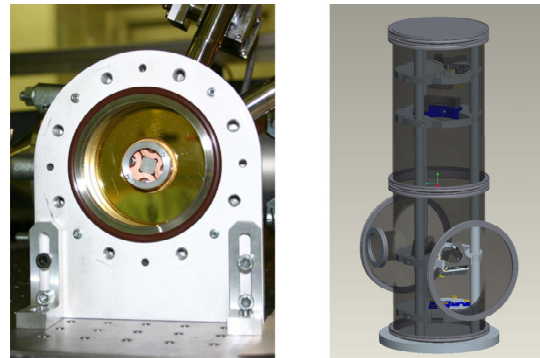


Figure 2: cryostat for amplifier S1 and design of vertical setup for S2

Current status

So far the oscillator, a preliminary stretcher and the second amplifier stage S1 are installed. First amplification tests were done using Yb:YAG and Yb:FP-glass as laser material in the second amplifier (see Table 1.).

seed	Yb:YAG	Yb:FP-glass
40 μJ	70 mJ	10 mJ
5 nm	1 nm	4 nm
	10 Hz	0.2 Hz

Table 1: burst energy, bandwidth and repetition rate for the first test of S1, burst length 500 μs

Further amplification was limited by self-lasing in Yb:YAG and thermal lensing of Yb:FP-glass at low temperatures. Both effects are expected to be much smaller in CaF₂ and more seed energy for the second stage will decrease the necessary gain.

References

- [1] J. Koerner et al., "Temperature dependent measurement of absorption and emission crosssections for various Yb³⁺ doped laser materials", Proc.SPIE 8080, 808003(2011)

* project "OPTIMAL" supported by TMBWK under contract No: B715-09012 and B514-09050

Current State and First Results of the 5th POLARIS Amplifier

A. Kessler¹, F. Schorcht¹, M. Hellwing², S. Keppler², M. Hornung¹, R. Bödefeld¹,
A. Sävert¹, J. Körner¹, J. Hein^{1,2} and M. C. Kaluza^{1,2}

¹Helmholtz-Institut-Jena, ²Friedrich-Schiller-Universität-Jena, Germany

POLARIS [1] has the goal to reach laser output energies of 100 J and pulse durations of 150fs. For this reason the output energy of the 4th POLARIS amplifier A4 (10J) has to be increased at least by factor of 10. This will be achieved using the 5th POLARIS Amplifier A5. So far, we have installed the pump system and the fully motorized beam line. Furthermore, we developed a Control System for convenient and safe operation.

Setup of A5

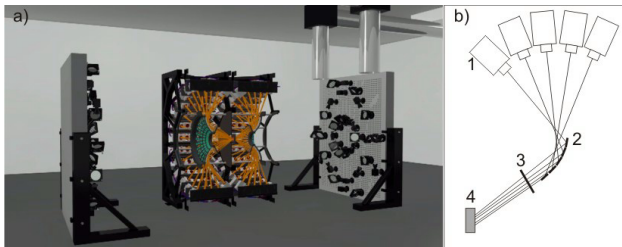


Figure 1: a) Artistic view of the A5 pump module in the middle and two vertical optical tables on the sides b) Pump ray geometry. Laser diode stacks (1), adjustment mirrors (2), cylindrical lens (3), laser medium (4)

A5 comprises a pump module in the middle and two vertical tables for the beam-line on the sides (Fig. 1). Currently 120 solid state laser diode stacks (Jenoptic GmbH) with 2.5kW optical power each and a central wave length of 940nm are installed. The capacity for a total of 240 stacks is available. The maximal pump pulse duration is 2.6ms, resulting in a maximum pump energy of 1560 J. Currently nine passes of the multi-pass configuration have been installed. After A4 the laser beam diameter is 20mm (FWHM). To match the diameter of the pump region in the amplifying medium (35mm FWHM), the beam diameter has to be increased by a factor of 1.73. We use 6" laser mirrors (Layertec GmbH) motorized by piezo adjustment motors (Newport).

Control System (CS)

Our CS is based on CS-Framework [2] developed by GSI. Realizing a CS means to merge POLARIS specific add-ons like CS-Framework classes for physical devices which are used in the system, operation sequences and human machine interfaces with CS-framework. For the pump system we developed the device classes for power supplies, pump spot adjustment mirrors, air humidity control and water cooling of the pump diodes. We defined sequences for daily routines like start up, shut down and automatic alignment of the pump spot positions. For the A5-beamline we developed device classes for the

Newport piezo motors, home made step motor controllers, motorized filter wheels and GigE-Vision cameras. Via user interface the operator can control images of each laser pass through the amplifiers for each laser shot, calibrate adjustment motors and get recommendations for their positions. Since the position of the piezo motors is not reproducible, the calibration values depend on direction and distance of the mirror displacement. To overcome this disadvantage we designed an adjustment routine that selects appropriate calibration values for the momentary beam deviation.

Results for homogenization of pump profile

To form a homogeneous, super-gaussian distribution of the pump light, the spots from the 120 individual pump diodes have to be arranged. This task has 360 free parameters, for each spot two translational parameters and one for the intensity. We developed a new routine based on an evolutionary algorithm “adaptive strategy” from the software package LAB2 [3] to find a parameter set. After two iterations we reach a peak to value variation below 2% (Fig. 2). Using a similar routine we also optimized the pump profile of the amplifier A4. [4].

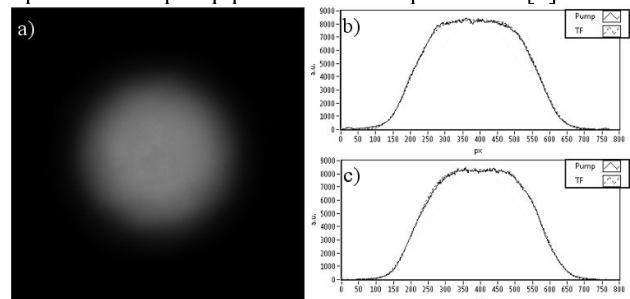


Figure 2: a) A5-Pumpprofile, b) horizontal and c) vertical lineouts of pump area (solid) and target function (dashed)

Laser material and gain measurement

We use a 3% Yb³⁺-doped 18mm thick CaF₂-crystal and a 3% Yb³⁺-doped FP-glass with 70mm diameter. During a first gain test with the CaF₂-crystal we have achieved a gain factor of 3. This result matches well the calculated gain of 2.75.

- [1] M.Hornung, PhD thesis, Uni-Jena 2010.
- [2] <http://wiki.gsi.de/cgi-bin/view/CSframework>
- [3] <http://www.lab2.de>
- [4] S. Keppler, A. Kessler, A. Sävert, annual report, HI-Jena 2011.

A new class of few-cycle parametric amplifiers and their application

J. Rothhardt^{1,2}, S. Hädrich^{1,2}, S. Demmler², M. Krebs², T. Eidam^{1,2}, F. Stutzki², F. Jansen², C. Jauregui², J. Limpert^{1,2}, and A. Tünnermann^{1,2}

¹Helmholtz Institute, Jena, Germany; ²Institute of Applied Physics, Jena, Germany

There have been a number of remarkable scientific results enabled by the now mature technology of attoscience. This great success has been made possible by the availability of controlled light fields with few-cycle pulse duration. In this regard optical parametric chirped-pulse amplification (OPCPA) has been considered to be the most interesting approach due to the possibility to achieve high repetition rate (high average power) operation.

Here we present amplification of a full optical octave of bandwidth in a single-color pumped optical parametric amplifier. Beyond this we present average power scaling to unprecedented average power levels.

Pump Laser

A crucial part in achieving new parameters in OPCPA system is the pump laser. It is used to transfer energy to a weak, but broadband signal via nonlinear interaction in a suitable crystal and, therefore, its performance determines the possible output. The experiments are focused on high average powers and repetition rates. For this purpose, fiber chirped-pulse amplification (FCPA) systems seem to be a promising tool [1]. However, the scalability of high energy FCPAs has been hindered by the onset of mode instabilities. The development of novel large-pitch fibers has greatly enhanced the average power of such systems [2]. By employing these fibers it became possible to extract compressed pulses with 200 μJ , 500 fs pulses at repetition rates of up to 1 MHz (200 W).

Octave-Spanning Amplification

A first requirement for the OPCPA system is a broadband seed signal. This is generated by exploiting self-phase modulation in a specially designed photonic-crystal fiber (PCF) that allows to generate a smooth, stable and coherent supercontinuum spanning more than an octave of bandwidth. It has been shown that it can be compressed near its Fourier limit and only 1.3 cycles duration by using a phase shaping element [3]. Timing synchronization between the pump laser and the signal is achieved by using the same oscillator for continuum generation and FCPA seeding. The latter one is achieved by frequency shifting the oscillator output in another PCF with lowest possible timing jitter [4].

The broad amplification bandwidth is achieved by using very short crystals and high pump intensities. This allows for a sufficiently high gain even for wavelengths, which are not perfectly phase-matched. Figure 1 shows the amplified spectrum, which covers more than an octave of bandwidth.

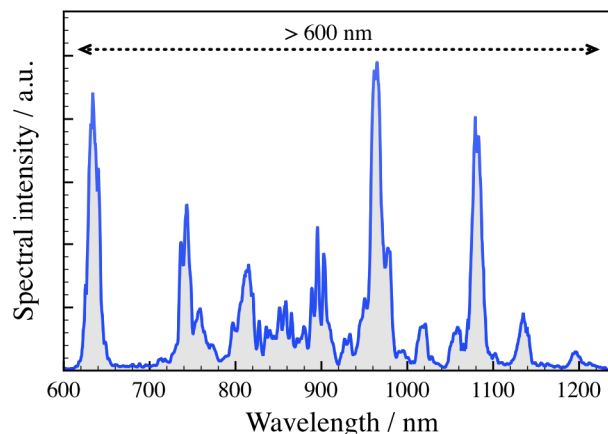


Figure 1: Spectrum after amplification in a two stage optical parametric amplifier covering a complete optical octave of bandwidth.

So far it was possible to compress the pulses to 5 fs, which corresponds to only 1.7 optical cycles at 880 nm central wavelength. The pulse energy of the compressed pulses was higher than 20 μJ . This corresponds to a pump to signal conversion efficiency of almost 20%. At 1 MHz repetition rate this leads to 22 W of average power for the few-cycle pulses, which is a record value for few-cycle laser system. In addition, the carrier envelope phase (CEP) stability of the system was measured to be as good as 150 mrad on a short (1 s) and 450 mrad on a long (95 s) time scale.

High Harmonic Generation

A possible application for such laser system is high harmonic generation (HHG). This process allows to generate isolated attosecond pulses (IAP) when driven with pulses with less than two-cycles in duration. Consequently, the extremely short CEP stable pulses of fiber laser pumped OPCPA systems hold promise to enable IAP generation at unprecedented repetition rates in the near future [6].

References

- [1] S. Hädrich et al., *Opt. Lett.* **36**, 313-315 (2011).
- [2] F. Stutzki et al., *Opt. Lett.* **36**, 689-691 (2011).
- [3] S. Demmler et al., *Opt. Express* **19**, 20151-20158 (2011).
- [4] J. Rothhardt et al., to be published in *JOSA B*
- [5] J. Rothhardt et al., to be published in *Opt. Express*
- [6] M. Krebs et al., to be presented at High Intensity Lasers and High Field Phenomena, March 2012

Coherent combination of femtosecond fiber amplifiers for performance scaling

A. Klenke, E. Seise, S. Demmler, J. Rothhardt, J. Limpert, A. Tünnermann^{1,2}

¹Helmholtz Institute Jena, Germany; ²Institute of Applied Physics, Friedrich-Schiller-University Jena, Germany

In the last decade, a lot of progress has been made in developing technologies to amplify high energy ultrashort pulses at high repetition rates and, consequently to high average powers. Several optical amplifier architectures have been developed to achieve this goal, including the thin disk laser, the innoslab laser and the fiber laser. However, all these architectures are characterized by their own limitations such as thermal effects, nonlinearities or damage threshold. Overcoming these limitations can be extremely challenging. Therefore, it is advantageous to consider additional concepts to scale the performance of such laser systems.

Coherent combination of amplifiers is already widely known to scale the output power of fiber amplifiers in the continuous wave regime. This approach is now extended to ultrashort pulses (see fig 1.). In this case, not only the scaling of the average power is beneficial, but also the improvement of the pulse energy and therefore the peak power. The following sections present theoretical and experimental results that have been obtained with the coherent combination technique.

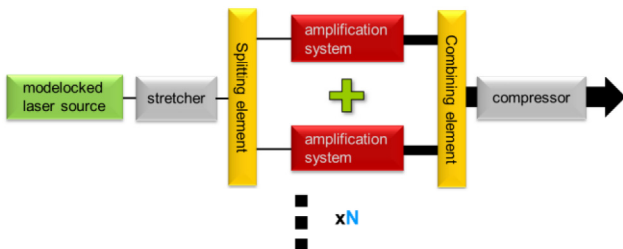


Figure 1: Schematic setup of the coherent combination of amplifiers in a CPA system.

Theoretical analysis

The coherent combination of ultrashort pulses results in new challenges because effects like dispersion, temporal delays between pulses and non-linear effects have to be considered. Therefore, it is necessary to do a theoretical investigation into how these effects impact the combining process. It could be shown that under realistic environmental conditions, a high efficiency of the combining process can still be achieved, even when increasing the number of amplifiers to a large number [1].

Experimental results

The coherent combining concept has so far been realized in two-channel experimental setups. Those setups employed state-of-the art technologies for amplifying ultrashort pulses like CPA and active phase shaping. Ad-

ditionally, an active stabilization system based on the Hänsch-Couillaud approach was implemented.

With these techniques, we could demonstrate that pulse energies of up to 3mJ [2] and average powers of up to 88W [3] combined and compressed can be realized by using Ytterbium-doped rod-type LMA fibers. Those values were achieved with combining efficiencies typically around 90% and the achieved peak power is a record value for a fiber CPA system. (see fig 2.)

Additionally, we demonstrated the use of the LPF fiber design for coherent combination. By using the excellent mode stability of those fibers at high average powers, we could achieve a combined and compressed average power of 215W.

Currently, the experimental realization of a CPA system with four coherently combined amplifiers is in progress. This should allow for the realization of femtosecond pulses with multi millijoules of energy at hundreds of Watts of average power.

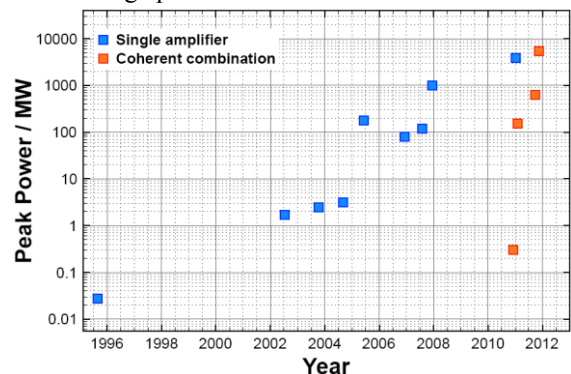


Figure 2: Development of the peak power of single amplifier and coherently combined femtosecond fiber based laser systems.

References

- [1] A. Klenke, E. Seise, J. Limpert, and A. Tünnermann, "Basic considerations on coherent combining of ultrashort laser pulses," *Opt. Express* **19**, 25379-25387 (2011).
- [2] A. Klenke, E. Seise, S. Demmler, J. Rothhardt, S. Breitkopf, J. Limpert, and A. Tünnermann, "Coherently-combined two channel femtosecond fiber CPA system producing 3 mJ pulse energy," *Opt. Express* **19**, 24280-24285 (2011).
- [3] E. Seise, A. Klenke, S. Breitkopf, J. Limpert, and A. Tünnermann, "88 W 0.5 mJ femtosecond laser pulses from two coherently combined fiber amplifiers," *Opt. Lett.* **36**, 3858-3860 (2011).

High repetition rate Optical Parametric Chirped Pulse Amplifier system for FEL applications

F. Tavella¹, A. Willner^{1,2}, M. Schulz^{2,3}, R. Riedel^{1,3}, M. Prandolini¹, A. Hage³, M. A. Seise^{1,4}, T. Gottschall⁴, S. Düsterer^{1,2}, J. Rossbach³, J. M. Drescher³, J. Limpert^{1,4}, A. Tünnermann^{1,4}, J. Feldhaus^{1,2}

¹HI-Jena, Germany; ²DESY, Hamburg, Germany; ³University of Hamburg, Germany; ⁴IAP Jena, Germany; Collaboration Partners: Queens University of Belfast (Group of M. Zepf); Centre for Plasma Physics and Lasers, TEL of Crete (Group of N. A. Papadogiannis, M. Tatarakis); ILT Aachen (P. Russbueldt); Amphos GmbH (T. Mans, C. Schnitzler, J. Dolkemeyer).

An amplifier system based on Optical Parametric Chirped Pulse Amplification (OPCPA) is planned for applications at the FLASH free electron laser. This amplifier is designed to be applied to several applications. Possible applications are pump probe laser, photo-injector Laser amplifier and FEL seed laser amplifier. Free electron laser seeding will be the testing ground for a prototype, which is currently being developed. An advanced XUV seed source is being developed in parallel to the laser amplifier. The objective is to maximize the XUV yield as the pulse energy of the amplifier is limited due to the high specified repetition rate of 0.1-1 MHz (FLASH repetition rate).

Optical Parametric Chirped Pulse Amplifier: pump amplifier development

The OPCPA pump amplifier system is the heart of the system and represents the most difficult part of this development, as 20 mJ pulse energy is required at high repetition rates. Different approaches are pursued. One relies on the Innoslab amplifier concept developed at the Institute of Laser Technik in Aachen. This amplifier system was tested to reach pulse energies of 20 mJ at 12.5 kHz repetition rate [1]. In the second approach, a laser amplifier system based on Yb:YAG thin-disk multipass amplification with 30 passes through the gain medium (thickness = 360 μ m, doping concentration 7 at. %) was used for further amplification to higher repetition rates in a burst operation mode. The seed pulse from a fiber laser (375 μ J pulse energy, IAP Jena) was amplified in the thin-disk multipass amplifier to a pulse energy of 44.5mJ, leading to a total amplification factor of 118 (1.17 per pass). The burst energy stability is approximately 1% rms at a maximum output power of 2.5kW or pulse energy of 25mJ at 100 kHz repetition rate, as demonstrated in Reference [2]. The pulses are compressed in a grating compressor to ~820 femtoseconds duration with a compressor transmission efficiency of more than 70%. These pulses were then used to generate the second harmonic at 515 nm with an efficiency of more than 50%. In the third approach, a combination of an Yb:YAG Innoslab amplifier with an output pulse energy of 5mJ with the thin-disk multipass amplifier with 10 passes through the disk medium was studied. The pulses were amplified to 24mJ, leading to a total amplification factor of 4.8 (1.17 per pass) with a burst energy stability below 1% rms.

FLASH-2 XUV seed source

An efficient XUV seeding source needs to be developed for the FLASH2 free electron laser. This has been the focus of several experiments. The main result was the proof-of-principle of dual-gas high harmonic generation (HHG) [3]. The principle of this high harmonic generation method is the enhancement of the XUV signal using hydrogen jets for phase tuning between multiple HHG sources. The main objective is to tune the hydrogen pressure such that only constructive interference of the multiple HHG generation zones can be observed. The proof-of-principle experiment and the subsequent experiment [4] with an increased number of gas nozzles (generation zones) showed excellent enhancement of the HHG conversion efficiency. The results could be confirmed with 3D simulations. A third experiment was performed in collaboration with the Center for Free Electron Laser Science, in order to test the effect of Quasi-Phase-Matched (QPM) HHG at wavelengths around 10nm. The phase tuning could be reproduced for short wavelengths. The same technique was used to enhance the harmonic signal in an experiment performed at the IAP Jena with a high average power fiber amplifier as a harmonic driver source. In conclusion, the novel HHG scheme shows a very good performance in terms of enhancing the total XUV photon flux and of controlling the coherence properties of the XUV radiation. Further investigations are necessary for an absolute enhancement in comparison with usual HHG schemes such as capillary-based high harmonic generation.

References

- [1] M. Schulz *et al.*, "Yb:YAG Innoslab amplifier: efficient high repetition rate subpicosecond pumping system for optical parametric chirped pulse amplification" *Opt. Lett.* 36, 2456-2458 (2011).
- [2] M. Schulz *et al.*, "Pulsed operation of a high average power Yb:YAG thin-disk multipass amplifier" *Opt. Express* 20, 5038-5043 (2012)
- [3] A. Willner *et al.*, "Coherent Control of High Harmonic Generation via Dual-Gas Multijet Arrays", *Phys. Rev. Lett.* 107, 175002 (2011)
- [4] A. Willner *et al.*, "Efficient control of quantum paths via dual-gas high harmonic generation", *N. J. Phys.* 13, 113001 (2011)

Laser particle acceleration

Absorption of circularly polarized laser pulses in near-critical plasmas*

J. Polz¹, A. P. L. Robinson², R. M. G. M. Trines², and M. C. Kaluza^{1,3}

¹Institut für Optik und Quantenelektronik, Max-Wien-Platz 1, 07743 Jena, Germany; ²Central Laser Facility, STFC Rutherford-Appleton Laboratory, Chilton, Didcot, Oxfordshire, OX11 0QX, UK; ³Helmholtz-Institut Jena, Fröbelstieg 3, 07743 Jena, Germany

Absorption of laser light in plasmas is a central point in the context of laser-plasma-interactions. Here, we concentrate on the description of absorption in near-critical plasmas, which means plasmas in the range of $0.1 \cdot n_c < n_e < a_0 \cdot n_c$, where n_c is the critical density of the laser and a_0 is the normalized vector potential of the focused laser pulse [1].

In the literature two concepts of absorption are described. One is dominated by leading-edge depletion (LED), where the forward push on the electrons at the head of the pulse is dominant [2, 3], while in the other the ponderomotive expulsion of electrons in the transverse direction is dominating (transverse ponderomotive acceleration, TPA) [4, 5, 6, 7, 8, 9]. So far it was unclear, however, if these two regimes are occurring distinct from another, or if they are acting simultaneously and cannot be delimited against each other.

We derived a new set of formulae for one-dimensional theory to describe the leading edge velocity u and the erosion velocity v_{er} of a laser pulse propagating in a near-critical plasma in the LED regime based on energy balance considerations in relativistic fluid motion (for a detailed derivation see [1]). The loss of energy at the leading edge of the laser pulse is approximately

$$\frac{d\chi_L}{dt} = -\frac{a_0^2}{4} m_e c^2 n_0 u \quad (1)$$

with χ_L the laser pulse energy per unit area, n_0 the electron density and u the velocity of the leading edge. Expressing the energy loss in terms of the erosion velocity v_{er} and the laser intensity I gives

$$\frac{d\chi_L}{dt} = -\frac{v_{er} I}{2c}. \quad (2)$$

The erosion velocity is related to the leading edge velocity via the group velocity of the laser $u = v_g - v_{er}$. While the group velocity is given by $v_g = \frac{\delta\omega}{\delta k}$ and the dispersion relation of a circularly polarized laser pulse in the plasma ($\omega^2 = c^2 k^2 + \omega_p^2 / \sqrt{1 + a_0^2}$), the leading edge velocity and the erosion velocity can be calculated from equation 1 and 2 as

$$u = \frac{v_g(\omega_L^2/\omega_p^2)}{\frac{1}{2} + \frac{\omega_L^2}{\omega_p^2}} \quad (3)$$

$$v_{er} = \frac{v_g/2}{\frac{1}{2} + \frac{\omega_L^2}{\omega_p^2}} \quad (4)$$

In two dimensions we can follow the same way to derive the formulae for the TPA regime. The energy losses are given by

$$\frac{d\mathcal{E}_L}{dt} = a_0 m_e c^2 n_0 u A_L \quad (5)$$

and

$$\frac{d\mathcal{E}_L}{dt} = \frac{v_{er} I A_L}{c}, \quad (6)$$

with \mathcal{E}_L the energy, and A_L the cross-sectional area of the laser pulse, leading to

$$u = \frac{v_g}{1 + \frac{\omega_p^2}{a_0 \omega_L^2}}, \quad (7)$$

by equating the relations 5 and 6.

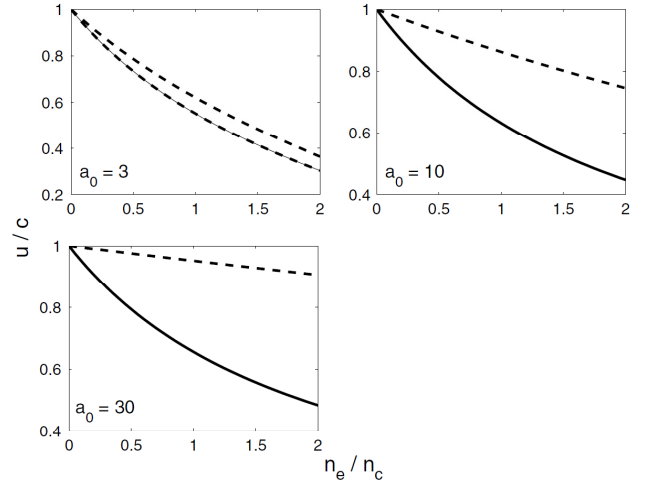


Figure 1: Plot of the leading edge velocities calculated from equation 3 for LED (solid) and equation 7 for TPA (dashed). The chosen normalized vector potential is given in each panel. Note that a smaller leading edge velocity translates to a higher erosion velocity for the same value of n_e . For increasing values of a_0 the erosion velocity and thus the depletion rate is decreasing [1].

To test our analytical set of formulae, we carried out two dimensional PIC simulations using the EPOCH code, where a circularly polarized laser pulse with $1 \mu\text{m}$ wavelength was normally incident on a $50 \mu\text{m}$ hydrogenic plasma slab. The pulse was represented by a flat top temporal profile with a pulse duration of $\tau_L = 40 \text{ fs}$, a Gaussian transverse profile characterized by its radius r_L and a normalized vector potential of $a_0 = 10$. A first set of simulations was carried out with plasma densities in the range

* The work leading to these results has received funding by the Bundesministerium für Bildung und Forschung (under contracts 03ZIK052 and 03ZIK445), and by the Helmholtz Gemeinschaft (under grant VH-NG-331)

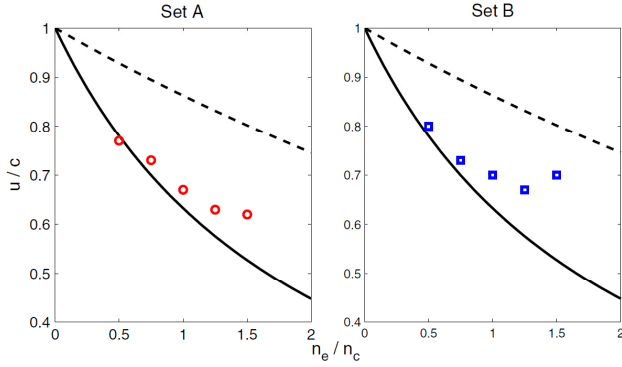


Figure 2: Leading edge velocities obtained from 2D PIC simulations of set A (left; circles) and set B (right; squares) plotted against analytical formulae for LED (equation 3; solid) and TPA (equation 7; dashed) [1].

of $0.5 - 1.5n_c$. The radii of the laser pulse were set to $r_L = 10 \mu\text{m}$ (set A) and $r_L = 2 \mu\text{m}$ (set B).

In figure 2 the leading edge velocities are plotted against the analytical formulae 3 and 7. In both sets the plots show a good agreement between the PIC simulations and the LED analytic formula for low densities. At higher densities the simulations start to diverge from the predicted velocity values. The TPA analytic formula at any point shows a good representation of the simulation results. To understand the behaviour at higher densities we analyze the depletion of the electromagnetic energy of the laser pulse (see figure 3). Even though the leading edge velocities are similar (cf. figure 2), the absorption rate for the wider laser pulse (set A) is higher than for the narrow one (set B). This is caused by the self focusing of the laser pulse, transporting energy from its wings to the central region and effectively increasing the normalized vector potential of the pulse. This leads to a slower depletion of the energy of the narrow focussed laser pulse due to its stronger self focussing (also compare figure 1 and [1]).

To point out that TPA starts to dominate over LED at higher densities, we performed another set of 2D simulations, where we set the density range to $n_e = 2 - 4n_c$ while we kept the vector potential at $a_0 = 10$ and the radius of the laser at $r_L = 10 \mu\text{m}$ (set C). The obtained leading edge velocities are plotted in figure 4, where one can see, that they now completely depart from the LED prediction, following closely the TPA prediction. Due to filamentation and self-focussing, we observe an increase of intensity of a factor of 2 in the simulations. By taking into account this fact in the TPA formula (equation 7), an even better agreement between theory and simulations is found.

Here, we have derived a new set of analytic formulae for the LED and the TPA regime, which we compared against 1D and 2D simulations. The LED analytic formulae have been found in excellent agreement with the simulation results of the 1D EM PIC calculations. For the 2D PIC simulations we showed a very good agreement to the analytic formulae and the two existing regimes of LED and TPA with a smooth transition between them. Both the analytic formulae and the simulations show that in the LED regime, for near-critical plasmas, the absorption is higher than for the

TPA regime.

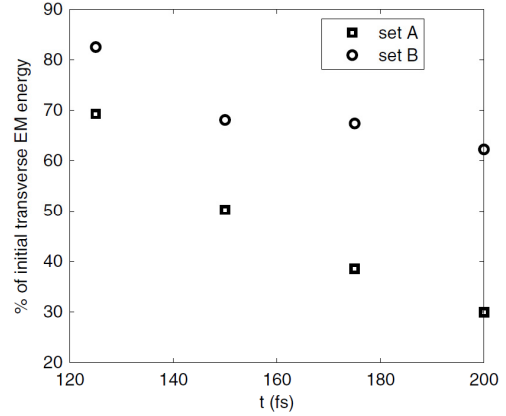


Figure 3: Fraction of the initial transverse EM energy of the laser for the simulations with $n_e/n_c = 1.5$ of set A (squares) and set B (circles) [1].

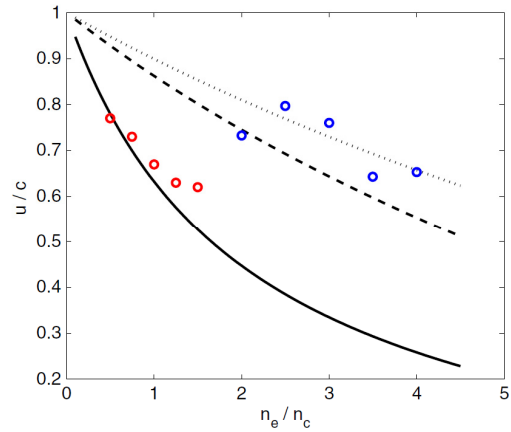


Figure 4: Leading edge velocities in simulations of set A (red circles) and set C (blue circles) plotted against electron density. Also shown are the analytic formula for LED (equation 3; solid) and TPA (equation 7; dashed). When taking account for intensity increase due to self focussing and plotting the TPA analytic formula with a_0 set to $\sqrt{2}a_0$ (dotted) a good agreement is found [1].

References

- [1] A. P. L. Robinson *et al.*, Plasma Phys. Control. Fusion, 53, 065019 (2011)
- [2] C. D. Decker *et al.*, Phys. Plasmas, 3, 2047 (1996)
- [3] S. V. Bulanov *et al.*, Phys. Fluids B, 4, 1935 (1992)
- [4] P. M. Nilson *et al.*, New J. Phys., 12, 045014 (2010)
- [5] A. B. Borisov *et al.*, Phys. Rev. A, 45, 5830 (1992)
- [6] W. B. Mori *et al.*, Phys. Rev. Lett., 60, 1298 (1988)
- [7] A. Macchi *et al.*, Plasma Phys. Control. Fusion, 51, 024005 (2009)
- [8] B. Quesnel and P. Mora, Phys. Rev. E, 58, 3719 (1998)
- [9] D. Bauer *et al.*, Phys. Rev. Lett., 75, 4622 (1995)

A cryogenic liquid micro droplet source for laser plasma interactions*

J. Polz¹, R. A. Costa Fraga³, A. Kalinin³, M. Kühnel³, D. C. Hochhaus^{4,5}, A. Schottelius³, P. Neumayer^{4,5}, R. E. Grisenti^{3,6}, and M. C. Kaluza^{1,2}

¹Institut für Optik und Quantenelektronik, Max-Wien-Platz 1, 07743 Jena, Germany; ²Helmholtz-Institut Jena, Fröbelstieg 3, 07743 Jena, Germany; ³Institut für Kernphysik, J. W. Goethe-Universität, Max-von-Laue-Str. 1, 60438 Frankfurt am Main, Germany; ⁴EMMI Extreme Matter Institute and Research Division, GSI Helmholtzzentrum für Schwerionenforschung, Planckstr. 1, 64291 Darmstadt, Germany; ⁵FIAS Frankfurt Institute for Advanced Studies, J. W. Goethe-Universität, Ruth-Moufang-Str. 1, 60438 Frankfurt am Main, Germany; ⁶GSI Helmholtzzentrum für Schwerionenforschung, Planckstr. 1, 64291 Darmstadt, Germany

In laser ion acceleration experiments using laterally extended metal foils, the hot electron distribution generating the accelerating fields at the target surface, rapidly spreads out over an area, much bigger than the focal spot size, leading to a significant reduction of the fields [1]. One solution is to use targets with transversely limited dimensions (“mass limited targets”) [2]. However, these targets need supporting structures, allowing a part of the hot electrons to spread, they have to be precisely aligned to the laser after each shot and they are complicated and expensive to fabricate.

An alternative are truly isolated micrometer sized droplets from liquid jets. When a liquid is forced through a nozzle, initially producing a cylindrical jet, it eventually starts to randomly break up into a stream of droplets due to the Plateau-Rayleigh instability. The applicability of this scheme for laser plasma experiments has already been proven by the use of water micro droplets [3]. Here, we present a source for micrometer sized droplets of cryogenic gases like hydrogen or argon for laser plasma interaction studies [5]. Due to the comparable high vapor pressure of hydrogen or argon at their triple point, a rapid evaporation cooling of the liquid occurs, as soon as it is injected into vacuum. This leads to a transition to the solid state, before the liquid is able to break up into droplets. This freezing can be prevented by injection of the liquid gases into a separate volume at pressures of the order of the vapor pressure [4]. At our droplet source, this volume is formed by an outer glass tube which is positioned over the inner orifice, where we minimized the distance between the two nozzles, to reduce the interaction length of the liquid jet with the co-flowing gas, increasing the spatial stability of the droplets.

The nozzle is formed by commercially available pulled glass tubes, which are broken under microscope view control, at the desired nozzle diameter, ensuring sharp edged profiles for laminar liquid flow conditions at the orifice exit. The capillaries are bonded to a copper connector, which is sealed under compulsion against a copper joint. A piezo-electric modulator attached to the droplet source ensures the forced breakup of the liquid jet at a fixed frequency, allowing synchronization of the droplets to the laser pulses.

To demonstrate the spatial stability of the droplets produced by our source, we compare different images shown in figure 1 right. From the different images the displace-

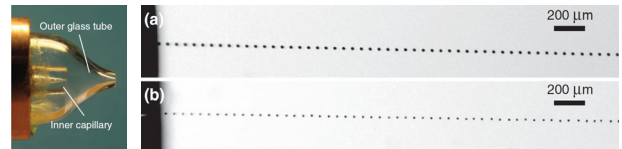


Figure 1: Left: Inner capillary for liquid jet generation and outer capillary for ambient gas allocation to prevent jet freezing. Right: Images of periodic droplet streams of a) argon and b) hydrogen [5]

ment of the individual droplets from the center of the stream can be deduced. The mean relative displacement $\langle \delta r \rangle$ is then plotted against the distance z from the opening of the outer glass tube. To ensure a good overlap between droplets and laser focus the condition $\langle \delta r \rangle < r_L$, where r_L is the laser focal spot radius, has to be met. As one can see in figure 2, a nearly ideal overlap is guaranteed within a few millimeters from the nozzle exit point for realistic spot size radii of $r_L \geq 2 \mu\text{m}$.

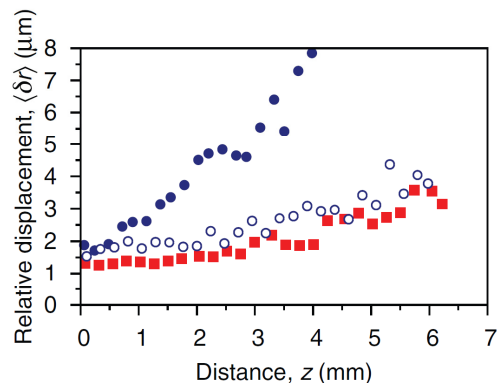


Figure 2: Relative mean droplet displacement $\langle \delta r \rangle$ plotted against distance z from the nozzle exit aperture. The filled circles (hydrogen) and squares (argon) are for expansion in co-flowing gas, while the open circles (hydrogen) are without additional gas environment. [5]

References

- [1] O. Jäckel *et al.*, New J. Phys., 12, 103027 (2010).
- [2] C. Strangio *et al.*, Las. Part. Beams, 25, 85-91 (2007).
- [3] S. Ter-Avetisyan *et al.*, Phys. Rev. Lett. 96, 145006 (2006).
- [4] Ö. Nordhage *et al.*, Nucl. Instrum. Methods Phys. Res. A 546, 391 (2005).
- [5] R. A. Costa Fraga *et al.*, Rev. Sci. Instrum. 83, 025102 (2012)

* The work leading to these results has received funding by the Bundesministerium für Bildung und Forschung (under contracts 03ZIK052 and 03ZIK445), and by the Helmholtz Gemeinschaft (under grant VH-NG-331).

Water micro droplets for laser ion acceleration*

J. Polz¹, A. Sävert¹, M. Schwab¹, M. Reuter¹, A. K. Arunachalam¹, O. Jäckel¹, S. Herzer¹, D. Klöpfel¹, W. Ziegler¹, F. Ronneberger¹, B. Beletes¹, A. Gopal¹, A. P. L. Robinson⁵, R. A. Costa Fraga³, A. Kalinin³, R. E. Grisenti^{3,4}, G. G. Paulus¹, and M. C. Kaluza^{1,2}

¹Institut für Optik und Quantenelektronik, Max-Wien-Platz 1, 07743 Jena, Germany; ²Helmholtz-Institut Jena, Fröbelstieg 3, 07743 Jena, Germany; ³Institut für Kernphysik, J. W. Goethe-Universität, Max-von-Laue-Str. 1, 60438 Frankfurt am Main, Germany; ⁴GSI Helmholtzzentrum für Schwerionenforschung, Planckstr. 1, 64291 Darmstadt, Germany; ⁵Central Laser Facility, STFC Rutherford-Appleton Laboratory, Chilton, Didcot, Oxfordshire, OX11 0QX, UK

The applicability of water micro droplets for laser plasma experiments has already been proven [1, 2, 3]. But so far the energy of the generated protons was limited to approx. 1 MeV, which was attributed to the limited pulse contrast of the order of 10^{-7} on a ns timescale. In a recent experiment at the JETI laser facility, delivering a pulse contrast of 10^{-10} until 1 ns and 10^{-8} until 10 ps before the main pulse, proton energies up to 10.5 MeV have been achieved.

The generation of the water droplet beam has been achieved by commercially available nozzles delivering 25 μm droplets, synchronized to the laser pulse by means of a built in piezo actuator, driven by a triggerable frequency generator. The positioning of the droplets in the laser focal spot is controlled by means of a probe beam aligned perpendicular to the main beam. This probe beam illuminates the droplets which are imaged onto a CCD camera by an $f/2$ imaging lens, allowing for μm -accuracy. The generated ion beam propagates towards a plastic scintillator $20 \times 20 \times 0.5 \text{ cm}^3$ in size, covering a solid angle of 0.49 sr. The ion beam profile is recorded using a gateable CCD. The shutter window of the camera was 10.5 ns long, opening 7.7 ns after the laser pulse arrived at the scintillator, representing an energy interval of the protons of 1 to 5 MeV. Part of the ion beam is traveling through a hole in the scintillator, towards a Thomson spectrometer recording the energy of the particles.

Sokollik *et al.* [4] have shown, that even for a spherical target one would expect the generation of a directional beam of ions. For our experimental conditions we observe, as shown in figure 1, that the ion beam is undergoing strong filamentation during the acceleration, caused by ionization effects, as described in [5]. The strong spatial fluctuation of the ion beam also led to strong variations in the recorded proton energy spectra.

The length of the 10^{-8} ASE pedestal of JETI can be tuned by means of a fast Pockels cell, enabling us to investigate the influence of the corresponding pre-plasma gradient on the cut-off energy of the generated fast protons. The minimum ASE pedestal of 600 ps duration is given by half of the stretched pulse length of 800 ps in the amplifier and 200 ps rise time of the Pockels cell window. As shown in figure 2 left the highest proton energies are not reached for maximum suppression of the ASE pedestal by the fast Pockels cell, but if the duration of the pedestal is increased by 150

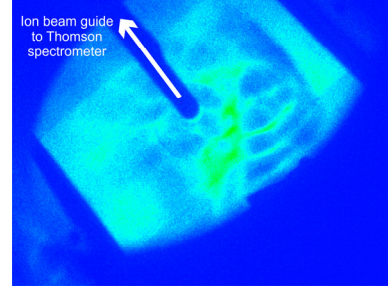


Figure 1: Typical imprint of the beam profile corresponding to a spectral window of 1 to 5 MeV protons. Strong modulations are visible, indicating filamentation of the ion beam. The shadow is created by the ion beam guide to the Thomson spectrometer.

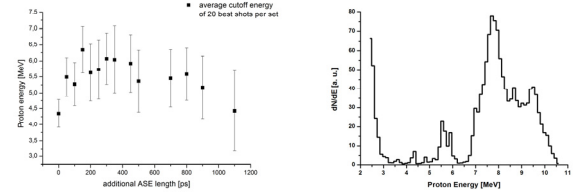


Figure 2: Left: Mean cutoff-energy of proton spectra plotted against additional ASE pedestal. The highest proton energies are achieved for an additional ASE duration of 150 - 350 ps. Right: For optimum conditions proton cut-off energies of 10.5 MeV are observed.

to 350 ps. For optimum conditions we are able to generate spectrally modulated proton spectra with cut-off energies of 10.5 MeV, as shown in figure 2 right, which marks an improvement of a factor of ten over results published so far with these kind of targets [1, 2, 3].

References

- [1] S. Ter-Avetisyan *et al.*, Phys. Rev. Lett. 96, 145006 (2006).
- [2] M. Schnürer *et al.*, Las. Part. Beams, 23, 337343 (2005).
- [3] A. V. Brantov *et al.*, Phys. Plasmas 13, 122705 (2006).
- [4] T. Sokollik *et al.*, PRL 103, 135003 (2009).
- [5] J. Fuchs *et al.*, Phys. Rev. Lett. 91, 255002 (2003)

* The work leading to these results has received funding by the Bundesministerium für Bildung und Forschung (under contracts 03ZIK052 and 03ZIK445), and by the Helmholtz Gemeinschaft (under grant VH-NG-331).

Implications for the electron distribution from the stationary hydrodynamic model of one-dimensional plasma expansion into vacuum

T. Kiefer*¹ and T. Schlegel²

¹Friedrich-Schiller-Universität Jena, Germany; ²Helmholtz Institute Jena, Germany

Standard analytical theory of Target Normal Sheath Acceleration (TNSA) is commonly based on estimates for the number and energy distribution of hot electrons, which are heated by a short intense laser pulse at the front side of a solid foil target. In most of these approaches, the energetic electrons are treated kinetically, e.g. in [1], as it is also predicted by multiple Particle-in-Cell (PIC) simulations. The expansion of the hot electron gas is described by a collisionless one-dimensional electrostatic model. Since the electron mass is small in comparison with that of the ions, one may assume an almost instantaneous arrangement of the electron distribution in a stationary configuration. The corresponding proper mathematical description employs the stationary, one-dimensional, electrostatic Vlasov equation

$$\frac{p}{m_e} \frac{\partial f_e}{\partial x} + e \frac{\partial \phi}{\partial x} \frac{\partial f_e}{\partial p} = 0. \quad (1)$$

Its solution $f_e(x, p) = f_{e,0}(\sqrt{p^2 - 2m_e e \phi(x)})$ provides an expression for the electron density as a function of the electric potential ϕ ,

$$n_e(\phi) = \int_{\mathbb{R}} f_{e,0}(\sqrt{p^2 - 2m_e e \phi(x)}) dp. \quad (2)$$

The distribution function $f_{e,0}$ can be chosen arbitrarily but has to fulfill the symmetric condition $f_{e,0}(p) = f_{e,0}(-p)$. It specifies the electron density in the absence of a potential ($\phi = 0$) and is usually described by a Maxwellian distribution, for which reason (2) becomes $n_e(\phi) = n_{e,0} \exp(\phi/T_{e,0})$, with the initial mean energy $T_{e,0}$.

Besides the kinetic approach a hydrodynamic ansatz was supposed [2, 3]. It starts from the Euler equation for an ideal electron fluid, assuming 'massless' electrons, and applies the adiabatic relation $P \cdot n_e^{-\kappa} = \text{const}$ for an ideal gas, which gives the relation

$$n_e(\phi) = n_{e,0} \cdot \left(1 + \frac{\kappa - 1}{\kappa} \frac{e \phi}{T_{e,0}}\right)^{1/(\kappa-1)}. \quad (3)$$

Like (2) the above expression defines the electron density as a function of the electric potential. It is expected that this approach automatically ensures energy conservation during the adiabatic plasma expansion process, as distinguished from the assumption of a Maxwellian distribution [4].

Recently we have shown that the hydrodynamic relation (3) is included in (2) as a special case with a particular distribution function. To address the problem, we inverted the relation (2) in terms of $f_{e,0}$. This was done with the help of

Fourier transforms. Using the inversion formula

$$f_{e,0}(p) = \frac{m_e}{\pi} \int_{-\infty}^{-\frac{p^2}{2m_e}} \frac{n_e\left(-\frac{p^2}{2m_e}\right) - n_e(\tilde{\psi})}{\left|p^2 + 2m_e \tilde{\psi}\right|^{3/2}} d\tilde{\psi}, \quad (4)$$

one directly finds the electron distribution $f_{e,0}$ which is associated with the electron density (3) as

$$f_{e,0}(p) = \alpha \frac{n_{e,0}}{\sqrt{2m_e T_{e,0}}} \cdot \Theta \left[1 - \frac{\kappa - 1}{\kappa} \frac{p^2}{2m_e T_{e,0}}\right] \cdot \left(1 - \frac{\kappa - 1}{\kappa} \frac{p^2}{2m_e T_{e,0}}\right)^{\frac{\kappa}{\kappa-1} - \frac{3}{2}}, \quad (5)$$

with some constant α . This phase space density is gener-

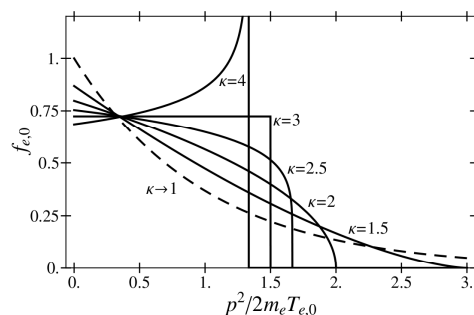


Figure 1: Electron phase space density (5) for different values κ . The limiting case of a Maxwellian distribution for $\kappa \rightarrow 1$ is displayed by a dashed line.

ally not Maxwellian, as Fig. 1 shows. Hence, the use of (3) implies always a specific electron distribution (5). Moreover, it may lead to large deviations from the correctly determined evolution of the phase space density gained from a conservative kinetic algorithm [5]. Agreement between both approaches could be obtained only for $\kappa = 3$. For this special case, the nonrelativistic analysis has been generalized also to relativistic energies $T_{e,0} \gtrsim m_e c^2$.

References

- [1] J. E. Crow, P. L. Auer, and J. E. Allen, *J. Plasma Phys.*, **14** (1974) 6; P. Mora, *Phys. Rev. Lett.*, **90** (2003) 185002
- [2] C. Sack and H. Schamel, *Phys. Rep.*, **156** (1987) 311
- [3] A. Andreev, A. Lévy, T. Ceccotti, C. Thauray, K. Platonov, R.A. Loch, and P. Martin, *Phys. Rev. Lett.*, **101** (2008) 155002
- [4] P. Mora, *Phys. Rev. E*, **72** (2005) 056401
- [5] T. Grismayer, P. Mora, J. C. Adam, and A. Heron, *Phys. Rev. E*, **77** (2008) 066407

* kiefer.thomas@gmail.com

Radiation Pressure Assisted Ion Acceleration using Multi-Component Targets

S. Kuschel^{1,2}, B. Aurand^{1,3,4,5}, C. Rödel^{1,2}, S. Herzer^{1,2}, J. Polz^{1,2}, A. E. Paz^{1,2}, O. Jäckel^{1,2}, P. Gibbon^{5,6}, A. Karmakar^{5,6}, B. Elkin⁷, G. G. Paulus^{1,2}, T. Kühl^{1,3,4,5}, and M. C. Kaluza^{1,2}

¹Helmholtz Institute Jena, Fröbelstieg 3, D-07743 Jena, Germany; ²Institute of Optics and Quantum Electronics, Friedrich Schiller University, Germany Jena, D-07743 Jena; ³GSI Helmholtzzentrum für Schwerionenforschung, D-64291 Darmstadt, Germany; ⁴Universität Mainz, D-55099 Mainz, Germany; ⁵ExtreMe Matter Institute, D-64291 Darmstadt, Germany; ⁶Institute for Advanced Simulation, Forschungszentrum Jülich GmbH, D-52428 Jülich, Germany; ⁷Faunhofer Institute for Interfacial Engineering and Biotechnology, Stuttgart, Germany

Ion acceleration using the radiation pressure of an ultra-intense laser pulse attracted strong interest due to its potential of generating ion spectra with low energy spread. We performed experiments at the 40-TW laser system "JETI" at high contrast. The obtained ion spectra show distinct signatures of quasi-monoenergetic ion acceleration when multi-component foils of a few nanometer thickness were used. The results provide evidence of an acceleration mechanism of ions that is assisted by the radiation pressure. Particle-in-cell simulations support our findings and reveal a two stage process. First, the ion species are separated due to the radiation pressure while the laser pulse interacts with the plasma. In a second step, the ions are accelerated by target normal sheath acceleration (TNSA). The combination of both effects leads to broad ion spectra with quasi-monoenergetic features.

Introduction

The acceleration of matter using the radiation pressure was first proposed in the context of interstellar spacecrafts [1]. Since the advent of ultra-intense laser pulses this acceleration scheme became relevant also for particle acceleration. Here, the radiation of a high intense laser pulse focussed to the intensity I_L onto a target exerts a pressure $p = (1 + R) \cdot I_L/c$ where R is the target reflectivity and c is the speed of light. The radiation pressure thus enables a uniform acceleration of a macroscopic target to a monoenergetic spectrum. This is in contrast to the acceleration by the electrostatic acceleration due to the electric sheath field created by heated electrons in the TNSA scheme where exponential ion spectra up to a cutoff energy are observed. In fact, it has been shown in simulations at laser intensities in the order of 10^{23} W/cm² that radiation pressure acceleration (RPA) is the dominant acceleration mechanisms leading up to GeV proton energies when ultra-thin foils of nanometer thickness are used. However, it has been predicted that RPA could be observed at currently available intensities using multi-component foil targets. A comparison between the pressure generated by the laser radiation and the pressure owing to the electrostatic charge separation induced in the target of thickness d leads to a balance condition $a_0 \cdot \sqrt{1 + R} \approx \sigma$

between the amplitude of the normalized vector potential $a_0 = \sqrt{I_L \lambda_L^2 / (1.37 \cdot 10^{18} \text{ W/cm}^2 \cdot \mu\text{m}^2)}$ and the normalized target density

$$\sigma = n_e/n_c \cdot d/\lambda_L \approx a_0. \quad (1)$$

Experiment

The experiment was performed at the JETI laser system delivering pulses of 1 J in 27 fs, with a 10 ps-prepulse contrast of 10^{-6} . This contrast is improved to 10^{-9} by using a plasma mirror set-up integrated into the laser beam line [2]. The improvement of the contrast is a necessary step for using nanometer foil targets. The laser, now delivering high contrast pulses containing up to 500 mJ on target, was focused by an off-axis parabola to an intensity up to $6 \cdot 10^{19}$ W/cm² ($a_0 \approx 5$). The polarization of the laser-pulse can be changed from linear to circular by a remote-controlled quarter-wave plate (Figure 1). Up to now, diamond-like carbon (DLC) foils of nanometer thickness have been used in these experiments in order to provide free-standing targets that satisfy this condition [4]. We developed parylene foils which are mechanically stable and mounted onto a grid such that several tens up to hundred free-standing foils are provided by a single mount.

We found that parylene foils have significant advantages as compared to commercially available DLC foils with low sp^3 content. First, the optical transparency of parylene lowers its sensitivity to prepulses and amplified spontaneous emission (ASE). The second advantage is the lower density as compared to DLC. This allows the use of foils with larger thickness that are more stable and satisfy condition 1 at the same time. The decisive advantage, however, is the composition of multiple ion species since particle-in-cell simulations have suggested that RPA can be enhanced by multi-ion targets due to charge separation forces [3].

Proton and carbon ions are recorded using a Thomson parabola and a MCP detector that has been calibrated regarding its absolute sensitivity. The ion spectra consist of a broad exponential spectrum that is also observed using thin foils of micrometer thickness (Figure 2). Additionally, quasi-monoenergetic features are observed in all ion species when a 13 nm parylene foil was used. The height of the additional peak is about 30% of the interpolated

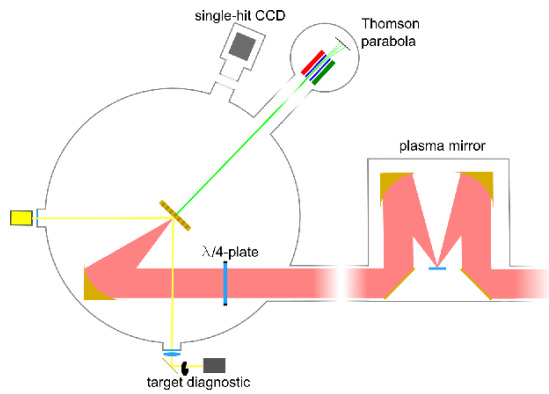


Figure 1: The experimental setup: The beam passes a plasma mirror and is focused to $6 \cdot 10^{19} \text{ W/cm}^2$ onto the target.

background. 40% of the shots in focus position showed mono-energetic features in the protons. Comparable features were also observed in the C^{5+} and C^{6+} ion traces [4].

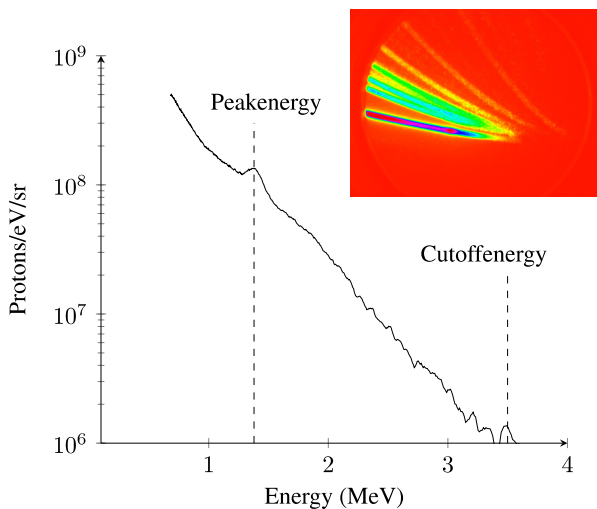


Figure 2: A typical proton spectrum with a peak at 1.4 MeV. The upper right corner shows the raw-data of this shot. These kinds of peaks are visible in 40% of the recorded shots in focus position.

The cutoff- and the peak-energy of the protons show a clear dependence on the the cutoff-energy of the C^{6+} ions (Figure 3). This leads to the conclusion, that different ion species gain their kinetic energies via the same acceleration mechanism namely TNSA. This is supported by the observation, that linear polarization produces the highest energies, while circular polarization reduces electron heating and thus TNSA in general [5].

The peaks are most likely due to a two-step acceleration process, starting with an RPA phase [3]: The strong electric field raised by the RPA process starts separating the different ion species of the ultra thin target. RPA ac-

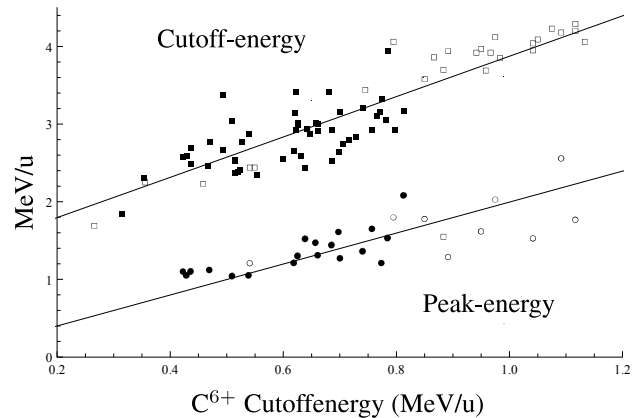


Figure 3: 111 shots showing the dependence of the proton cutoff- and peak-energy on the C^{6+} cutoff-energy. Circular polarization is depicted by filled marks, whereas linear polarization is depicted by empty marks.

celeration (and thus the ion species separation) stops at the end of the laser pulse while TNSA is present as long as hot electrons are capable of creating an accelerating sheath field. Thus, TNSA accelerates all ion species and leads to the observed peaks in the ion spectra. This acceleration step is similar to the directed-Coulomb-explosion [6] and is supported by 2D-simulations. For our laser and plasma parameters, a distinct peak in carbon and proton spectra due to RPA has been found which is in good agreement with our experimental findings [7]. When using thicker 100 nm multi-component targets, no peaks are observed neither in the simulation nor in the experiment.

References

- [1] G. Marx *Interstellar Vehicle Propelled by Terrestrial Laser Beam*, Nature 21, 22 (1966)
- [2] C. Rödel et al. *High repetition rate plasma mirror for temporal contrast enhancement of terawatt femtosecond laser pulses by three orders of magnitude*, Applied Physics B 103, 2 (2011)
- [3] B. Qiao et al. *Radiation-Pressure Acceleration fo Ion Beams from Nanofoil Targets: The Leaky Light-Sail Regime*, Phys. Rev. Lett. 105, 155002 (2010)
- [4] A. Henig et al. *Radiation-Pressure Acceleration of Ion Beams Driven by Circularly Polarized Laser Pulses*, Phys. Rev. Lett. 103, 245003 (2009)
- [5] A. Macchi et al. *Laser Acceleration of Ion Bunches at the Front Surface of Overdense Plasmas*, Phys. Rev. Lett. 94, 165003 (2005)
- [6] S.S. Bulanov et al. *Accelerating monoenergetic protons from ultrathin foils by flat-top laser pulses in the directed-Coulomb-explosion regime*, Phys. Rev. E 78, 026412 (2008)
- [7] B. Aurand, S. Kuschel et al. *Radiation Pressure Assisted Acceleration of Ions using Multi-Component Foils in High-Intensity Laser-Matter Interactions*, submitted

Tuning of a laser wake field accelerator: Recent experiments and simulations *

A. Sävert¹, S.P.D. Mangles³, M. Schnell¹, M. Reuter^{1,2}, M. Nicolai¹, O. Jäckel²,

C. Spielmann^{1,2} and M.C. Kaluza^{1,2}

¹ Friedrich Schiller Universität Jena, Germany; ² Helmholtz-Institut Jena, Germany;

³ Imperial College London, United Kingdom

Electron bunches from a laser wake field accelerator exhibit an ultra-short pulse duration (<10 fs) and a small divergence (~ 1 mrad). These unique features make these electron bunches promising candidates for the generation of secondary radiation via macroscopic or microscopic undulators (Thomson back scattering). These techniques benefit additionally from a high bunch charge.

Last year we made the discovery [1] that changing the target gas in a laser wake field accelerator from helium to hydrogen increases the bunch charge per area by more than one order of magnitude. This is a combined effect of having a 2 times smaller divergence in the transverse direction and 4 times higher bunch charge. The underlying physics, however, remained unclear. In a second campaign with the JETI laser we were able to test some of our assumptions. Switching from helium to hydrogen as a target gas changes two things: the ionization energy and the charge to mass ratio. To distinguish between effects caused by either of these two parameters we have done similar experiments using deuterium.

The new experimental setup was optimized for the laser parameters of the JETI system. The pulse duration was further shortened to $\tau = 27$ fs while the energy on target was comparable to the last campaign with 650 mJ. The shorter pulse duration allowed for a tighter focusing (using an $f/13$ off axis parabolic mirror). The resulting diameter of the focal spot was $12 \mu\text{m}$ FWHM with a vacuum FWHM intensity of $8.3 \times 10^{18} \text{ W/cm}^2$. The laser pulses hit a gas jet produced by a super sonic nozzle with 3 mm exit diameter. The electron bunch diagnostics were a scintillating phosphor screen positioned 42 cm after the nozzle to observe the pointing and the beam divergence and an electron spectrometer.

First we were looking at the pointing of the electron beam on the first scintillator screen. In Fig. 1, the transverse electron profile of 30 consecutive shots at the optimal pressure were added up. We could verify the results from our last campaign, except that deuterium produces even more stable electron pulses than hydrogen. Since H_2 and D_2 have the same ionization energies this identifies this parameter to be the main reason. The higher degree of collimation of the electron bunches from deuterium could, however, hint towards an effect of the charge-to-mass-ratio. However, recent experiments with high purity hydrogen (99.9999%) give similar results as compared to deuterium. The H_2 gas in our first measurement had a purity of 99.9% and D_2 of 99.5% only. However, the main impurities in D_2 are HD and H_2 . Neglecting ion mass effects, D_2 has the same purity as the high purity H_2 in our latest experimental campaign.

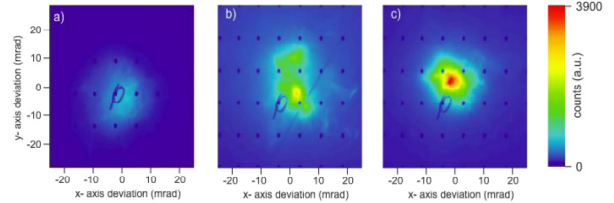


FIGURE 1: Pointing of the electron bunches at the first lanex screen for helium (a), hydrogen (b) and deuterium (c).

This means that the main reason for the observed differences is due to the different ionization levels of He (24.6 eV, 54.4 eV) and H_2 (15.4 eV for molecules). The dominant ionization mechanism is optical field ionization. The minimum required intensity for H_2 is smaller than for He and hence ionization occurs earlier. This allows the rising edge of the laser pulses to efficiently heat up the plasma due to inverse bremsstrahlung. A rough estimate leads to a plasma temperature of several hundred eV for H_2 when the electron acceleration starts.

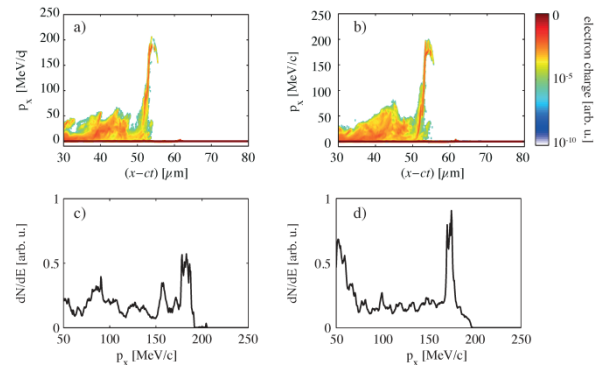


FIGURE 2: Comparison of electron momentum distribution for cold (left column) and hot (right column) simulations. Longitudinal momentum (p_x) as a function of longitudinal position ($x-ct$) after 1.13 mm for initial temperatures of a) 0 keV and b) 1 keV. Electron spectrum at the same time for c) 0 keV and d) 1 keV.

Simulations using the OSIRIS PIC code were performed with different initial plasma temperatures of 0 keV and 1 keV. First results confirm our experimental findings (Fig. 2). The higher plasma temperature leads to a higher charge of the electron bunch. Further investigations should also reveal the transverse dynamics which lead to a smaller divergence.

References

- [1] A. Sävert *et al* HI Jena report (2011)

* This work was supported by the DFG (contract no. TR18) and by the BMBF (contract nos: 03ZIK052 and 05K10SJ2)

Photon and particle spectroscopy and diagnostics:

Experiments and theory

Laser driven x-ray parametric amplification in neutral gases: a new brilliant light source in the XUV

J. Seres¹, E. Seres¹, B. Ecker^{2,3,4}, B. Landgraf^{1,4}, D. Hochhaus^{2,5,6}, D. Zimmer^{2,3}, V. Bagnoud², B. Aurand^{2,3,6}, B. Zielbauer^{2,3,4}, T. Kuehl^{2,3}, and C. Spielmann^{1,4}

¹Friedrich-Schiller-University, Jena, Germany; ²GSI Helmholtz Centre for Heavy Ion Research, Darmstadt, Germany; ³Johannes-Gutenberg-University, Mainz, Germany; ⁴Helmholtz Institute, Jena, Germany; ⁵EMMI, Extreme Matter Institute, Darmstadt, Germany; ⁶Johann-Wolfgang von Goethe-University, Frankfurt, Germany

Studying nuclear [1], inner atomic or structural dynamic requires ultra-short XUV pulses or narrow linewidth x-ray [2]. Laser based high harmonic generation (HHG) as a strongly non-linear frequency conversion process is capable to produce ultrashort XUV pulses in a laser like beam with compact laser systems. HHG does not rely on relativistic laser intensities thus high repetition rate laser systems can be used. However, due to the low conversion efficiency, HHG radiation has to be further increased.

More recently we introduced the concept of parametric amplification of HHG radiation. In the first description we added a stimulated emission process and named it self-seeded x-ray parametric amplification (XPA) [2, 3]. Beyond the super-quadratic increase of the XUV signal, which can be explained by HHG theory in a limited pressure range, other observed characteristics (exponential growth, gain narrowing, strong blue shift etc.) and their scaling with intensity and pressure [3,4] can only be explained accurately by the new XPA model.

In the last year we have improved our model. Aside atomic and free electron dispersion we included in our new model also Gaussian beam, atomic and Gouy phase shifts, and the effect of the group velocity mismatch. This extended XPA theory fully describes the observed scaling of the XUV yield with pressure, intensity, jet position, etc. [5]. For an experimental verification, we used the femtosecond front-end of the PHELIX laser system delivering 350-fs-long 7 mJ pulses and the JETI laser system delivering 30-fs-long, 1 J pulses, both at a repetition rate of 10 Hz. We focused the laser beam to a diameter, which suitable to realize XPA in Argon [3,6].

In Fig 1 we present the pressure dependence of the signal for the 35th harmonic measured with the PHELIX frontend. The diamonds represent the measurements, which has been made for a laser intensity of 2×10^{14} W/cm². The measured radiation yield increases nearly exponential with pressure (Fig. 1) at low pressures. In the pressure range above 0.6 bar, the signal saturates and a higher pressure results in a lower signal. The observed exponential increase is a clear indication of the predicted stimulated emission and parametric amplification. To compare our measurement with the existing theories, we fitted the signal (light blue) predicted with a model de-

scribing absorption limited high harmonic generation for a finite phase matching length. It can be seen that the measured behavior of the pressure dependence can fully describe with the XPA theory in the full pressure range.

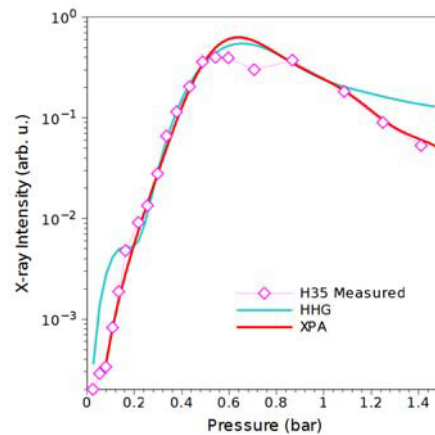


Figure 1. Measured XUV signal (diamonds) as function of pressure and a comparison with XPA and pure HHG

Additionally, for XPA and pure HHG the maximum signal is expected at different positions of the jet in respect to the focus. We checked this with a measurement series recording the x-ray spectra dependence on the jet position in a wide range of pressure and laser parameters, i.e. measurements were performed with the PHELIX frontend and the JETI laser. Again we found a very good agreement of our model with the observed scaling, such as the position of the maximum signal is independent of the jet position as predicted by XPA and in contradiction to pure HHG.

Summing up, XPA holds the promise to realize a new class of bright x-ray sources for spectroscopy and many other applications combining the advantages of conventional x-ray lasers and HHG. The excellent beam quality and the ultra-short pulse duration of HHG pulses will be then available at much higher pulse energies.

References

- [1] A. Gumberidze, et al., NIM B 267, 2480 (2009)
- [2] T. Kuehl, et al., Laser and Part. Beams 25, 93 (2007)
- [3] J. Seres, et al., Nature Phys. 6, 455 (2010)
- [4] J. Seres, et al., Nature Phys. 6, 9279 (2010)
- [5] J. Seres, et al., submitted (2012)
- [6] B. Aurand, et al., NIM A 653, 153 (2011)

Towards seeded X-ray lasers at PHELIX

B. Ecker^{1,2,#}, E. Oliva⁶, B. Aurand^{2,3,4}, D. C. Hochhaus³, T. Kuehl^{2,4}, P. Neumayer³, H. Zhao⁴,
B. Zielbauer⁴, K. Cassou⁵, S. Daboussi⁵, O. Guilbaud⁵, S. Kazamias⁵, D. Ros⁵, T. Le⁶
and P. Zeitoun⁶

¹Helmholtz Institute Jena, Helmholtzweg 4, 07743 Jena, Germany

²Johannes Gutenberg University Mainz, Saarstr. 21, 55122 Mainz, Germany

³ExtreMe Matter Institute EMMI, Planckstr. 1, 64291 Darmstadt, Germany

⁴GSI Helmholtzzentrum fuer Schwerionenforschung, Planckstraße 1, 64291 Darmstadt, Germany

⁵LASERIX-CLUPS / Laboratoire de Physique des Gaz et des Plasmas, 91400 Orsay, France

⁶Laboratoire d'Optique Appliquée, ENSTA, École Polytechnique, 91761 Palaiseau, France

Plasma-based X-ray lasers (XRL) possess several disadvantageous properties that are related to their generation process. Being based on the amplification of spontaneous emission (ASE), XRL can not provide a significant degree of spatial coherence and the beam profiles are dominated by characteristic speckle-patterns. The circumvention of these undesired properties consists in injection-seeding the XRL medium with a spectrally matched XUV pulse of a second source, which is typically either based on high-order harmonic generation (HHG) [1, 2] or a second XRL [3, 4]. HHG sources provide high-quality XUV beams but suffer from small conversion efficiencies. The spectral overlap between one of the harmonic lines and the XRL transition needs to be ensured, which can be problematic especially when working with a Nd:Glass laser like PHELIX [5]. The spectral width of HH radiation is significantly larger compared to the line width of the XRL transition. This alleviates the spectral matching but reduces the efficiency of the seeding process. Utilizing a second XRL for seeding is more demanding on the laser system in terms of the required pump energy and can not provide the beam quality offered by HHG. However, successful seeding experiments have been reported utilizing these techniques, demonstrating fully coherent and diffraction limited XRL beams.

On the road of improving the beam quality of the XRL at GSI we developed a setup that allows us to operate two independent XRL targets simultaneously. The setup is based on the in-house developed DGRIP pumping technique [6], allowing for an efficient pumping including the travelling wave excitation (TW) for both of the targets. The setup also relies on the PHELIX double-beam option originally developed for pump-probe experiments that is available since November 2010. This way, each of the two XRL targets can be pumped by its individual pump beam (Fig. 1). Due to the symmetry of the setup the XRL output of the two targets is propagating in opposite directions. The XRL pulses can be diagnosed separately or be combined in a seed/ amplifier configuration. For the latter option one can use a spherical XUV mirror to image the output of the first XRL target into the gain zone of the second.

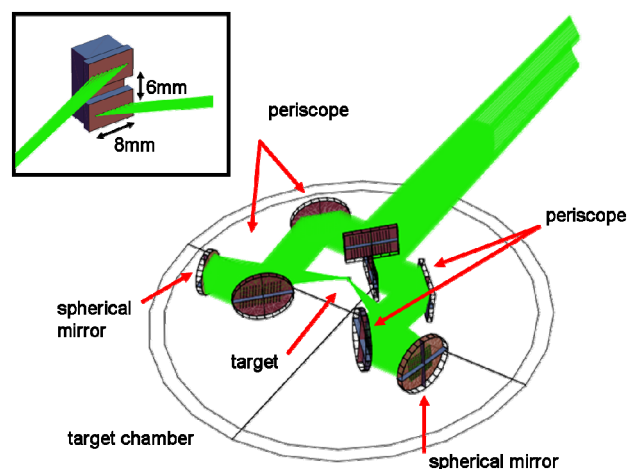


Figure 1: The Butterfly Configuration. The inset gives a more detailed view of the target arrangement [7].

A first successful experiment using this experimental scheme that we refer to as Butterfly configuration has been carried out in 2011. The results hold the promise of the determination of the life time of the gain in a transient, Ni-like silver XRL [8]. Simulations of the temporal development of the seeded XRL signal utilizing the Maxwell-Bloch code DeepOne [9] are in progress. A succeeding beam-time in 2012 is planned using molybdenum as target material, allowing us to carry out the experiment at higher laser repetition-rate and thus provide more valuable input for the development of the DeepOne code.

References

- [1] Ph. Zeitoun et al., Nature 431, (2004).
- [2] Y. Wang et al., Nature Photonics 2, 94-98 (2008).
- [3] M. Tanaka et al., Optics Letters 28, 1680-2 (2003).
- [4] M. Nishikino et al., Physical Review A 68 (2003)
- [5] D. C. Hochhaus et al., Applied Physics B (2010).
- [6] D. Zimmer et al., Optics Express 13, 2403 (2008).
- [7] B. Ecker et al., Proc. of SPIE, San Diego (2011).
- [8] B. Ecker et al., to be published.
- [9] E. Oliva et al., Phys. Rev. A 84, 013811 (2011).

[#]b.ecker@gsi.de

SHHG report (2011): Efficiency of relativistic surface harmonic generation

J. Bierbach^{1,2}, A. Galestian Pour², C. Rödel^{1,2}, O. Jäckel¹, M. C. Kaluza^{1,2}, M. Zepf^{1,3}, and G. G. Paulus^{1,2}

¹Helmholtz Institute Jena, Helmholtzweg 4, D-07743 Jena, Germany; ²Institut of Optics and Quantum Electronics, Friedrich Schiller University Jena, D-07743 Jena, Germany; ³Queen's University Belfast, BT7 1NN, United Kingdom

Ultrashort coherent XUV and soft x-ray pulses of high brilliance are required for seeding planned free-electron laser facilities like FLASH II or XFEL. Our research in the project "Surface High Harmonic Generation (SHHG)" is focused on the generation of intense XUV pulses from relativistic solid-density plasmas. We investigate the efficiency of relativistic SHHG in experiments at the 40-TW "JETI" laser system and compare it to predictions from established theory. Beam characteristics like divergence and polarization of the high harmonics are measured. Furthermore, a strong influence of the plasma scale length on the efficiency is found for the first time, which can be controlled and optimized by an adequate enhancement of the laser pulse contrast using a plasma mirror or second harmonic generation. Our experimental results are in agreement with 1D particle-in-cell simulations. We record pulse energies in the order of microjoules per harmonic line, equivalent to efficiencies of 10^{-5} . Thus, in terms of pulse energy, surface high-harmonic generation is becoming a source competitive with HHG in gases. In addition, we demonstrate the first consecutively measured relativistic surface high-harmonic generation at a repetition rate of 10 Hz yielding an average power of 10 μ W in the spectral range of 51 nm to 26 nm. This opens the way to numerous scientific applications, e.g. nonlinear XUV and XUV-XUV pump-probe experiments or the seeding of free-electron lasers.

Introduction

The generation of high harmonics of the fundamental laser field is the most prominent way to generate ultrashort pulses and provides the shortest available temporal resolution in the order of attoseconds. High-harmonic generation on solid surfaces (SHHG) using relativistic laser intensities exploits nonlinear phenomena in fully ionized relativistic plasmas and thus can overcome the limitations of HHG in gases. In a SHHG experiment the laser pulse is focused to intensities providing a normalized laser vector potential

$$a = \frac{eE}{\omega m_e c} = \sqrt{\frac{I\lambda^2}{1,37 \cdot 10^{18} \frac{Wm^2}{cm^2}}} \gg 1, \quad (1)$$

thus leading to a relativistic electron oscillation at the surface. After the solid material is ionized by prepulses or the rising slope of the main pulse, a dense plasma-vacuum boundary exceeding the critical density is created and reflects the incident laser pulse. For relativistic intensities

the dominant process of harmonic generation is attributed to a periodic phase modulation during the reflection off the oscillating surface. This simplified but intuitive model is often referred to as the "relativistically oscillating mirror" (ROM) and describes the essential physics of relativistic SHHG. It predicts a power law for the spectral distribution of the emitted harmonics

$$\eta(\omega) \propto \left(\frac{\omega}{\omega_0}\right)^{-\frac{3}{2}} \quad (2)$$

up to a roll-off frequency $\omega_{ro} \approx 8\gamma^3\omega_0$. From these equations high efficiencies, e.g. 10^{-4} for the 30th harmonic, are expected. Therefore SHHG in the relativistic regime is considered to be a promising source of intense attosecond XUV pulses with pulse energies orders of magnitude higher than the current state-of-the-art. We have investigated several aspects of SHHG in a series of experiments.

Beam characteristics

The angular distribution of the emitted harmonic beam is recorded using a non-imaging flat-field spectrometer. For a short plasma scale length of $L_p \leq \lambda/10$, a constant ($1/e^2$)-divergence of about 20 mrad is found for ROM harmonics. The scale length was controlled by the laser pulse contrast that was enhanced by an anti-reflection (AR) coated plasma mirror target. In order to generate a scale length of $L_p \approx \lambda/5$, BK7 glass substrates are used as plasma mirror targets. A spectral double peak structure of the harmonic lines was observed for the longer scale length (s. Fig. 1); an effect, that originates from a stronger denting for smoother plasma density gradients due to the ponderomotive force [1].

Efficiency of ROM harmonics

The XUV pulse energy and efficiency of SHHG is investigated using an imaging XUV spectrometer that was calibrated at a synchrotron facility. A strong influence of the plasma scale length is found in experiments using different plasma mirror targets for contrast enhancement. Until now, it had generally been accepted that achieving sufficiently steep density gradients for ROM harmonics is the major challenge for the realization of an efficient SHHG XUV source. Hence, one would expect the harmonic yield to increase as the prepulse level is reduced. Surprisingly, the strongest harmonic emission is observed for intermediate contrast settings using the BK7 plasma mirror (s. Fig.

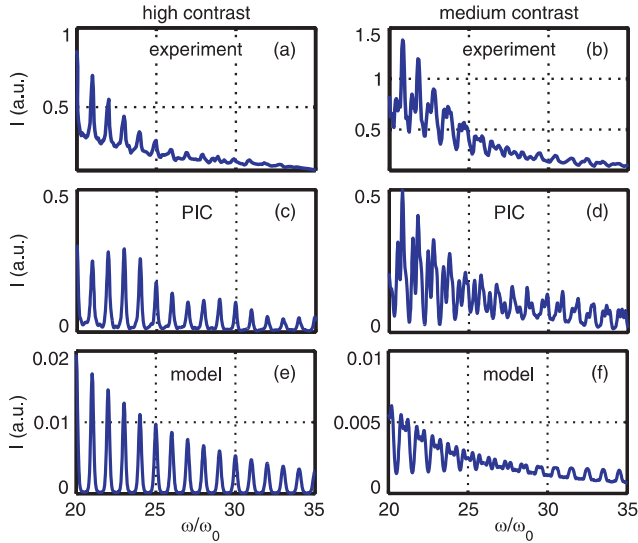


Figure 1: a) A typical ROM spectrum using high contrast shows sharp harmonic lines. b) For intermediate contrast settings and thus a longer plasma scale length the harmonic emission is much stronger and shows a double-peaked substructure. c+d) Particle-in-Cell simulations clearly confirm the observations. A closer look in the plasma simulations provides evidence that the surface plasma gets strongly curved by the ponderomotive pressure for the longer scale length case. This means that the emitted attosecond pulse train is unequally spaced. e+f) An analytical model is in excellent agreement with the findings on the spectral substructure.

2), e.g. $2.7 \mu\text{J}$ for the 21st harmonic (equivalent to an efficiency of 10^{-5}). At higher contrast, obtained by using an anti reflection coated plasma mirror, only $0.3 \mu\text{J}$ for the 21st harmonic and an efficiency of 10^{-6} are achieved. This is the first experimental evidence for the reduction of the absolute harmonic yield in the limit of ultra-steep density gradients. Our findings are confirmed by 1D PIC simulations. Theoretically, this reduction is explained by two effects. First, for steep gradients there is a larger restoring force acting on the oscillating plasma surface. Thus, the amplitude and velocity of the ROM are reduced, leading to lower harmonic efficiency. Second, the driving E-field at the critical plasma density itself is more and more reduced for shorter scale lengths as a result of the inhomogeneous wave equation. Consequently, the harmonic efficiency can be optimized by careful control of the laser pulse contrast and the resulting plasma scale length [2].

Generation of $10 \mu\text{W}$ ROM harmonic radiation at a repetition rate of 10 Hz

In another experiment relativistic surface harmonics were created using the second harmonic of the JETI laser. Second harmonic pulses with a pulse energy of 100 mJ are focused to relativistic intensity onto a rotating glass

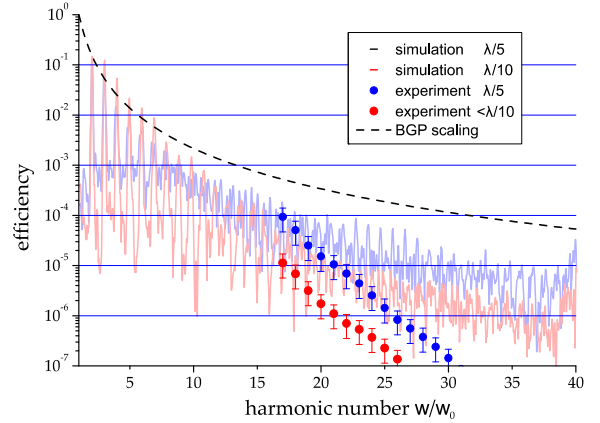


Figure 2: Experimental efficiencies (circles) are compared to spectral densities from 1D PIC simulations (lines) for different plasma scale lengths (density $n_e = 200n_c$, exponential density profile). The experimental efficiencies have been normalized to a pulse energy of 250mJ (energy that is focused to $a_0 > 1$). In the ultra-relativistic limit the efficiency is given by eq. (2).

surface such that the 10-Hz repetition rate of the laser system is exploited [3]. XUV pulse energies in the order of microjoules in the spectral range between 51 nm to 26 nm are consecutively measured, resulting in a total average power of $12.3 \mu\text{W}$ for the observed harmonic emission. The respective efficiencies are in the order of 10^{-5} to 10^{-7} . Nevertheless, it has to be admitted that the efficiency of ROM harmonics under the present conditions falls behind expectations created by theoretical results valid in the ultra-relativistic limit (eq. (2)). Apparently, the relativistically oscillating mirror is only at the onset of being driven efficiently in the relativistic regime. On the other hand, the first demonstration of ROM harmonic generation at the laser repetition rate establishes a compact source of high-intensity XUV pulses that are, suitable, e.g. for experiments on nonlinear attosecond experiments or for seeding of XUV free-electron lasers.

This project collaborates with a university project funded by DFG. The emphasis of that project is the attosecond time structure of surface harmonics.

References

- [1] M. Behmke et al.: *Controlling the Spacing of Attosecond Pulse Trains from Relativistic Surface Plasmas*, Phys. Rev. Lett. 106, 185002 (2011).
- [2] C. Rödel et al.: *Harmonic Generation from Relativistic Plasma Surfaces in Ultra-steep Plasma Density Gradients*, submitted, preprint available at arXiv:1205.6821
- [3] J. Bierbach et al.: *Generation of $10 \mu\text{W}$ relativistic surface high harmonic radiation at a repetition rate of 10 Hz*, New Journal of Physics 14, 065005 (2012).

Polarization effects detected with the high purity x-ray polarimeter

K.S. Schulze^{1,2}, B. Marx², I. Uschmann^{1,2}, E. Förster^{1,2}, G.G. Paulus^{1,2}, and T. Stöhlker¹

¹Helmholtz-Institut Jena, Germany; ²Institut für Optik und Quantenelektronik, FSU Jena, Germany.

With the help of the Jena x-ray polarimeter we measured the highest polarization purity that has ever been measured in the x-ray range in 2010 [1]. The reason for developing such a polarimeter is a QED experiment that is planned in the future, namely the detection of vacuum birefringence [2]. For that experiment, a laser with more than one petawatt peak power is required to induce birefringence into the vacuum. Short x-ray pulses which are very well polarized, are required to measure the expected small birefringence. In addition, the resulting ellipticity has to be measured with a very sensitive analyzer. The high purity that we have reached with our polarimeter enables other high sensitive polarization measurements what we demonstrated in 2011. For example, we measured the polarization state of the undulator radiation of the PETRA III P01 beam line with a high precision. Furthermore we investigate different materials between polarizer and analyzer to detect their influence on the polarization state of x-ray radiation. One sample was Kapton® that was chosen because of its common application as window or substrate in the x-ray range. We use a Kapton® sample that shows a strong optical activity in the visible spectral range (rotation of the linear polarization of about 10° in a $50\mu\text{m}$ thick foil). In the x-ray range, we have observed an ellipticity of about $3 \cdot 10^{-10}$ per foil that is caused by circular dichroism, also a kind of optical activity. Although the value is very small, the influence on the polarization has to be considered when vacuum pipes or samples with Kapton® windows are placed inside the polarimeter.

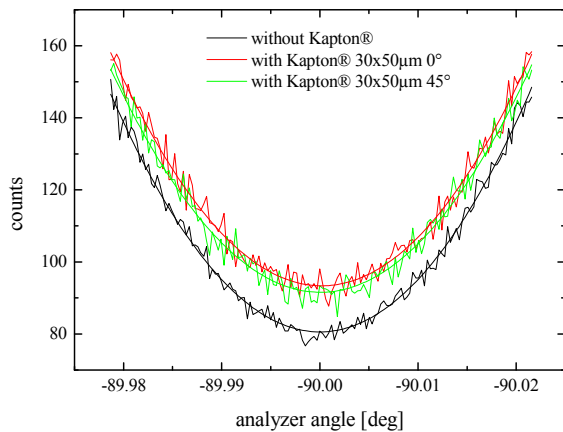


Figure 1: Intensity variation near suppression with and without a stack of 30 Kapton foils inside the polarimeter

In addition, we have investigated the influence of crystal deformations on the polarization state of x-rays that are transmitted through the sample. This deformation can be induced by bending the crystal or by the piezoelectric effect. The latter is displayed in figure 2 where a quartz crystal oscillator was placed inside the polarimeter. Resonant oscillations inside the quartz lead to a shift and a broadening of the detected curve in comparison to the undisturbed crystal. This intensity variation can be used to switch or modulate x-rays and is to be more investigated in the future.

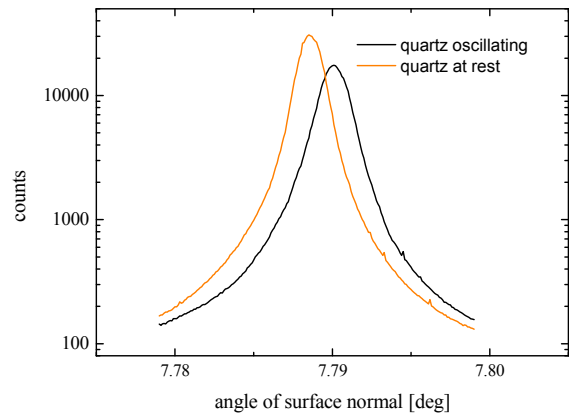


Figure 2: Intensity variation behind the polarimeter when a quartz crystal oscillator is slightly rotated near a Bragg reflection.

References

- [1] B. Marx, I. Uschmann, S. Höfer, R. Löttsch, O. Wehrhan, E. Förster, M. Kaluza, T. Stöhlker, H. Gies, C. Detlefs, T. Roth, J. Härtwig, and G.G. Paulus, “Determination of high purity polarization state of X-rays”, *Optics Communications* 284 (2011) 915-918
- [2] T. Heinzl, B. Liesfeld, K. Amthor, H. Schwöerer, R. Sauerbrey, A. Wipf, “On the observation of vacuum birefringence”, *Optics Communications* 267 (2006) 318-321

Properties of the bremsstrahlung linear polarization in polarized electron-atom collisions*

R. Martin^{1,2}, R. Barday³, J. Enders³, Y. Fritzsche³, U. Spillmann², A. Surzhykov^{2,4}, G. Weber^{1,2}, V. A. Yerokhin^{2,4,5}, and Th. Stöhlker^{1,2,4}

¹Helmholtz-Institut Jena, Germany; ²GSI Helmholtzzentrum Darmstadt, Germany; ³TU Darmstadt, Germany; ⁴Universität Heidelberg, Germany; ⁵Saint-Petersburg State Polytechnical University, Russia

Electron-atom bremsstrahlung is one of the most important x-ray production processes. Of particular interest is the investigation of how the photon polarization is affected if the incident electrons are themselves spin-polarized. The analysis of such a polarization transfer may reveal unique knowledge on the relativistic photon-matter interaction. While the underlying polarization correlations were already theoretical studied in the 70s [1] and have recently been revisited [2], an experimental study of the polarization transfer from incident polarized electrons to the emitted x-rays was for a long time hampered by the lack of appropriate sources for the production of polarized electrons in combination with efficient hard x-ray polarimeters. Hence the influence of longitudinal electron polarization on the orientation of the linear polarization axis of the bremsstrahlung photons has been measured only recently [3].

In a follow-up study, we applied a dedicated Si(Li) Compton polarimeter [4] in order to determine for the first time the complete linear polarization properties, i.e. the degree of the linear polarization and the orientation of the polarization axis, for different bremsstrahlung photon energies arising from transversely polarized electrons. The experiment has been performed at the test stand of the polarized electron source SPIN at the TU Darmstadt [5]. The source provides electrons with a kinetic energy of 100 keV and a high degree of electron polarization (in our case $76 \pm 5\%$). In addition to the measurement using transversely polarized electrons a reference measurement using unpolarized electrons has been performed. Figure 1 shows the azimuthal distributions of Compton-scattered photons inside the polarimeter for both settings of the electron spin orientation. Here, a thin gold foil target was used and the detector was located at an observation angle of 130° . As seen, the distribution recorded for transversely polarized electrons (squares) is shifted on the φ axis in comparison to the reference data (circles) which has been recorded for an unpolarized electron beam. This shift is equivalent to a rotation of the polarization axis which is a clear indication for the influence of a spin polarization of the incident electrons. At the same time the distribution measured using the transversely polarized electrons exhibits a stronger anisotropy which can be attributed to a higher degree of linear polarization of the emitted x-rays in comparison to the

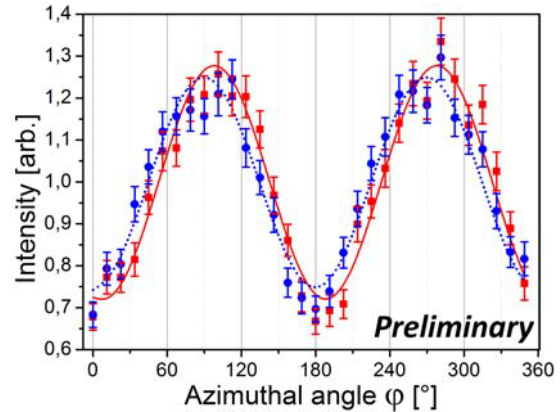


Figure 1: Projection of Compton scattering distribution on the azimuthal angle φ for the bremsstrahlung energy of 86.5 ± 3 keV. The circles show the experimental results for an unpolarized electron beam and the dashed line indicates a fit of the Klein-Nishina equation. The squares represent the data for transversely polarized electrons. The solid line shows the respective result of the fit.

unpolarized electron case. To obtain quantitative results for the bremsstrahlung linear polarization a modified version of the Klein-Nishina formula [6] was adjusted to the Compton scattering distribution (cf. solid and dashed line in Figure 1). According to this procedure, the degree of the linear polarization P_L of the bremsstrahlung photons is increased from 28% to 31% while the axis of the polarization is rotated by an angle of $\Delta\varphi = 8^\circ$. It should be noted that for a reliable comparison to theoretical predictions further corrections and effects, such as multiple scattering of the electrons in the target foil, has to be taken into account. Nevertheless, even the uncorrected experimental findings clearly indicate the influence of the incident electron spin polarization and deliver two separate experimental probes to study the polarization transfer in electron-atom collisions.

References

- [1] H. K. Tseng and R. H. Pratt, Phys. Rev. A **7**, 1502 (1973).
- [2] V. A. Yerokhin, and A. Surzhykov, Phys. Rev. A **82**, 062702 (2010).
- [3] S. Tashenov et al., Phys. Rev. Lett. **107**, 173201 (2011).
- [4] G. Weber et al., JINST **5**, C07010 (2010).
- [5] C. Heßler et al., Conf. Proc. EPAC08, 1482 (2008).
- [6] O. Klein and Y. Nishina, Z. Physik **52**, 853 (1929).

* Work supported by DFG through SFB 634 and by the state of Hesse through the LOEWE center HIC for FAIR and by the Helmholtz Gemeinschaft (Nachwuchsgruppe VH-NG-421).

PEBSI - A Monte Carlo simulator for polarized-electron bremsstrahlung*

G. Weber^{1,2}, R. Martin^{2,3}, A. Surzhykov^{2,3}, M. Yasuda⁴, V. A. Yerokhin^{5,2,3}, and Th. Stöhlker^{1,2,3}

¹Helmholtz-Institut Jena, Germany; ²GSI, Darmstadt, Germany; ³Universität Heidelberg, Germany; ⁴Osaka Prefecture University, Japan; ⁵St. Petersburg State Polytechnical University, Russia

Electron-atom bremsstrahlung, also referred to as ordinary bremsstrahlung, is one of the basic photon-matter processes and has attracted continuous interest both theoretically and experimentally during the last decades [1, 2, 3]. Of particular importance is the study of the bremsstrahlung polarization properties resulting from polarized electrons as it reveals subtle details of the so-called polarization transfer, i.e. a modified degree of linear polarization and a rotation of the polarization axis, from charged particles to the emitted x-rays [4]. Recently, a series of polarization-resolved bremsstrahlung measurements has been carried out at the test stand of the polarized electron source SPIN [5] at the TU Darmstadt. In these experiments the polarization transfer was studied in collisions of polarized electrons with gold foils of about $100 \mu\text{g}/\text{cm}^2$ thickness and at an impact energy of 100 keV [6, 7].

A crucial point when drawing conclusions from the experimental data is the question to what extent the bremsstrahlung characteristics, in particular concerning the polarization, are altered by effects due to multiple collisions inside the target. One can expect that the linear polarization shows a high sensitivity to the target thickness as the straggling of incident electrons followed by bremsstrahlung emission leads to a superposition of different degrees of polarization and polarization orientations, resulting in a decrease of the degree of linear polarization and a modified orientation of the polarization axis. To quantify these effects, the Monte Carlo code PEBSI (Polarized Electron Bremsstrahlung Simulator) was developed for modeling the bremsstrahlung arising from polarized electrons during their passage through matter [8].

Indeed, preliminary calculations show that for the target thicknesses of interest the straggling of the electrons within the target foils leads to a significant reduction of both the degree of linear polarization P_L and the rotation of the polarization vector $\Delta\chi$. As an example, we present in Fig. 1 the degree linear polarization and the rotation of the polarization axis of bremsstrahlung stemming from polarized electrons with an kinetic energy of 100 keV impinging on a thin gold foil. We assumed the electron polarization to be oriented perpendicular to the incident electron direction (transversal polarization) and to lie within the reaction plane, being defined by the incident electron momentum and the direction of the emitted photon. It is interesting to note that while the value of P_L significantly decreases with decreasing photon energy, the rotation angle $\Delta\chi$ exhibits only a very weak dependence on the bremsstrahlung en-

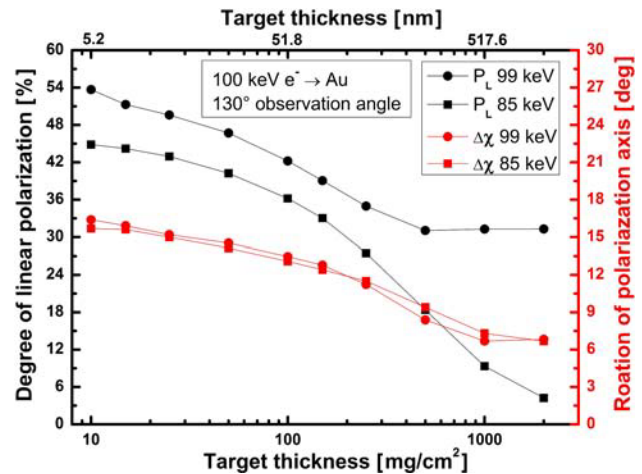


Figure 1: Preliminary PEBSI results for the degree of linear polarization and the orientation of the polarization axis for bremsstrahlung arising from polarized electrons impinging on a gold foil of various thicknesses. The bremsstrahlung is emitted at an angle of 130° with respect the incident electron direction and two photon energies at the high-energy end of the bremsstrahlung distribution are considered.

ergy. Moreover, for the highest photon energy considered, the degree of linear polarization remains constants for target thicknesses above $500 \mu\text{g}/\text{cm}^2$.

Summarizing, according to the presented PEBSI results, a rigorous analysis of polarization-resolved bremsstrahlung measurements using high-Z solid-state target foils has to take into account the effects of electron straggling on the bremsstrahlung properties.

References

- [1] W. Nakel, Phys. Rep. **243**, 317 (1994).
- [2] C. A. Quarles, Rad. Phys. Chem. **59**, 159 (2000).
- [3] C. A. Quarles and S. Portillo, Rad. Phys. Chem. **75**, 1187 (2006).
- [4] V. A. Yerokhin and A. Surzhykov, Phys. Rev. A **82**, 062702 (2010).
- [5] C. Heßler et al., Proceedings of EPAC08 (2008).
- [6] R. Martin et al., AIP Conf. Proc. **1336**, 94 (2011).
- [7] S. Tashenov et al., Phys. Rev. Lett. **107**, 173201 (2011).
- [8] G. Weber et al., Nucl. Inst. Meth.B. in print.

* Work supported by the Helmholtz Gemeinschaft (Nachwuchsgruppe VH-NG-421).

Time resolved x-ray diffraction on indium antimonide (InSb) crystals

S. Höfer¹, Tino Kämpfer^{1,2}, Ingo Uschmann^{1,2}, Eckhart Förster¹

¹HIJ, Jena, Germany; ²IOQ, Jena, Germany

Introduction

We present recent results on probing InSb crystals by time resolved x-ray diffraction after ultra short excitation by an infrared femtosecond laser pulse. By using extreme asymmetric Bragg diffraction the probing penetration depth of the x-rays of about 100 atomic layers was adapted to the penetration depth of the exciting laser radiation. The high temporal resolution of the experiment was achieved by using a tabletop kHz laser plasma source as a x-ray source. The pulse duration of this source is expected to be shorter than 200 fs ($1 \text{ fs} = 10^{-15} \text{ s}$) [1].

Experiment

The exit laser beam is split in two beams, the weaker one (0.7 mJ) excites the InSb as pump and the stronger one (3.5 mJ) generates short x-ray pulses on the titanium foil. These x-ray Ti-K_α photons are focused to the InSb crystal by a toroidally bent 400 GaAs crystal (Fig.1). The diffracted x-ray photons are collected by a CCD. The pump beam is tilted only a few degrees to the x-ray beam, to reduce temporal smearing of the pulses. The probe is a polished InSb crystal with a 111 surface. The sample was not moved within the experiment and no damage occurs after 12 hours, at the used flux of 10 mJ/cm^2 . The measurements of all delays were repeated 10 times.

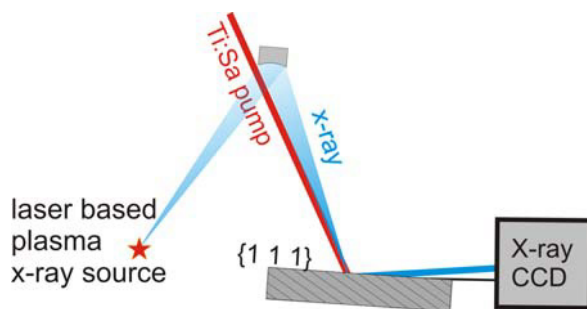


Figure 1: Experimental setup, with strong asymmetry

Experimental results

In the case of the strong asymmetric 220 reflection the absorption depth of the optical pump and the x-ray probe are 60 nm. 5 ps after laser excitation the rocking curve clearly changes. After 50 ps the full rocking curve are displaced, this denotes to a homogeneous heating of the pumped surface volume. At later times the rocking curve moves back, due to recombination in the crystal (Fig. 2).

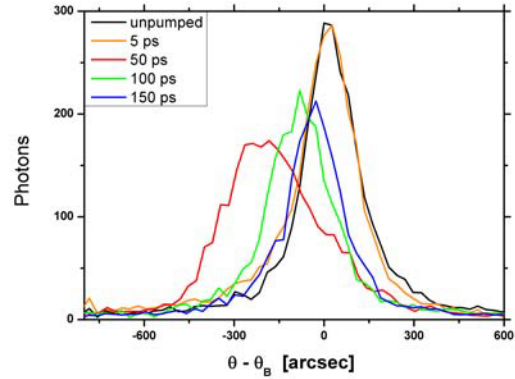


Figure 2: Measured rocking curves for the strong asymmetric 220 reflection, at different time delays.

In the second case with the asymmetric 113 reflection, the absorption depth of the x-rays is six times larger than the depth of the laser pump pulse. The strain wave propagates with the sound speed (3880 m/s) in the crystal; it takes more than 100 ps to excite the full probed volume. After 150 ps the probed volume is fully expanded, but the surface has already recombined (Fig. 3).

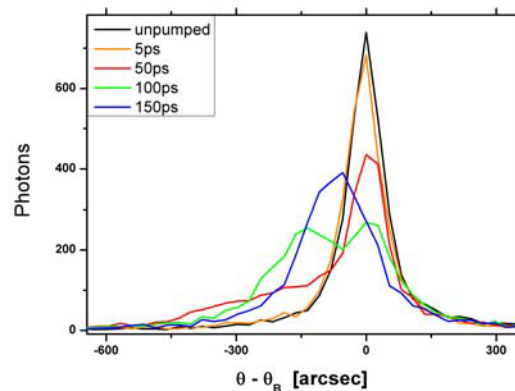


Figure 3: Measured rocking curves for the asymmetric 113 reflection, at different time delays.

Conclusion

The experimental data will allow us to find a better theoretical model which considers fast coupling of the excited electrons to the lattice as well as recombination of the lattice [2].

References

- [1] Ch. Reich, P. Gibbon, I. Uschmann, E. Förster, Phys. Rev. Lett. 84, 21 (2000).
- [2] A. Morak, T. Kämpfer, I. Uschmann, A. Lübcke, E. Förster, R. Sauerbrey et al.: phys. stat. sol. 243, No.12 (2006).

Laser-excited acoustical phonons in germanium probed by ultrashort pulses from a laser-driven x-ray diode

T. Kämpfer^{1,2}, K. S. Schulze^{1,2}, I. Uschmann^{1,2}, S. Höfer^{1,2}, R. Loetzsch^{1,2} and E. Förster¹

¹ Helmholtz-Institut Jena, Fröbelstieg 3, D-07743 Jena, Germany; ² Institut für Optik und Quantenelektronik, Friedrich-Schiller-Universität Jena, Max-Wien-Platz 1, D-07743 Jena, Germany

During the last years a new source of ultrashort x-ray pulses - a laser-driven x-ray diode - has been developed in the x-ray optics group. In 2011 we have demonstrated that this source can be used for time-resolved x-ray diffraction experiments on a picosecond timescale [1]. This kind of x-ray source shows, compared to all other laboratory sources (e.g. laser-plasma sources [3]), some advantages in terms of stability and laser requirements because it combines the function of a conventional x-ray tube with the short pulse laser technique. The experimental setup is shown in Figure 1. A silver cathode is illuminated by the frequency doubled beam of a titanium:sapphire amplifier. The emitted pulse of photoelectrons is accelerated to a titanium anode where hard x-rays (characteristic lines and bremsstrahlung) are generated. The emitted Ti- K_{α} radiation is focused by a toroidally bent crystal onto a germanium sample and the rocking curve of its 004 reflection is recorded by an x-ray CCD.

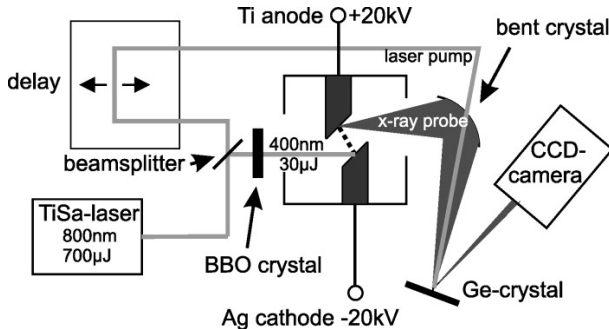


Figure 1: Experimental setup for time-resolved x-ray diffraction with a laser-driven x-ray diode.

The main part of the fundamental laser beam can be used to excite the sample at variable delays with respect to the x-ray probe. Experimental results are shown in Figure 2b. A few tens of picoseconds after laser-excitation, a deformation of the rocking curve is observed. This expansive deformation of the lattice (strain wave, Figure 2a) moves forward into the crystal with the longitudinal speed of sound.

The experimental results are in accordance with calculations of the processes involved by a microphysical model [2]. Hence the creation of the strain wave can be described in the following way: (1) absorption of photons and carrier excitation, (2) diffusion and scattering of carriers, (3) carrier relaxation due to Auger recombination, (4) energy transport to optical phonons due to carrier-phonon scattering, (5) phonon-phonon scattering and excitation of acoustical phonons, and (6) deformation of the lattice due to acoustical phonons.

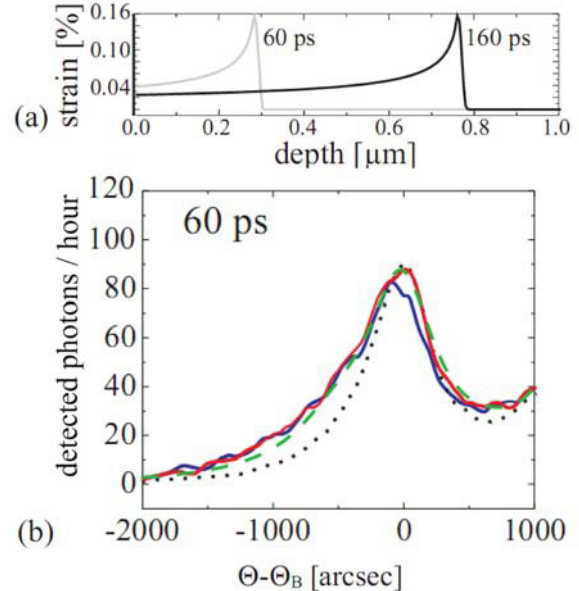


Figure 2: (a) Calculated strain profiles for two different delays after laser excitation. (b) Measured and simulated rocking curves, dotted: without excitation, solid: with excitation (blue: 1 h acquisition, red: 5 h acquisition), dashed: simulation.

Furthermore, the very good stability of the x-ray diode allows the measurement of absolute reflectivity changes (not shown), which are consistent with calculations of x-ray diffraction from the strained lattice. In long term operation, the source allows acquisition times of hours, days or even weeks without interruption.

With the help of state-of-the-art fiber lasers, the brightness of the source can be increased by two orders of magnitude while at the same time the stability increases due to the turnkey operation of the laser.

References

- [1] K. S. Schulze, T. Kämpfer, I. Uschmann, S. Höfer, R. Loetzsch, E. Förster, *Applied Physics Letters* 98 (2011), 141109 1-3.
- [2] A. Morak, T. Kämpfer, I. Uschmann, A. Lübcke, E. Förster, and R. Sauerbrey, *Phys. Status Solidi B* 243 (2006), 2728.
- [3] I. Uschmann, T. Kämpfer, F. Zamponi, A. Lübcke, U. Zastra, R. Loetzsch, S. Höfer, A. Morak, and E. Förster, *Appl. Phys. A* 96 (2009), 91.

Optical Coherence Tomography using broad-bandwidth XUV and soft x-ray radiation

S. Fuchs^{1,2}, *A. Blinne*², *C. Rödel*^{1,2}, *U. Zastrau*², *V. Hilbert*², *M. Wünsche*², *J. Bierbach*^{1,2},
E. Förster^{1,2}, and *G. G. Paulus*^{1,2}

¹Helmholtz-Institute Jena, Helmholtzweg 4, 07743 Jena, Germany; ²Institute of Optics and Quantum Electronics, Friedrich-Schiller University of Jena, Max-Wien-Platz 1, 07743 Jena, Germany

We present a novel approach to extend optical coherence tomography (OCT) to the extreme ultraviolet (XUV) and soft X-ray (SXR) spectral range. As a consequence, the theoretical resolution limit of XUV coherence tomography (XCT) is in the order of nanometers. We performed simulations and proof-of-principle experiments at synchrotron sources and found the expected properties concerning resolution and penetration depth confirmed.

Introduction

Optical coherence tomography (OCT) is a well-established method to retrieve three-dimensional, cross-sectional images of biological samples in a non-invasive way using near-infrared radiation. The axial resolution of OCT is in the order of the coherence length $l_c \propto \lambda_0^2 / \Delta\lambda_{\text{FWHM}}$ which depends on the central wavelength λ_0 and the spectral width (FWHM) $\Delta\lambda_{\text{FWHM}}$ of a light source. As a consequence, the axial resolution only depends on the spectrum rather than the geometrical properties of the radiation. OCT with broadband visible and near-infrared sources typically reaches axial (depth) resolutions in the order of a few micrometers [1]. Within the last decade and in conjunction with the quickly developing sector of advanced material design, the scale length of interest has dropped from micrometers to a few nanometers. The investigated method presented here takes advantage of the fact that the coherence length can be significantly reduced if broadband XUV and SXR radiation is used.

Microscopy using XUV and SXR radiation has regularly ineluctable practical restrictions imposed by the optics and sources available in this regime. Coherence tomography with short wavelength has the potential to circumvent some of these limitations. A major limitation of XUV radiation is the absorption within a few tens or hundreds of nanometers depending on the actual composition of the material and the wavelength range. Consequently, XUV coherence tomography (XCT) can only display its full capabilities when used in the transmission windows of the sample materials. For instance, the silicon transmission window (30-99 eV) corresponds to a coherence length of about 12 nm assuming a rectangular spectrum and an absorption length of about 200 nm, thus suggesting applications for semiconductor inspection. In the water

window at 280-530 eV as defined by the K absorption edges of carbon and oxygen, respectively, a coherence length as short as 3 nm can be achieved and highlights possible applications of XCT for life sciences.

In preparation for a proof-of-principle experiment, we performed simulations based on the matrix-algorithm. The spectral reflectivity of layer-structured samples was calculated in order to investigate the imaging properties of XCT with respect to resolution and penetration depth [2].

Setup

Typically, a OCT device in the near-infrared spectral range consists of a Michelson-type interferometer in which one mirror is the sample [3]. The image can be captured by measuring the spectral intensity of each component of the broad bandwidth light source (Fourier-domain OCT) or by scanning the reference arm length of the interferometer (time-domain OCT). However, the realization of a classical Michelson interferometer in the XUV regime is highly demanding. The short wavelengths call for extraordinary precision with respect to the flatness of optical surfaces including beam splitters. In order to overcome these problems, we use a variant of Fourier-domain OCT setup called common-path Fourier-domain OCT [4]. The reference wave and the sample wave share the same path, see Fig. 1.

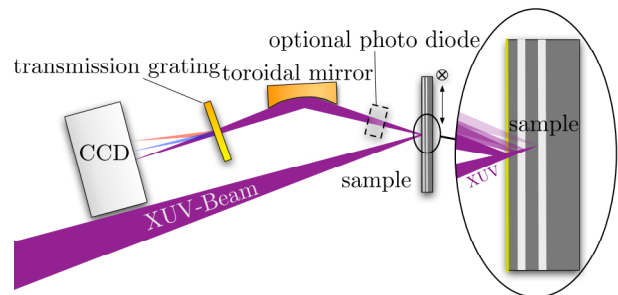


Figure 1: Proposed common-path Fourier-domain OCT setup in the XUV spectral range.

Strikingly, using this variety of OCT, a beam splitter can be completely avoided [5]. For a proof-of-principle setup broadband synchrotron light was focused on the surface of the sample. The samples are one-dimensional structured

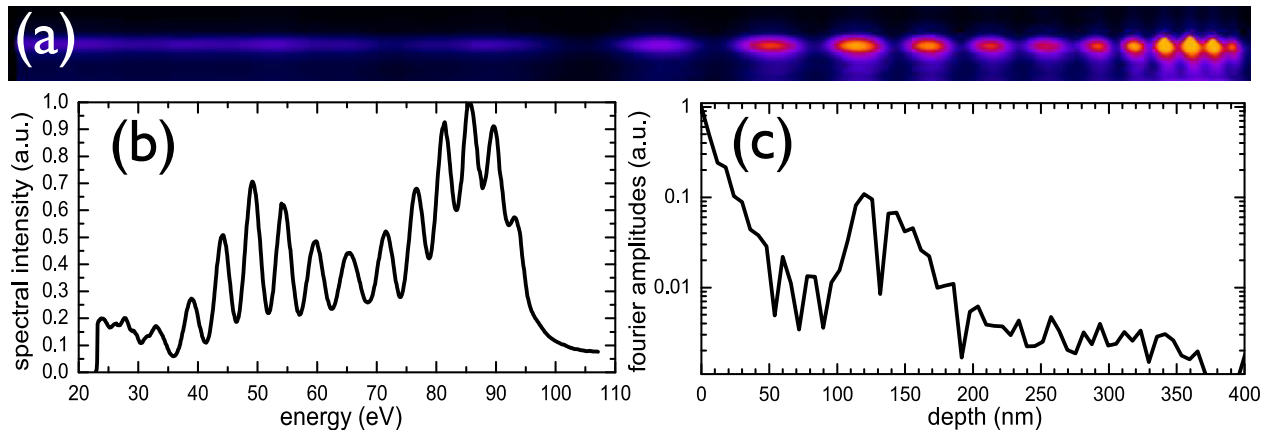


Figure 2: XCT signal of two 5-nm gold layers separated by a silicon layer, buried under 120 nm silicon and a gold top layer. (a) CCD image of the grating spectrometer, (b) lineout from (a) and rescaled to energy units, (c) fourier transform of (b) shows depth structure of the sample

layer systems consisting of materials with sufficient absorption lengths in the spectral ranges used, e.g., silicon or boron carbide. The reflected intensity is measured either with a grating spectrometer, consisting of a gold transmission grating and a toroidal mirror (spectrometer-based OCT) [6], or with a photo diode (swept-source OCT). However, the reference arm of the interferometer is not easily accessible in our setup. Instead, the top layer reflection assumes the role of a reference beam. In order to better distinguish the top layer reflection from inner layer reflections, a thin, strongly reflecting top layer (e.g. 5 nm gold) was added to the sample. Merely a Fourier transform of the reflected spectrum needs to be computed for retrieving the structural information. A 3D image can be captured by scanning the focus point over the sample.

Measurement

Layer-structured samples were designed and fabricated in cooperation with the Fraunhofer Institute for Applied Optics and Precision Engineering in Jena. Different samples consisting of silicon, gold, platinum, and boron carbide layers with different thicknesses were investigated at the Helmholtz centres DESY (Deutsches Elektronen-Synchrotron, Hamburg) and BESSY (Berliner Elektronenspeicherring-Gesellschaft für Synchrotronstrahlung) in the water and silicon transmission window. Both swept-source OCT with a photo diode and spectrometer-based OCT with the grating spectrometer were performed. We found the expected values in resolution and penetration depth confirmed.

In Fig. 2 a XCT-signal of two 5-nm gold layers separated by a silicon layer, buried under 120 nm silicon and a gold top layer is shown. The spectrum was recorded with a grating spectrometer. It can be seen that the peak width is about 15 nm, which corresponds to the coherence length of broadband radiation in the silicon transmission window.

The two peaks at 120 nm and 140 nm represent the two buried gold layers and they clearly appear separated from each other.

Conclusion

We report on the extension of Optical Coherence Tomography using extreme ultraviolet and soft x-ray radiation and thus increased the resolution of OCT from micrometers to a few nanometers. The experimental results strongly suggests its application as a new non-invasive tomographic method to investigate nanometer-scale structures of layered systems and simple three-dimensional samples by lateral raster scanning.

References

- [1] D. Huang et al., "Optical coherence tomography," *Science* **254**, 1178-1181 (1991).
- [2] S. Fuchs et al., "Optical coherence tomography using broadband XUV and soft X-ray radiation," *Appl. Phys. B* **106**, 789-795 (2012).
- [3] W. Drexler and J. G. Fujimoto, *Optical Coherence Tomography* (Springer Verlag, Berlin, 2008).
- [4] A. B. Vakhtin et al., "Common-path interferometer for frequency-domain optical coherence tomography," *Appl. Opt.* **42**, 6953-6958 (2003)
- [5] G. G. Paulus and C. Rödel, "Short-wavelength coherence tomography," (US Patent 20080212075)
- [6] S. Fuchs et al., "Sensitivity calibration of an imaging XUV spectrometer-detector system for high intensity laser experiments," *submitted*.

Laser Driven X-ray Radiography on Warm Dense Matter*

*D. C. Hochhaus^{1,2,3,#}, B. Aurand^{1,4}, M. Basko^{1,8}, B. Ecker^{4,6}, T. Kühl^{2,4}, T. Ma⁷, F. Rosmej⁵,
B. Zielbauer^{2,6}, D. Zimmer² and P. Neumayer^{1,3}*

¹EMMI, Darmstadt; ²GSI, Darmstadt; ³FIAS, Frankfurt; ⁴University of Mainz, Mainz;
⁵UPMC, Paris, France; ⁶HIJ, Jena; ⁷LLNL, Livermore, USA; ⁸ITEP, Moscow, Russia

Matter at high energy density (HED), at pressures exceeding 1 Mbar, is prevalent in many compact astrophysical objects. In the laboratory HED matter can be generated by use of high-intensity drivers, such as powerful lasers or heavy ion facilities. This offers the opportunity to test modelling of dense matter properties, such as the equation-of-state or opacities.

Using GSI's high-energy short-pulse laser facility PHELIX we have recently employed hot electrons to isochorically heat solid density matter. Upon laser irradiation of matter at relativistic intensities ($>10^{18}\text{W/cm}^2$) about 10% of the laser energy is converted to a fraction of energetic ("hot") electrons with ranges of several 100 μm in matter at solid density. In our experiment we have irradiated Titanium wires (diameters 50 and 80 μm) with laser pulses of up to 50J of energy. The K-alpha fluorescence excited within the target by the fast electrons is recorded with an absolutely calibrated spectrometer providing a spatial resolution of 25 μm along the wire axis.

We have modelled the fast electron transport and K-alpha generation within the wire both with a 1D collisional model, where we include ohmic heating using the "rigid beam model" [1], and with the 3D hybrid PIC code ZUMA. Both models accurately reproduce the K_α emission emitted along the wire. This allows us to assess the energy deposited by the hot electrons in the bulk target. We find a temperature distribution reaching from >150 eV (wire-tip) down to ~2 eV (1000 μm from the tip).

The relaxation time of the hot electron population is of the order ps, short compared to the hydrodynamic evolution of the target. Thus the rapid heating is well separated in time from the subsequent expansion of the target.

We have employed the second laser beam of the new double-beam option of PHELIX to drive an intense hard x-ray back-lighter to take radiographic images of the exploding wire [2]. Variation of the delay between the heater and the back-lighter laser pulse allowed us to follow the wire expansion in time. Careful characterization of the x-ray back-lighter spectrum was required to determine the absolute mass density of the expanding matter for comparison of the radiographic images to radiation hydrodynamic calculations (fig. 1). The energy deposition as determined from the K_α emission was used as initial condition. Comparing simulations in 1D- and 2D-cylindrical geometry with and without radiation revealed that 2D effects as well as effects from radiation transport are negligible, and the expansion is well described as a 1D isentropic expansion.

* Work supported by EMMI and the Helmholtz Institut Jena.

[#]d.hochhaus@gsi.de

With this clean experimental realization of HED matter, these measurements hold the potential of an alternative method for testing EOS models in the WDM regime [4].

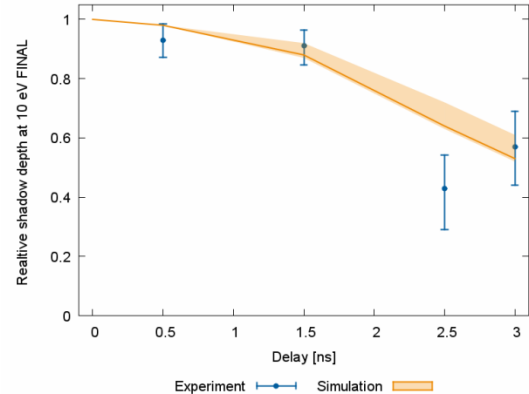


Figure 1: Comparison of radiographic shadow depth vs. 1D hydro-simulation of Titanium expanding at initially 10 eV and solid density

While the temporal and spatial resolution of the measurement are sufficient, improvements in the image signal-to-noise and back-lighter spectrum characterization are required to reduce the uncertainty of the absolute density measurement. We expect this to be feasible by shielding the intense x-ray emission from the tip of the laser irradiated wire and adding a static calibration target at the imaging plane.

To assess the potential of laser driven hard x-ray sources as back-lighters for dense plasmas created at FAIR, we have performed Monte-Carlo simulations of the back-lighter spectrum for various laser irradiation conditions. The calculations were benchmarked with results of the recent experiment on the back-lighter spectral composition. Our modelling shows that a 100J-class ps-laser driven x-ray source will provide a sufficient flux of x-ray radiation energetic enough to penetrate the high ρ -r targets as produced in HIHEX scheme

We believe this adds to the strong case for a high energy short pulse laser as diagnostic tool for plasma physics experiments at FAIR.

References

- [1] J. R. Davies, Phys. Rev. E **68**, 056404 (2003)
- [2] D.C. Hochhaus, GSI Sci. Rep. (2010)
- [3] N.A. Tahir et al., Phys. Rev. Lett. **95**, 035001 (2005)
- [4] M. E. Foord et al., Rev. Sci. Instr. **75**, 2586 (2004)

X-Ray Diffraction Topography of Optical Waveguides written in YAG Single Crystals using fs-Laser *

J. Kräußlich¹, H. Marschner², E. Förster¹, J. Siebenmorgen³, T. Calmano³, and G. Huber³

¹Helmholtz Institute of Jena, Germany; ²Institute for Optics and Quantum Electronics, University of Jena,
³Institute of Laser-Physics, University of Hamburg, Germany.

YAG single crystal specimens with laser-written waveguides were studied using X-ray diffraction methods [1]. The samples were prepared at the Institute of Laser-Physics of the University of Hamburg.

Straight-lined single and twin tracks were fabricated with femtosecond laser pulses [2, 3] in the (001)-oriented planar YAG specimens of 0.1mm thickness (Fig. 1). With ultrashort pulses energy can be transferred to the crystalline lattice of this transparent material, which results in the destruction of the lattice and a change of the refractive index. Due to the nonlinearity of the underlying absorption process the modified volume is limited to the focus of the fs-laser. This can be used to produce optical channel-waveguides and to realize highly efficient waveguide lasers in rare-earth doped YAG [3].

The main goal in this project is, to find out the microscopic correlations between lattice modifications and refractive index changes which lead to waveguiding.

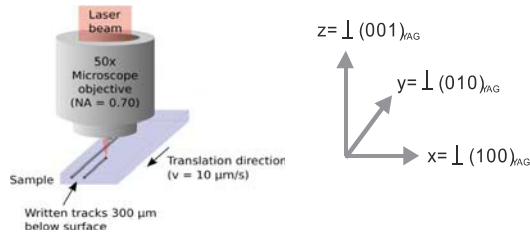


Figure 1: Principle of the laser-based structuring

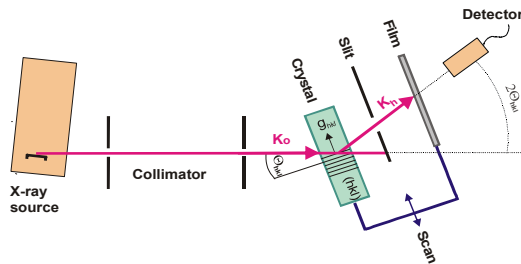


Figure 2: Experimental setup used for recording of X-ray diffraction images due to 'Lang technique'

X-ray diffraction methods respond very sensitive to crystalline lattice parameter changing. The image contrast of crystal defects in the X-ray diffraction topography is given by the relation of the diffraction vector $g_{(hkl)}$ to the inherent stress field vector components in the crystal.

$$\text{image contrast} \left. \begin{array}{l} \text{maximum} \leftrightarrow \varepsilon_i \parallel g(hkl) \\ \text{zero} \leftrightarrow \varepsilon_i \perp g(hkl) \end{array} \right\}$$

$g_{(hkl)}$ – diffraction vector

$$\varepsilon_i = \left(\frac{\Delta d}{d} \right)_{(hkl)} \text{ – elastic strain field vector components}$$

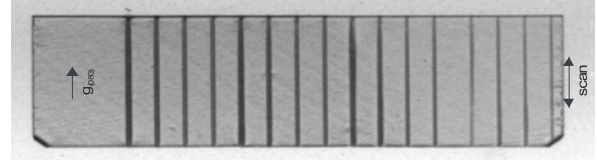


Figure 3 shows a X-ray transmission topograph recorded with $\text{AgK}_{\alpha 1}$, $\theta_{(080)} = 10.73^\circ$. The diffraction vector $g_{(080)}$ is parallel to the written tracks and horizontally lying in sample surface.

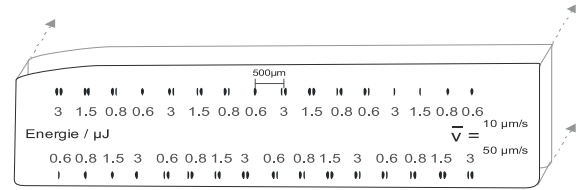


Figure 4 shows the cross section schema of the structured YAG sample with laser writing parameters.

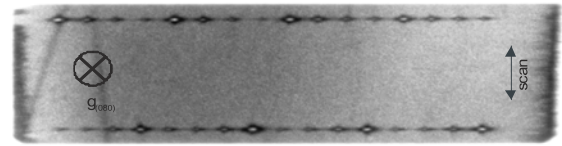


Figure 5 shows a X-ray reflection topograph recorded with $\text{AgK}_{\alpha 1}$, $\theta_{(080)} = 10.73^\circ$. The diffraction vector $g_{(080)}$ is perpendicular to the cross section surface.

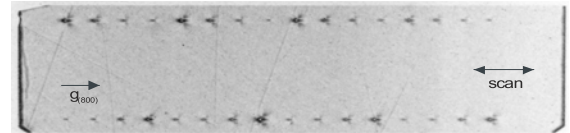


Figure 6 shows a X-ray transmission topograph recorded with $\text{AgK}_{\alpha 1}$, $\theta_{(800)} = 10.73^\circ$. The diffraction vector $g_{(800)}$ is horizontally lying in the cross section surface.

The X-ray topographs visualize qualitatively the deformation and stress fields arising by laser-based structuring. Quantitative results can be achieved by using the method of finite elements modelling.

References

- [1] D.K. Bowen and B.K. Tanner; "High Resolution X-ray Diffractometry and Topography", Taylor & Francis Ltd, (1998)
- [2] J. Siebenmorgen et al.; Appl. Phys. B (2009) **97**, 251-255
- [3] T. Calmano, J. Siebenmorgen, O. Hellmig, K. Petermann, G. Huber; Appl. Phys. B (2010) **100**, 131-135

Generation of picosecond narrow bandwidth X-ray pulses from a Laser-Thomson-Backscattering source at HZDR

A. Irman¹, A. Jochmann¹, S. Trotsenko^{2,3}, U. Lehnert¹, J.P. Couperus¹, M. Kuntzsch¹, A. Wagner¹, A. Debus¹,
H.P. Schlenvoigt¹, K.D. Ledingham⁴, T.E. Cowan¹, R. Sauerbrey¹, Th. Stöhlker^{2,3} and U.Schramm¹

¹Helmholtz Zentrum Dresden-Rossendorf, Dresden, Germany; ²GSI, Darmstadt, Germany; ³Helmholtz-Institut Jena, Jena, Germany; ⁴University of Strathclyde, Glasgow, Scotland

Intense ultrashort hard X-ray can serve as a novel tool for structural analysis of complex systems with unprecedented temporal and spatial resolution [1]. However, hard X-ray generation based on insertion devices like undulators in conventional accelerators requires GeV range electron energies and thus large installations. The most prominent examples of such sources are the X-ray free electron laser projects that are currently under construction [2].

Here, we propose the replacement of the magnetic undulator by an optical light wave and the implementation of this scheme, also well-known as the Thomson backscattering [3], at the radiation source ELBE. In this scheme, electrons oscillating in the light field emit Doppler-upshifted radiation (proportional to the square of the relativistic energy γ) into a relativistically contracted solid angle cone (proportional to $1/\gamma$) in the laboratory. Although the brilliance as well as the total number of photons expected from this process cannot compete with the XFEL approach, it should be sufficient for a number of applications where the short pulse duration and the simultaneous availability of 100 TW class laser radiation can be exploited. Pump-probe experiments analysing laser induced melting and re-crystallization or temporal X-ray probing of warm dense matter only represent a small range of applications that will be the topic of further proposals.

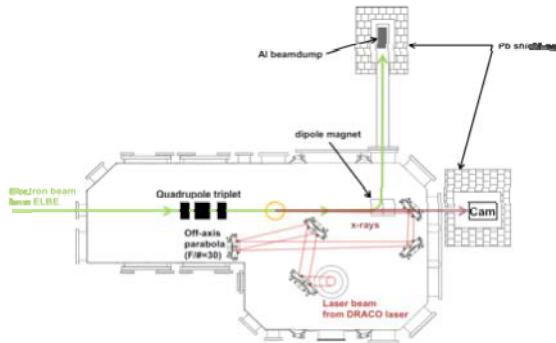


Fig. 1: Thomson backscattering experimental setup.

Experimental setup

A schematic drawing of the setup is presented in figure 2. Electron beams with energy of 24, 27 and 30 MeV and charge of 70 pC from the radiation source ELBE were transported into the interaction chamber located in room 111b of the ELBE building. Inside the chamber these electron beams were focused by a set of permanent quadrupole magnets onto the interaction point, where they collided with synchronized counter-propagating laser

beams from the DRACO Tisa laser system. The scattered X-ray photons pass a kapton window at the end of the vacuum chamber and enter the diagnostic area shielded with lead bricks. A dipole magnet was installed downstream of the interaction point to deflect the electron beams towards the electron beam dump made from a thick aluminium block.

Preliminary Results

The generated x-rays are highly collimated and can be reliably adjusted from 5.5 to 23.5 keV by tuning the electron energy (24 MeV to 30 MeV) and the laser intensity. Ensuring the spatio-temporal overlap at the interaction point and suppressing the Bremsstrahlung background we have achieved a signal to noise ratio of greater than 300. Together with the use of an x-ray camera (resolution of 250 eV FWHM) to record the x-ray beam profile (in Fig.2) and the energy spectrum (in Fig.3), we were able to resolve the angular-energy correlation and to study the influence of the beam emittance on the observed bandwidth. This experiment serves as an important step towards a compact tuneable source of ultrashort hard x-ray pulses at the ELBE.

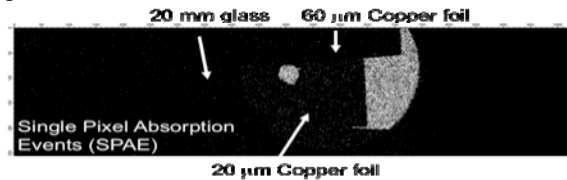


Fig. 2: The measured x-ray beam profile on the CCD.

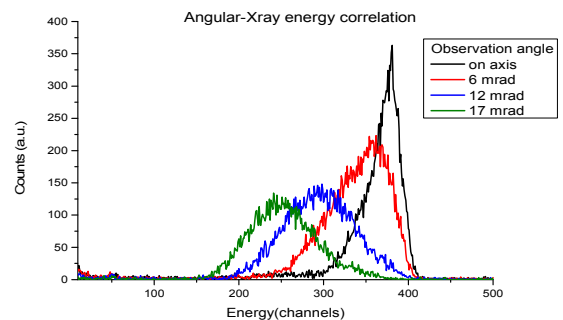


Fig. 3: Angular-energy correlation of the x-ray beams.

References

- [1] T. Guo, Laser and photonics Rev. 3, 591 (2009)
- [2] XFEL project DESY, Hamburg, Germany
- [3] E. Esarey, et al., Phys. Rev. E. 48, 3003 (1993)

Nonlinear Thomson scattering of ultraintense laser light on relativistic electrons with the account of radiation friction *

T. Schlegel¹ and V.T. Tikhonchuk²

¹Helmholtz Institute Jena, and GSI Darmstadt, Germany; ²University Bordeaux 1 - CNRS - CEA, CELIA, UMR 5107, F-33400 Talence, France

The electron dynamics in a number of simple electromagnetic wave configurations at constant normalized field strengths $a_1 > 10$ was studied recently including the effect of radiation damping [1]. This analysis has been partly motivated by the observation of strong electron deceleration in the vacuum field behind a quasistationary laser piston obtained in related Particle-in-Cell (PIC) simulations [2]. As a consequence of this electron energy loss, the cross section of laser light scattering by the electron decreases, and the radiation spectrum takes the form of a broad quasicontinuous distribution.

In this Contribution, some properties of the electron motion in ultraintense counterpropagating or comoving laser waves will be described. Thereby, the radiation friction force is used in the classical Landau-Lifshitz approximation [3]. In Fig.1 we compare the obtained analytical expressions for the electron energy, its longitudinal momentum, for the power and energy of the emitted radiation in the case of a counterpropagating wave with numerical solutions of the basic equations for several initial electron energies $\gamma_0 m_e c^2$, $\gamma_0 = \sqrt{1 + u_{x0}^2}$, and field strengths a_1 [1].

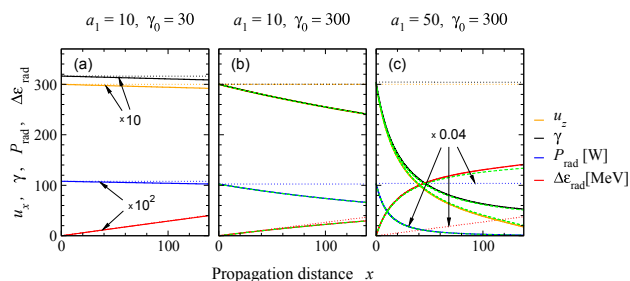


Figure 1: The power and energy of the scattered radiation, the longitudinal momentum u_x and the γ -factor of the electron versus the normalized distance of propagation in an intense counterpropagating plane laser wave. The relevant input quantities are given in the titles of panels. The numerical data without the account for radiation damping are depicted by dotted lines, the dashed green curves in panels (b) and (c) display the corresponding analytical results.

Applying the analytical estimates for $u_x(t)$ and $\gamma(t)$, an approximate expression for the radiation power,

$$P_{\text{rad}}(t) \simeq \frac{4\tau_{\mathcal{R}} a_1^2 \gamma_0^2}{(1 + 4\tau_{\mathcal{R}} a_1^2 \gamma_0^2 t)^2} \quad (1)$$

* Work supported by the Region Aquitaine under project No. 34293, by the European support program Marie Curie IRSES project # 230777, and by EURATOM in the framework of keep-in-touch activities

may be deduced, with the dimensionless damping constant $\tau_{\mathcal{R}} \simeq 1.5 \times 10^{-8}$. Its time integral gives the emitted radiation energy $\Delta \varepsilon_{\text{rad}}$. Panels (b) and (c) of Fig.1 show good agreement of the analytical estimates with numerical results. They demonstrate reduced nonlinear Thomson scattering in the case of essential radiation friction. For a small damping effect, the time-dependent term in the denominator may be skipped, and we get the well-known expression $P_{\text{rad}} = 4\tau_{\mathcal{R}} a_1^2 \gamma_0^2$ [4].

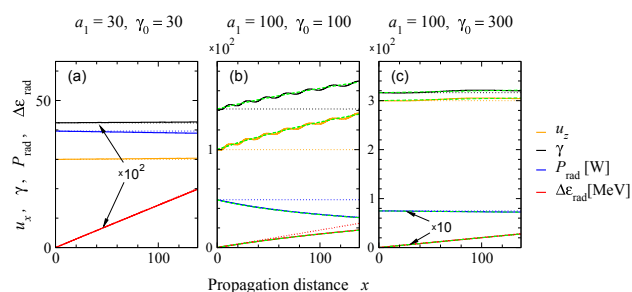


Figure 2: Same dependencies as in the previous figure but for an electron moving in a copropagating plane laser wave. The relevant input quantities are given in the panel titles. The numerical data without the account for radiation damping are depicted by dotted lines, the dashed green curves in panels (b) and (c) display the analytical estimates.

When the electron interacts with a copropagating laser wave, the radiation friction force will induce an additional transverse momentum similar to the case of a counterpropagating wave. However now, at certain initial parameters $a_1 > a_{1\text{min}} \approx 45 \sqrt{1 + (\gamma_0/a_1)^2}$, a distinct acceleration effect will appear. Figure 2, (b) illustrates this situation, where the estimated minimum field amplitude is smaller than the input number a_1 chosen in panel (b). Note that the radiation power decreases in this case. In contrast, the initial γ -factors in panels (a) and (c) of Fig.2 result in numbers $a_{1\text{min}}$, which exceed the input vector potentials. Consequently, we do not find essential electron acceleration here, and the scattered laser power is approximately the same as without radiation friction.

References

- [1] T. Schlegel and V.T. Tikhonchuk, *New J. Phys.* (2012).
- [2] T. Schlegel et al., *Phys. Plasmas* **16**, 083103 (2009).
- [3] L.D. Landau, E.M. Lifshitz, *The Classical Theory of Fields* (Pergamon, New York, 1994).
- [4] E. Esarey, S.K. Ride, P. Sprangle, *Phys. Rev. E* **48**, 3003 (1993).

Vacuum polarization in inhomogeneous fields

L. Roessler^{1,2} and H. Gies^{1,2}

¹Helmholtz-Institut Jena; ²Theoretisch-Physikalisches Institut, Friedrich-Schiller-Universität Jena

The photon polarization tensor provides an effective description of photon propagation in the quantum vacuum. In the presence of external electromagnetic fields, it predicts striking phenomena as vacuum birefringence and dichroism. We have devised a new strategy to compute the polarization tensor in inhomogeneous fields by generalizing worldline numerical methods to computations of correlation functions.

The photon polarization tensor is a central quantity in quantum electrodynamics (QED). It contains information about how light propagates in a background subject to ubiquitous quantum fluctuations. Specifically in electromagnetic backgrounds, the polarization tensor predicts phenomena such as birefringence and dichroism[1]. Whereas for homogeneous electromagnetic fields, the photon polarization tensor at one-loop level is known in integral form, knowledge about this tensor in inhomogeneous fields has so far been inexistent. We have developed new worldline numerical methods to surpass the homogeneous field limitation, and in particular studied birefringence in a spatially inhomogeneous magnetic field [2], see Fig. 1. This field

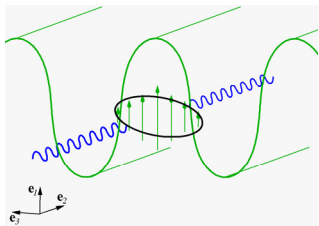


Figure 1: Photon propagation in an inhomogeneous field.

configuration is inspired by the superposition of a strong optical standing-wave laser pulse and higher harmonics in the X- or gamma-ray regime.

The velocity shifts of propagating light now depend on the x_3 coordinate, $\Delta v(x_3)$ to be determined from the eigenvalues of the polarization tensor. In our numerical computations for scalar QED, we use a strong background field $e\bar{B} = 0.2m^2$ superimposed by a spatially oscillating amplitude $B_1 = 0.5\bar{B}$ with oscillation wavelength λ_B . We study the dependence of the velocity shift Δv_{\parallel} on the magnetic oscillation in terms of the phase $\phi = 2\pi x_3/\lambda_B$; $\phi = 0, 2\pi, \dots$ corresponding to photon propagation along the field maxima and $\phi = \pi, 3\pi, \dots$ to minima. In the limit of large $\lambda_B \gg 1/m$, the field becomes slowly varying with respect to the Compton wavelength. Here, the local velocity shifts approach the homogeneous field limits upon insertion of the local magnetic field $B(x_3)$. Near $\lambda_B m \simeq 1$, the field oscillates on the scale of the Compton wavelength, and larger deviations from the “locally-constant-field” ap-

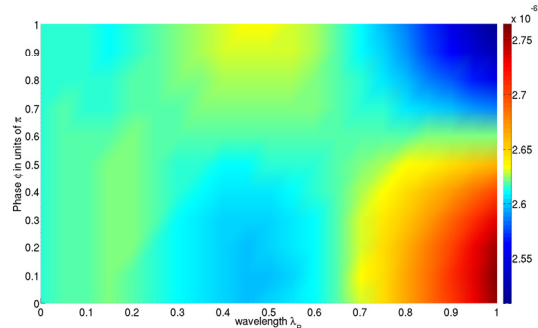


Figure 2: Contour plot of the phase velocity shift Δv_{\parallel} for photon propagation in an inhomogeneous magnetic field along the \vec{e}_2 direction as a function of the field variation wavelength λ_B and the position phase $\phi = 2\pi x_3/\lambda_B$.

proximation become visible, see Fig. 2.

In the worldline picture, the propagating photon undergoing a virtual electron-positron loop with spatial extent $\sim 1/m$ recognizes a magnetic field averaged over a Compton wavelength. This leads to a wash out of the velocity-shift contour with respect to the field inhomogeneities. In the limit of very rapid variations, $\lambda_B \ll 1/m$, the photon thus undergoes a velocity shift induced by the averaged field value \bar{B} , such that $\Delta v \sim \bar{B}^2$.

An interesting observation in the region $\lambda_B m \lesssim 1$ is that the transition from the locally-constant-field limit for $\lambda_B m \gg 1$ to the averaged field limit $\lambda_B m \ll 1$ is not monotonic. For $0.25 \lesssim \lambda_B m \lesssim 0.65$, we observe velocity shift maxima at the field minima and vice versa, see Fig. 2. This can be interpreted as manifestation of the non-local nature of fluctuation-induced properties: e.g., the velocity shift in a field minimum can be dominated by the contributions from nearby maxima if the latter are within the scale of the fluctuation size $1/m$.

We interpret the scale of monotonicity as a critical scale where the self-focussing property of the quantum vacuum turns into defocussing. Our observations thus indicate the existence of a new inherent property of the quantum vacuum which is induced by the nonlinear as well as the non-local properties of quantum fluctuations.

References

- [1] J. S. Toll, Ph.D. thesis, Princeton Univ., 1952 (unpublished); S. L. Adler, *Annals Phys.* **67**, 599 (1971); W. Dittrich and H. Gies, *Springer Tracts Mod. Phys.* **166**, 1 (2000).
- [2] H. Gies and L. Roessler, *Phys. Rev. D* **84**, 065035 (2011) [arXiv:1107.0286 [hep-ph]].

The photon polarization tensor in a homogeneous external field revisited

B. Döbrich^{1,2} and F. Karbstein^{1,2}

¹Helmholtz-Institut Jena; ²Theoretisch-Physikalisches Institut, Friedrich-Schiller-Universität Jena

The photon polarization tensor is the central object in an effective theory for photon propagation in the quantum vacuum. It accounts for the vacuum fluctuations of the underlying theory, and in the presence of external electromagnetic fields, gives rise to such striking phenomena as vacuum birefringence and dichroism. Standard approximations to the polarization tensor for homogeneous fields are often restricted to on-the-light-cone dynamics, and are only limited to certain momentum regimes. We aim at analytical insights into the photon polarization tensor while retaining its full momentum dependence.

Whereas for homogeneous electromagnetic fields, the photon polarization tensor at one-loop level is known exactly in terms of a double parameter integral in momentum space since a long time [1] (cf. also Ref. [2] and references therein), its explicit evaluation still poses an intricate issue.

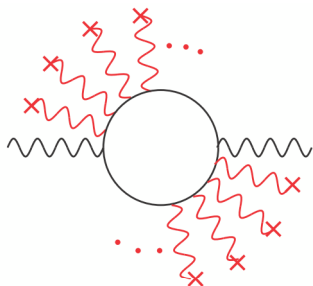


Figure 1: One-loop photon polarization tensor in the presence of a homogeneous external magnetic field indicated by the red wiggly lines ending at crosses.

Apart from the perturbative weak-field expansion, all approximations presently available are manifestly limited to momentum space. This is due to the fact that their derivation involves constraints to a certain momentum regime, whereas the transition to position space by a Fourier transformation requires knowledge about the full momentum range. Novel studies in the framework of QED which come into reach owing to the fast advances in the field of high-intensity laser physics [3], and growing interest in the experimental search for beyond-the-standard-model particles, like minicharged particles [4], strongly necessitate insights beyond these limitations.

In order to achieve this, we have focused on the special case of a pure homogeneous magnetic field \vec{B} [5]. Hence, the only two externally set vectors in the problem are the magnetic field \vec{B} and the wave vector \vec{k} of the probe photons. They govern the entire direction dependence of the polarization tensor.

Our starting point is the proper-time [6] representation of the photon polarization tensor in momentum space.

We first consider the situation where $\vec{k} \parallel \vec{B}$. For this alignment the proper-time integral can be written in terms of a single parameter integral. This is possible following two different strategies, namely either by explicitly carrying out the sum over the Landau levels for Dirac fermions in the presence of the external magnetic field, or by directly evaluating the proper-time integral [7]. The former calculation is valid in the full momentum regime, i.e., in particular also beyond the pair creation threshold. By requiring this result to be reproduced when performing the respective proper-time integral directly, the integration contour of the proper-time integral can be specified unambiguously. Only then the proper-time integral is well defined.

Having established the correct proper-time integration contour, in a second step we turn to the more general situation of $\vec{k} \not\parallel \vec{B}$ [8]. Here, we devise a strong field expansion, applicable beyond the pair creation threshold also. Noteworthy, a factorization with respect to momentum components parallel and perpendicular to the magnetic field vector is encountered here. The resulting expression allows for insights in the full momentum regime. It is amenable to a Fourier transformation, and can in principle also be employed in position space. Thus it is of particular interest in attempts to restrict the available parameter regime for minicharged particles in light-shining-through-walls experiments via “tunneling of the 3rd kind” [4].

Our results can also be applied to a variety of other problems. They are relevant for all kinds of studies concerned with the impact and phenomenology of quantum non-localities onto photon propagation in position space, and thus pave the way to explore diffractive phenomena.

References

- [1] I. A. Batalin and A. E. Shabad, *Sov. Phys. JETP* **33**, 483 (1971).
- [2] W. Dittrich and H. Gies, *Springer Tracts Mod. Phys.* **166**, 1 (2000).
- [3] A. Di Piazza, C. Müller, K. Z. Hatsagortsyan, C. H. Keitel, arXiv:1111.3886 [hep-ph].
- [4] B. Döbrich, H. Gies, N. Neitz and F. Karbstein, arXiv:1203.2533 [hep-ph] and arXiv:1203.4986 [hep-ph].
- [5] W. y. Tsai and T. Erber, *Phys. Rev. D* **10**, 492 (1974) and *Phys. Rev. D* **12**, 1132 (1975).
- [6] J. S. Schwinger, *Phys. Rev.* **82**, 664 (1951).
- [7] F. Karbstein, L. Roessler, B. Döbrich and H. Gies, arXiv:1111.5984 [hep-ph].
- [8] B. Döbrich and F. Karbstein, in preparation (2012).

New constraints on minicharged particles from tunneling of the 3rd kind

*B. Döbrich^{1,2}, H. Gies^{1,2}, N. Neitz^{*2}, and F. Karbstein^{1,2}*

¹Helmholtz-Institut Jena; ²Theoretisch-Physikalisches Institut, Friedrich-Schiller-Universität Jena

We have demonstrated that magnetic fields significantly enhance a new tunneling mechanism in quantum-field theories with photons coupling to fermionic minicharged particles. Based on this scenario, we have proposed a dedicated laboratory experiment of the light-shining-through-walls type, particularly sensitive to minicharged particles with masses in and below the meV regime.

Strong electromagnetic fields have recently become a powerful and topical laboratory probe of fundamental physics. Together with polarimetry experiments, experiments of the light-shining-through-walls (LSW) type have provided the so far strongest laboratory – and thus model-independent – bounds on minicharged particles (MCPs).

The maximum mass sensitivity scale of these experiments is typically set by the frequency scale of the optical probe laser $\sim \text{eV}$, and thus access to a hypothetical new-physics regime of small masses but very weak couplings is granted. Unfortunately the observables of both polarimetric setups and conventional LSW scenarios at best saturate for small MCP masses as the mass parameter m effectively decouples in the limit $m \rightarrow 0$. In contrast, the LSW scenario considered by us [1] does not exhibit this saturation behavior.

Our LSW scenario is based on a new tunneling mechanism in quantum field theory (QFT): here a photon (wave vector \vec{k}) can traverse an impenetrable barrier by virtue of virtual intermediate states that do not couple to the barrier (cf. Fig. 1). As it complements standard quantum mechani-

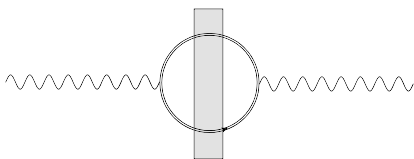


Figure 1: Tunneling of a photon through a barrier mediated by a minicharged particle–antiparticle loop in a magnetic field indicated by the solid double line of the MCP intermediate states.

cal tunneling and classical (on-shell) tunneling in QFT, this phenomenon has been dubbed “tunneling of the 3rd kind” [2]. Notably, it manifestly exploits the fluctuation-induced nonlocal properties of QFT. Whereas current laboratory bounds on MCPs are difficult to improve with tunneling of the 3rd kind at zero field, we have demonstrated that an external magnetic field \vec{B} can significantly amplify the tunneling probability for the case of minicharged fermions. The essence of the phenomenon lies in the existence of

* Now at: MPI für Kernphysik, Heidelberg.

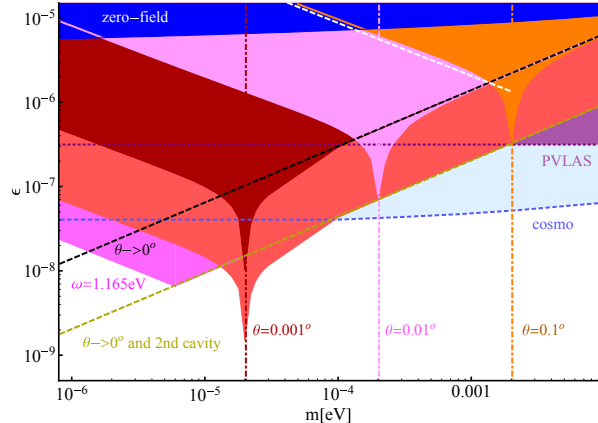


Figure 2: MCP parameter space accessible with tunneling of the 3rd kind and ALPS parameters [3]. At zero field access to the dark blue colored area is granted. The tunneling phenomenon is strongly amplified by a magnetic field (reddish colored areas), and can be further enhanced by the use of a 2nd cavity on the rear side (lowermost light red colored area). The peak structures mark the pair creation threshold for various angles $\theta = \angle(\vec{k}, \vec{B})$. We compare with bounds from PVLAS polarization measurements [4] (purple/dotted line) and the best model-independent cosmological bounds [5] (blue/short-dashed line). Our setup has the potential to outmatch these bounds below $m \lesssim 9 \times 10^{-5} \text{eV}$.

a near-zero mode in the Landau-type energy spectrum of fermionic minicharged fluctuations. As this zero mode is screened only by the MCP mass, the effect increases with a power-law dependence for decreasing MCP mass or increasing magnetic field and approaches a maximum at the pair-creation threshold. Owing to this low-mass enhancement which is unprecedented so far in the context of strong-field physics, a dedicated laboratory experiment involving only present-day technology has the potential to explore a parameter space which so far had only been accessible with large-scale cosmological observations based on CMB data [5] (cf. Fig. 2).

References

- [1] B. Döbrich, H. Gies, N. Neitz and F. Karbstein, arXiv:1203.2533 [hep-ph] and arXiv:1203.4986 [hep-ph].
- [2] H. Gies and J. Jaeckel, JHEP **0908**, 063 (2009).
- [3] K. Ehret *et al.*, Phys. Lett. B **689**, 149 (2010).
- [4] E. Zavattini *et al.* [PVLAS Collaboration], Phys. Rev. D **77**, 032006 (2008).
- [5] A. Melchiorri, A. Polosa and A. Strumia, Phys. Lett. B **650**, 416 (2007).

Relativistic ionization dynamics of highly charged ions

P. Wustelt^{1,2}, T. Rathje^{1,2}, A. M. Saylor^{1,2}, D. Hoff^{1,2}, S. Trotsenko^{1,3}, Th. Stöhlker^{1,3}, G. G. Paulus^{1,2}

¹Helmholtz-Institut Jena, Jena, Germany; ²Institute of Optics and Quantum Electronics, University of Jena, Jena, Germany; ³GSI, Darmstadt, Germany; ⁴University of Heidelberg, Heidelberg, Germany.

The investigation of the behaviour of heavy ions in ultra-intense laser fields is an important aspect of the atomic physics program at FAIR. Of particular interest is the dynamics of ionization in the highly complex setting of multi-photon, multi-electron ionization. So far, most experiments have studied the dependence of the ions charge state distribution on the laser intensity. A major complication in such work has been that ionization in the low-intensity regions of a high-power laser focus contributes strongly to the ion yield, i.e. there exists a severe background problem. In addition, such data cannot provide a detailed picture of the underlying processes.

The goal of this project is to develop and apply novel instrumentation that allows for highly differential measurements and discriminates background events as efficiently as possible. A common characteristic of suitable experimental schemes is that targets with low particle density have to be used. Together with the low repetition rate typical for ultra-intense lasers, this results in the greatest challenge of this project, namely a very low event rate. Our strategy to deal with this problem is to devise several experimental approaches with complementary advantages and disadvantages. For economic reasons, we favor setups that can also be used for university projects with separate funding or have even been built for such projects originally.

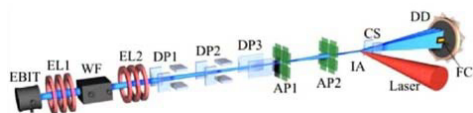


Figure 1: Experimental setup of the ion beam apparatus, which includes an electron beam ion trap (EBIT) or Duoplasmatron (not shown), two Einzel lenses (EL1, EL2), a Wienfilter (WF), three sets of deflector plates (DF1, DF2, DF3), two adjustable pinholes (AP1, AP2), an interaction region (IA), a charge separator (CS), a Faraday cup (FC) and a delay-line detector (DD). The focused laser beam is perpendicular to the ion beams.

The first setup is an ion beam machine [1]. The scheme of the apparatus is shown in Fig. 1. Highly charged ions are produced in an electron beam ion trap/ source (EBIT/EBIS) an accelerated to a few keV kinetic energy. A well-defined beam is formed by several pinholes, electrostatic lenses, and deflection plates. The mass and charge state is selected with the help of a Wien filter. Further on, this ion beam is intersected by the laser beam. As a consequence, the ions are further ionized and slightly deflected towards a time- and position-sensitive (3D) detector. The particular advantage of the approach is that the background gas particles have a statistical distribution of relatively small velocities. Therefore, the corresponding

ionization fragments in general will not reach the detector at the same time as the events of interest, i.e. they can be suppressed very efficiently.

Status of the project: The setup was completed and optimized, aiming on improving the current and uniformity of the ion beam profile.

In addition, a complementary ion source, the so-called duoplasmatron was developed for a production of high intensity ion beams [2]. The advantage of this source is the ability of producing a dense collimated ion beam with ion currents up to several μA . The source consists of two plasma areas, which are confined by an outer magnetic field. A strong electron beam is generated between the cathode and the anode. The intermediate electrode separating the two plasma zones tapers the electron beam, which ionizes the atoms by impact ionization. A rather low energy electrons enable production of low charge states only, however an experiment with this kind of ion beam will still constitute a major step forward for the field. The developed apparatus will allow us to study whether and to which extent non-sequential ionization mechanisms play a role. As sequential ionization – i.e. the ion core will relax to its ground state before the next electron is ionized – is known to dominate, the interpretation of the data expected from the ion beam apparatus calls for establishing the corresponding baseline. Using the semi-classical theory of strong-field ionization, a set of coupled rate equations was used to describe the ionization dynamics. For the first time also the sub-cycle dynamics has been included. We reproduced the known result that at any given energy the charge state distribution is dominated by one or two charge states. In addition, the momentum distribution of the ions is estimated. Taking advantage of including the sub-cycle dynamics, predictions about the influence of the absolute phase of few-cycle pulses on the ionization can be made.

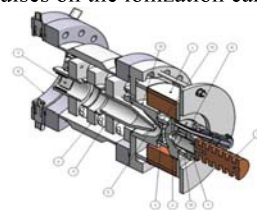


Figure 2: Isometric section of the Duoplasmatron: (1) Cathode, (2) Intermediate electrode, (3) Anode, (4) Magnet, (5) Extraction, (6) Einzel lens, (7) Deflector plates, (8) Gas inlet, (9) Cooling, (10) Isolation, (11) Isolation.

References

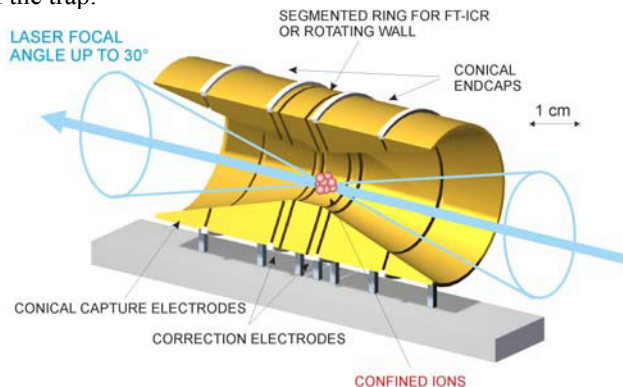
- [1] N.I.Shvetsov-Shilovski *et al*, **PRA** **83** 033401 (2011)
- [2] P.Wustelt, Bachelor thesis, University of Jena, (2011)

A dedicated Penning trap for studies with particles in extreme laser fields

M. Vogel^{1,2}, *W. Quint*^{2,3}, *Th. Stöhlker*^{2,4,5}, *G.G. Paulus*^{4,5}

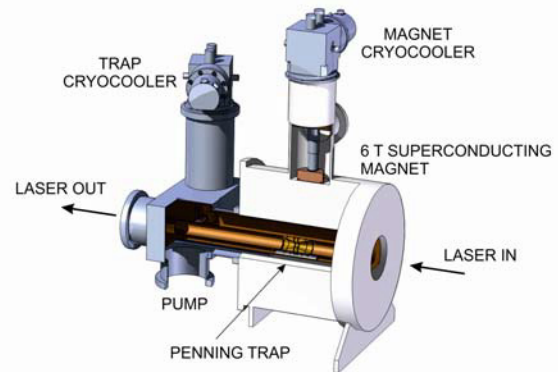
¹ Technische Universität Darmstadt, Germany; ² GSI, Darmstadt, Germany; ³ Ruprecht-Karls-Universität, Heidelberg, Germany; ⁴ Helmholtz-Institut Jena, Germany; ⁵ Universität Jena, Germany

The application of ion confinement techniques at a high-intensity laser opens unprecedented possibilities for the study of non-linear effects in extremely strong fields. Non-destructive ion detection methods with up to single-ion sensitivity extend the experimental capabilities towards a detailed study of multiphoton ionization processes. In the present context, the Penning trap serves as a universal tool for ion confinement and preparation of suitable ion targets for laser irradiation by a multitude of manipulation techniques such as a rotating wall and the use of trap electrodes as 'electric tweezers' for ion target positioning. At the same time, it serves as a detector for broad-band FT-ICR and narrow-band (resonant) mass spectrometry. The presented setup is by design easily adaptable to specific needs at different high-intensity laser facilities. The trap can have conical endcap openings to allow applications with strongly focused lasers without spoiling the trapping field harmonicity and the tunability of the trap.



The interaction of highly intense radiation with matter and the corresponding non-linear effects have been subject of lively research, both theoretical and experimental, especially in the infrared and visible photon energy regimes. Laser systems capable of producing high intensities also at photon energies in the extreme ultra-violet (EUV) and (soft) X-ray regime open access to novel effects like non-linear Compton effects or simultaneous elastic and inelastic photon scattering, and allow multiphoton-ionization experiments in a new domain. Recently, exceptionally strong non-linear photoionization has been observed using high-intensity EUV laser light and been connected with the excitation of collective giant resonances. However, experiments have so far not been able to prepare and investigate well-defined particle ensembles and to non-destructively analyze the reaction products with high accuracy, nor were they able to select or prepare products for further studies in a well-defined way.

We are currently setting up a Penning-trap-based experiment for the investigation of particles interacting with highly intense laser light. The application of specific Penning trap techniques allows to circumvent many problems of earlier studies, particularly by control over the confined particles' density and localization and the use of trap electrodes as 'electrostatic tweezers' for optimized overlap with the laser light.



This also allows experiments with selected and cooled highly-charged ions under well-controlled conditions and is thus of relevance in the frameworks of the HITRAP project at GSI and of the SPARC collaboration and the future FLAIR facilities at FAIR.

As an immediate application example, the FLASH laser at DESY, Germany, is currently capable of producing light with wavelengths down to 4.5 nm (275 eV) in pulses of few fs length with peak powers of around 5 GW and repetition rates of 10 Hz. As a user facility, FLASH is capable of providing light under well-controlled conditions to guest experimental setups like the present one. At a focusing to 100 μ m in the trap centre, FLASH reaches an intensity of around 10¹⁴ W/cm² and allows photoionization studies well in the non-linear regime.

On the side of optical photons at high intensities, an application example is the PHELIX laser at GSI, Germany. With optical photons and intensities up to order 10²¹ W/cm², it covers a somewhat diametric case than for example the FLASH laser, allowing much higher intensities at lower photon energies. This, on the other hand, requires large-scale optics with stronger focusing, hence the large opening angle of the present Penning trap design. Here, typical focal sizes are small and serve as an example where single ion sensitivity is an advantage of a Penning trap.

FLASH and PHELIX allow studies in different regimes of photon energies and intensities. This holds true also for laser systems such as JETI and POLARIS, where also the effect of polarized photons can be studied with the present setup.

Lifetime measurement of the 2^3P_0 state in He-like uranium

R.Reuschl^{1,2,3}, T. Gassner^{1,4}, U. Spillmann¹, A. Bräuning-Demian¹, A. Ananyeva^{1,5}, H. Beyer¹, K.-H. Blumenhagen^{1,4}, W. Chen¹, S. Hagmann⁵, M. Hegewald⁵, P. Indelicato⁶, M. Schwemlein^{1,2,3}, S.Toleikis⁷, M. Trassinelli⁸, S. Trotsenko^{1,9}, D. Winters¹, N. Winters^{1,4} and Th. Stöhlker^{1,9}

¹ GSI, Darmstadt, Germany; ² ExtreMe Matter Institute, Darmstadt, Germany; ³ Frankfurt Institute for Advanced Studies, Frankfurt, Germany; ⁴ Ruprecht-Karls-Universität, Heidelberg, Germany; ⁵ Johann Wolfgang Goethe Universität, Frankfurt, Germany; ⁶ Laboratoire Kastler Brossel, ENS, CNRS, UPMC, Paris, France; ⁷ DESY, Hamburg, Germany; ⁸ INSP, CNRS, UPMC Paris 6, France; ⁹ Helmholtzinstitut Jena, Germany

Up to now, the predictions of quantum electrodynamics (QED) have been found to be in excellent agreement with experimental data. In recent years, considerable progress in the evaluation of higher order corrections has been achieved on the theoretical side - not only for hydrogen- but also for helium-like systems - up to very heavy nuclei. He-like systems are of particular interest since they provide the simplest multi-electron configuration.

For the energy of the ground-state and the 2^3P_2 - state in He-like uranium experimental results have been published [1,2]. Now we are aiming at a more precise determination of the metastable 2^3P_0 state. Its energy can be determined indirectly via its lifetime which has a calculated value of 57.3 ps [3,4]. The 3P_0 state is the longest living among all $n = 2$ excited states and decays via i) an E1M1 transition to the 1^1S_0 state ($\sim 30\%$; $6 \cdot 10^9/s$) and more important via ii) an E1 transition to the 2^3S_1 state ($\sim 70\%$; $1.2 \cdot 10^{10}/s$). This 2^3S_1 state decays promptly to the ground state under emission of a 96 keV photon. By counting the number of 96 keV photons emitted by the swift projectile as a function of the distance from the target-foil, one obtains an exponential decay curve. This curve can directly be attributed to the decay of the 2^3P_0 state if we assume this level to be the only feeding mechanism of the 2^3S_1 state after a given time.

Previous experiments on this meta-stable state have been conducted at the BEVALAC [5] and at GSI [6]; the former providing a value of 54.4 ± 3.4 ps. With a new experimental set-up an improvement of this value to a precision of 1 ps is envisaged. The new energy-, time- and position-sensitive 2D germanium detectors permit a considerable gain in counting statistics. These detectors consist of 128 single strips with a width of 250 μm each. In order to obtain well defined data-points a Soller-slit like collimator of 1 mm thick tantalum sheets with a slit width of 1 mm is placed in front of the detector. Given a crystal width of 32 mm we should be able to measure 15 positions of the decay-curve simultaneously.

In October 2011 we have performed a test experiment with our set-up at the beamline in Cave A. A beam of U^{79+} -ions from the SIS was passed through an Al-stripper at 300 MeV/u producing U^{91+} -ions at an energy of 290 MeV/u. Afterwards the ions passed through a 1.5 mg/cm² nickel foil in our interaction chamber. About 5% of the initially H-like ions undergo electron capture in the Ni-foil, thus forming He-like uranium. Only a very small fraction of the electrons is directly captured into the 3P_0

state, but this level is fed by cascade transitions from higher n-levels. Subsequent to the $2^3P_0 \rightarrow 2^3S_1$ transition, the ground-state transition $2^3S_1 \rightarrow 1^1S_0$ occurs, whose intensity is recorded as a function of the distance from the target-foil (see figure).

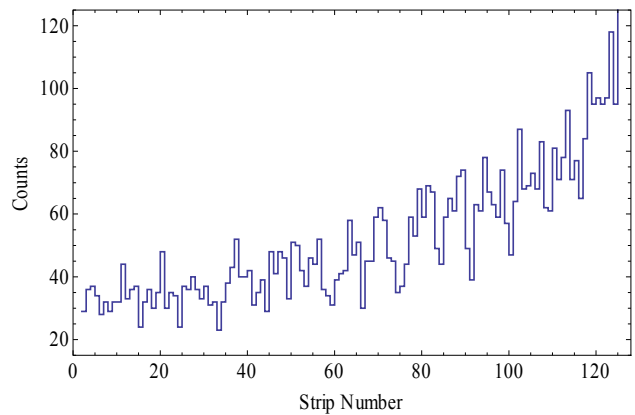


Figure 1: Decay curve measured during the beam-time with a 2D Germanium detector. Strip #125 is closest to the target (~ 5 mm), strip #1 furthest away.

The decay curve covers a span of a little more than two decay-lengths. The spectrum was obtained by applying several conditions on the data. Most important is a coincidence between the recorded x-ray and the down-charged (i.e. He-like) ion. This requires a clear separation of the charge-states behind the dipole magnet. Energy conditions were applied to select the proper transition. The limited beam time did not permit at this time to accumulate sufficient statistics for a precise value, but a preliminary analysis yields a lifetime of 57.4 ± 9.6 ps. The applicability of our method to derive lifetimes with high precision was demonstrated and the set-up is ready for a production run.

References

- [1] A. Gumberidze et al., Phys. Rev. Lett. 92 (2004) 203004-1
- [2] M. Trassinelli et al., EPL 87 (2009) 63001
- [3] W.R. Johnson, D.R. Plante, J. Sapirstein, Adv. At. Mol. Phys. 35 (1995) 255
- [4] G.W.F. Drake, Nucl. Inst. Meth. B 9 (1985) 465
- [5] C.T. Mungler, H. Gould, Phys. Rev. Lett. 57 (1986) 2927
- [6] S. Toleikis et al., Nucl. Inst. Meth. B 235 (2005) 197

The High Voltage Electron Beam Ion Trap (S-EBIT) for SPARC

Y. Ke¹, I. Orban^{1,2}, M. Hobein¹, S. Tashenov¹, S. Trotsenko³, S. Mahmood¹, O. Kamalou¹, A. Safdar¹,
Th. Stöhlker³, H. Zhang¹, and R. Schuch¹

¹Fysikum, Stockholm University, AlbaNova, S-10691 Stockholm, Sweden

²Atomic Physics Division, GSI, Darmstadt, Germany

³Helmholtz-Institute Jena, Jena, Germany

A high voltage Electron Beam Ion Trap “Super EBIT” (S-EBIT) for a 260 keV electron beam energy has been built up at Stockholm University based on the Refrigerated Electron Beam Ion Trap (R-EBIT) [1,2] from “Physics and Technology” (Livermore, USA). This was the first of the next generation EBIT with a refrigerated (dry cryogenic) system where cold heads keep the magnets and heat screens on 4 K and 50 K temperatures, respectively. The electron beam is compressed by a magnet field of max 4T. Singly charged ions can be injected from metal vapor source MEVVA or isotopically cleaned from a high current plasma source CHORDIS for charge breeding. The S-EBIT has a sophisticated extraction scheme with a charge cleaning magnet and a time-of-flight section for charge breeding diagnostics. So far the S-EBIT was used for ion trapping and cooling experiments, electron-ion collisions, and highly-charged ion nanocapillary studies [2-5].



Figure 1: Foto of the assembled S-EBIT.

The upgrade of S-EBIT includes raising the electron energy from 30 keV to 260 keV, installation of a new vibration-free pulse-tube cooler, a new injection, and extraction system (Figs. 1 and 2). We also developed a new operational system for this EBIT in LabView that controls the relevant machine parameters, such as electron beam currents, vacuum, and safety interlocks. This S-EBIT with improved parameters should allow the production of fully

stripped heaviest ions of all elements up to uranium. The machine is now prepared for the possible move to the HITRAP facility and finally to the Helmholtz-Institute Jena to serve as a development platform for SPARC experiments at the future FAIR facility.

Table 1: S-EBIT parameters

Magnetic field	<4 Tesla
Electron beam energy	<260 keV (trap 40kV, gun & collector -220kV)
Electron beam current	<250 mA
Electron beam radius	30 μm
Central current density	<4 kA/cm ²
Trap length	2 cm

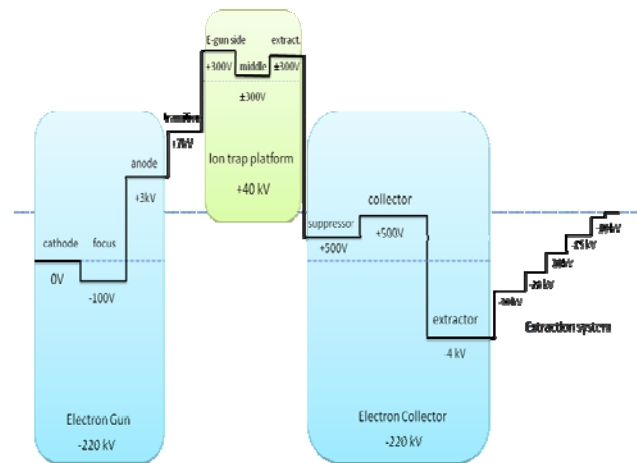


Fig. 2. S-EBIT high voltage scheme (voltage values are the upper limits of the power supplies).

We acknowledge support from the Knut & Alice Wallenberg foundation and the Swedish Research Council VR.

[1] J. McDonald and D. Schneider, NIM B 241, 870 (2005).
 [2] S. Böhm et al., Journ. of Phys. Conf. Series **58**, 303 (2007).
 [3] I. Orban et al., subm. to Phys. Rev. A
 [4] M. Hobein, A. Solders, M. Suhonen, Y. Liu and R. Schuch, Phys. Rev. Lett. **106**, 013002 (2011).
 [5] H. Zhang et al., Phys. Rev. Lett. to be published.

SPARC EXPERIMENTS IN THE HIGH-ENERGY STORAGE RING HESR

Th. Stöhlker^{1,2,3}, C. Dimopoulou³, A. Dolinskii³, T. Katayama³, Yu.A. Litvinov³, R. Maier⁴, D. Prasuhn⁴, M. Steck³, R. Schuch⁵, H. Stockhorst⁴ for the SPARC@FAIR Collaboration
¹ Helmholtz Institute Jena, ² Friedrich Schiller Universität Jena, ³ GSI Helmholtz Center, Darmstadt, ⁴ FZ Jülich, ⁵ Stockholm University

Within the Modularized Start Version (MSV) [1] of the FAIR project [2], the construction of the high-energy storage ring HESR is foreseen. The HESR was originally designed for experiments with stored antiprotons. However, the accelerator facilities, which will be constructed within the MSV, also allow for acceleration, storage and cooling of heavy highly-charged ions [3].

The HESR has a maximum magnetic rigidity of 50 Tm and a circumference of 575 m with two 132 m long straight sections [4]. Corresponding to the operating range of antiprotons which covers magnetic rigidities between 5 and 50 Tm, the HESR can be used to store highly-charged ions in the energy range from 200 MeV/u up to 5 GeV/u. Particularly, the higher energies are not available at any other storage ring facility worldwide. Furthermore, coupling of intense laser beams to HESR is envisaged, which will significantly extend the experimental capabilities. Thus unique conditions will be enabled for conducting precision studies of phenomena like free/bound-state electron-positron pair/multiple-pair creation, laser-assisted electron-ion recombination, laser spectroscopy and laser cooling, electron-capture and ionisation in relativistic collisions, negative continuum dielectronic recombination, and many others.

The planned experiments with ions in the HESR will employ internal targets. Gaseous as well as thin solid, e.g. fiber, internal targets are being considered. The electron cooling system will be used as a target of free electrons. Dedicated transversal electron targets, also for polarized electrons, are in preparation. The targets will be installed in the first part of the arc in the free space, which is available due to the missing dipole concept of the HESR (see Figure 1). Ions that will change their charge state in the target will be detected with particle detectors located, dependent on the required resolution, after the second or the third dipoles of the arc.

To achieve the highest resolution, the cooling of the ion beams is indispensable. In the start-up phase of the HESR, a 2 MV electron cooler [5] will be installed. The electron cooled ion beams will be available at energies from 200 MeV/u to ~3.5 GeV/u. Above 3.5 GeV/u the stochastic cooling will be applied. The inevitable beam heating due to the internal target will be compensated by the cooling. If the energy loss in the target is too large, then a barrier bucket rf system can also be employed.

Estimated beam lifetimes lie in the several ten seconds range even for heaviest gas-targets (e.g. Kr, Xe), which extend to minutes for lighter target atoms. For hydrogen, the target of main interest, the lifetimes increases from ~10 min at the injection energy (~750 MeV/u) to more than 100 min at highest energies.

All these facts show that the high-energy SPARC experiments will be feasible in FAIR [3]. The preparation of a detailed technical design report is presently ongoing.

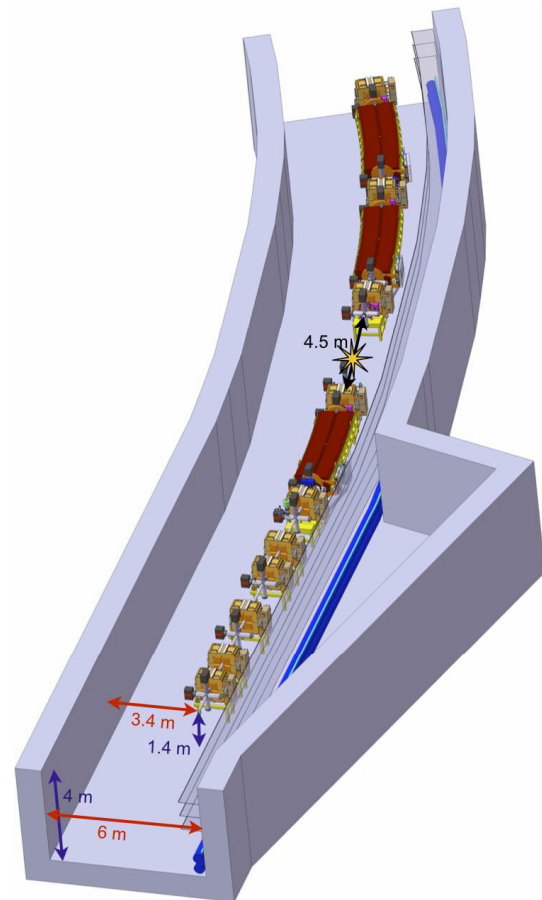


Figure 1. A schematic illustration of one from four arcs of the HESR. The envisioned position of the internal target together with the SPARC experimental installations is indicated with a yellow star. Main dimensions are indicated.

References:

- [1] W.F. Henning (Ed.), International Accelerator Facility for Beams of Ions and Antiprotons, GSI-Darmstadt, November, 2001, <http://www.gsi.de/GSI-Future/cdr/>
- [2] FAIR Green Paper: The Modularized Start Version, Oktober 2009, <http://www.gsi.de/documents/DOC-2009-Nov-124-1.pdf>
- [3] T. Stöhlker et al., SPARC experiments in HESR: A feasibility study, <http://lxcms1.gsi.de/typo3/en/start/fair/>
- [4] R. Maier et al., PAC'11, New York, March 2011, THOCN2, p. 2104 (2011); <http://www.JACoW.org>.
- [5] J. Dietrich et al., COOL'11, Alushta, Ukraine, September 2011, MOIO05, p.15 (2011); <http://www.JACoW.org>.

An x-ray laser beamline to the ESR

V. Bagnoud¹, B. Ecker^{1,2}, U. Eisenbarth¹, S. Götte¹, Th. Kühl^{1,2,3,4}, P. Neumayer^{4,5}, Th. Stöhlker^{1,3,6},
D.F.A. Winters¹, and B. Zielbauer^{1,3}

¹GSI Helmholtzzentrum für Schwerionenforschung GmbH, Darmstadt; ²Johannes-Gutenberg-Universität Mainz;
³Helmholtz Institut Jena; ⁴Extreme Matter Institute (EMMI), Darmstadt; ⁵Goethe-Universität Frankfurt am Main;
⁶Friedrich-Schiller-Universität Jena

Heavy highly charged ions are unique ‘few electron systems’ (1-4 electrons) and therefore ideal candidates for a direct comparison between state-of-the-art atomic structure calculations and high-precision measurements.

The ground state hyperfine structure of heavy hydrogen-like ions has already been measured directly by means of laser spectroscopy at the Experimental Storage Ring (ESR) at GSI [1]. In summer 2011, also the first direct measurement of the ground state hyperfine structure in a heavy lithium-like ion (Bi^{80+}) has been performed at the ESR [2].

The fine structure splitting in heavy Li-like ions could, due to the large transition energies, never be studied with available laser systems. However, with the aid of an X-Ray Laser (XRL), and exploiting the large Doppler shift of the transition wavelength in the ESR, such a laser spectroscopy experiment will be possible. With this technique also other ground state properties of atomic nuclei, such as masses (or binding energies), charge radii, spins and nuclear magnetic moments can be inferred [3].

Since several years an XRL is successfully being operated at the PHELIX facility at GSI [4]. Here, a set of high-intensity laser pulses is used to create a plasma in a solid target and excite electrons in the ionic states to create a population inversion sufficient for laser operation. The wavelength at which lasing occurs can be varied via the target material. Developments for XRL-spectroscopy at the ESR need to establish a compact setup, placed directly underneath the ESR beamline. The target will be pumped by the PHELIX pre-amplifier via a dedicated laser beamline to the ESR hall (see Fig. 1). Detection of the fluorescence from the laser-excited ions will be done in vacuo, using a metal plate (photoelectric effect) and a micro-channel plate.

The unique combination of a heavy ion storage ring and an x-ray laser has great potential, especially for experiments at FAIR. Firstly, a measurement of the $2s_{1/2} \rightarrow 2p_{1/2}$ transition in Li-like holmium ($Z=67$, $\lambda=7.53$ nm) will be attempted at the ESR. This transition was never measured and will require a high ion energy ($\beta=0.73$) and a molybdenum XRL-target ($\lambda=18.9$ nm). On our request, a complete and precise calculation of this fine structure transition in Li-like holmium was made, yielding an energy of $E=164.6207 \pm 0.0254$ eV [5].

An initial study has been performed to determine the feasibility of a first XRL experiment at the ESR. Here, all technical specifications (XRL and ESR) and measurement parameters (timing, detection, etc.) were taken into account. It was found that realistic parameters are: XRL and ion

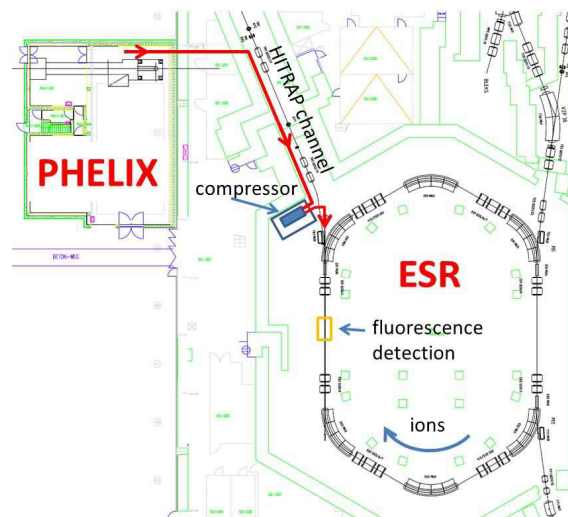


Figure 1: Overview of the two facilities at GSI: PHELIX and ESR. The red line indicates the path of the laser, the blue line that of the ions.

beam diameter 3 mm, 10^{11} XRL photons, 2×10^7 ions, 5% collection efficiency, and 70% detection efficiency. Using these values, we expect to obtain about 30 detected counts per XRL shot on resonance (1 shot per 2 minutes).

The uncertainties in both experiment and theory are of the order of 10^{-4} or less, which implies a similar final uncertainty in the measurement of the transition. The result of this proof-of-principal experiment will thus be a unique, precise, and direct measurement of the $2s_{1/2} \rightarrow 2p_{1/2}$ fine structure transition in a heavy Li-like ion, which is a critical test of state-of-the-art atomic structure calculations in strong fields.

This new and technically challenging project, with many novel experimental features (x-ray lasers and detection), will be carried out in close collaboration with the Helmholtz Institut Jena.

References

- [1] P. Seelig, Th. Kühl *et al.*, Phys. Rev. Lett. **81**, 4824 (1998).
- [2] W. Nörtershäuser, D.F.A. Winters, Th. Kühl *et al.*, GSI beam-time application (2008).
- [3] E.W. Otten, Treatise on Heavy-ion Sciences, D.A. Bromley ed. Vol. 8 (1988), p.515-638 Plenum Press, New York.
- [4] V. Bagnoud *et al.*, Appl. Phys. B **100**, 137 (2010).
- [5] V. Yerokhin, *private communication* (2012).

Cryogenic Current Comparator for FAIR

R. Geithner, F. Kurian*, R. Neubert**, W. Vodel, and P. Seidel**

Helmholtz-Institut Jena, Fröbelstieg 3, D-07743 Jena

**GSI Helmholtzzentrum für Schwerionenforschung GmbH, Planckstraße 1, D-64291 Darmstadt*

***Friedrich-Schiller-Universität, Helmholtzweg 5, D-07743 Jena*

For the recently launched FAIR (Facility for Antiproton and Ion Research) project [1] at GSI Darmstadt an improved Low Temperature dc Superconducting Quantum Interference Device (LTS SQUID) based Cryogenic Current Comparator (CCC) for non-contact monitoring of low intensity particle beams should be developed.

Using SQUID-systems with an extremely low noise level, the sensitivity ultimately depends on the pickup coil with the embedded ferromagnetic core. With the help of the Fluctuation-Dissipation-Theorem (FDT) [2] it is possible to evaluate the noise contribution of the pickup coil. Using the FDT you can calculate the current noise spectral density (PSD_I) from the results of the measurements of the frequency dependent inductance $L_S(\nu)$ and serial resistance $R_S(\nu)$ of coils including these cores with an LCR-Meter.

$$PSD_I = 4k_B T \frac{R_S(\nu)}{(2\pi\nu(L_{SQUID} + L_S(\nu)))^2 + (R_S(\nu))^2} \quad (1)$$

From Equation (1) it could be seen that materials with a high $L_S(\nu)$ and low losses represented by $R_S(\nu)$ lead to a better noise performance. The noise contribution of the cores was also directly measured with a SQUID [3] noise measurement equipment. For both setups a single turn superconducting winding is applied to the cores. To compare the noise measurements with the predictions of the FDT you have to take the input coil of the SQUID sensor L_{SQUID} into account for the calculation. Because there is not any core material in the superconducting input coil of the SQUID the frequency dependence and the serial resistance could be neglected.

The measurements were done in a new wide neck cryostat with an inner diameter of 400 mm and an usable helium level of 860 mm. The operating time is about three days even for large samples.

From preliminary measurements [4] we choose Nanoperm M 764-01[5] as an optimal core material for the improved CCC. To show the improvements of this material at 4.2 K the results are compared to the pickup coil of the DESY-CCC [6]. A four times higher inductance factor which is less frequency dependent is seen for Nanoperm M764-01 compared to DESY-CCC pickup coil with a Vitrovac 6025F [7] core embedded.

From FDT we calculate a three till six time lower current noise for Nanoperm M-764 (see Fig. 1, curve c) compared to the previous DESY-CCC pickup coil with a Vitrovac 6025F core.

The white current noise of such a coil is $2.5 \text{ pA/Hz}^{1/2}$ only and seems to be limited by the SQUID noise (see Fig. 1, curve (d)). The total noise in the frequency range from 20 Hz up to 10 kHz would be reduced by a factor of 3.1 to 28 nA compared to 87 nA for the DESY-CCC pickup coil.

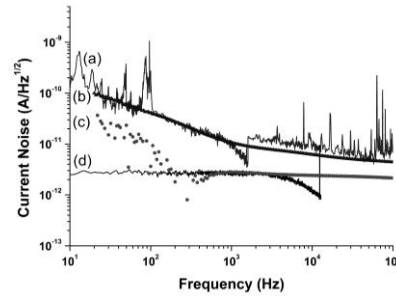


Fig. 1: Measured current noise of the DESY-CCC pickup coil (a) and the SQUID (d) as well as the calculated current noise from FDT of the DESY-CCC pickup coil (b) and Nanoperm M-764 core 2 (c).

The next step is to measure the current noise of the Nanoperm M764 cores and to compare these results with the prediction of the FDT. This will be followed by the characterization of the completed CCC.

The improvements of the noise contribution together with some constructional changes should lead to a 3 times better sensitivity and a much better reduction of the currently seen mechanical interferences [6].

References

- [1] Facility for Antiproton and Ion Research (FAIR), homepage available: <http://www.gsi.de/fair/>
- [2] H.P. Quach, T.C.P. Chui, Cryogenics 44 (2004)6, 445
- [3] W. Vodel, K. Mäkineniemi, Meas. Sci. Technol., 3 (1992), 1155-1160
- [4] R. Geithner et al., Proc. of DIPAC 2011, TUPD66, pp. 458 – 460, Hamburg, Germany
- [5] MAGNETEC GmbH, Industriestrasse 7, D-63505 Langenselbold, Germany
- [6] R. Geithner et al., Rev. Sci. Instrum. 82 (2011), 013302
- [7] VACUUMSCHMELZE GmbH & Co. KG, Gruener Weg 37, D-63450 Hanau, Germany

Publications

P. L. Robinson, R. M. G. M. Trines, J. Polz, M. Kaluza

Absorption of circularly polarized laser pulses in near-critical plasmas

Plasma Physics and Controlled Fusion **53**, 065019, 2011

J. Bromage, J. Rothhardt, S. Haedrich, C. Dorrer, C. Jocher, S. Demmler, J. Limpert,
A. Tuennermann, J. D. Zuegel

Analysis and suppression of parasitic processes in noncollinear optical parametric amplifiers,

Optics Express **19**, 16797, 2011

F. Jansen, F. Stutzki, C. Jauregui, J. Limpert, A. Tuennermann

Avoided crossings in photonic crystal fibers

Optics Express **19**, 13578, 2011

A. Klenke, E. Seise, J. Limpert, A. Tuennermann

Basic considerations on coherent combining of ultrashort laser pulses

Optics Express **19**, 25379, 2011

N. I. Shvetsov-Shilovski, A. M. Sayler, T. Rathje, G. G. Paulus

Carrier-envelope phase effect in the yield of sequential ionization by an intense few-cycle laser pulse

New Journal of Physics **13**, 123015, 2011

V. P. Shevelko, I. L. Beigman, M. S. Litsarev, H. Tawara, I. Y. Tolstikhina, G. Weber

Charge-changing processes in collisions of heavy many-electron ions with neutral atoms

Nuclear Instruments & Methods in Physics Research B **269**, 1455, 2011

A. Willner, F. Tavella, M. Yeung, T. Dzelzainis, C. Kamperidis, M. Bakarezos, D. Adams,
M. Schulz, R. Riedel, M. C. Hoffmann, W. Hu, J. Rossbach, M. Drescher, N. A. Papadogiannis,
M. Tatarakis, B. Dromey, M. Zepf

Coherent Control of High Harmonic Generation via Dual-Gas Multijet Arrays

Physical Review Letters **107**, 175002, 2011

E. Seise, A. Klenke, S. Breitkopf, M. Ploetner, J. Limpert, A. Tuennermann

Coherently combined fiber laser system delivering 120 μ J femtosecond pulses

Optics Letters **36**, 439, 2011

A. Klenke, E. Seise, S. Demmler, J. Rothhardt, S. Breitkopf, J. Limpert, A. Tuennermann

Coherently-combined two channel femtosecond fiber CPA system producing 3 mJ pulse energy

Optics Express **19**, 24280, 2011

I. Hofmann, J. Meyer-ter-Vehn, X. Yan, A. Orzhekhovskaya, S. Yaramyshev

Collection and focusing of laser accelerated ion beams for therapy applications

Physical Review Special Topics-Accelerators and Beams **14**, 031304, 2011

M. Behmke, D. an der Bruegge, C. Roedel, M. Cerchez, D. Hemmers, M. Heyer, O. Jaeckel, M. Kuebel, G. G. Paulus, G. Pretzler, A. Pukhov, M. Toncian, T. Toncian, O. Willi
Controlling the Spacing of Attosecond Pulse Trains from Relativistic Surface Plasmas
Physical Review Letters **106**, 185002, 2011

B. Aurand, S. Kuschel, C. Roedel, M. Heyer, F. Wunderlich, O. Jaeckel, M.C. Kaluza, G. G. Paulus, T. Kühl
Creating circularly polarized light with a phase-shifting mirror
Optics Express **19**, 17151, 2011

B. Marx, I. Uschmann, S. Hofer, R. Lotzsch, O. Wehrhan, E. Förster, M. Kaluza, T. Stöhlker, H. Gies, C. Detlefs, T. Roth, J. Hartwig, G. G. Paulus
Determination of high-purity polarization state of X-rays
Optics Communications **284**, 915, 2011

M. Trassinelli, A. Kumar, H. F. Beyer, P. Indelicato, R. Maertin, R. Reuschl, Y. S. Kozhedub, C. Brandau, H. Braeuning, S. Geyer, A. Gumberidze, S. Hess, P. Jagodzinski, C. Kozhuharov, D. Liesen, U. Spillmann, S. Trotsenko, G. Weber, D. F. A. Winters, T. Stöhlker
Differential energy measurement between He- and Li-like uranium intra-shell transitions
Physica Scripta T **144**, 014003, 2011

A. Willner, F. Tavella, M. Yeung, T. Dzelzainis, C. Kamperidis, M. Bakarezos, D. Adams, R. Riedel, M. Schulz, M. C. Hoffmann, W. Hu, J. Rossbach, M. Drescher, V. S. Yakovlev, N. A. Papadogiannis, M. Tatarakis, B. Dromey, M. Zepf
Efficient control of quantum paths via dual-gas high harmonic generation
New Journal of Physics **13**, 113001, 2011

M. Grech, S. Skupin, A. Diaw, T. Schlegel, V. T. Tikhonchuk
Energy dispersion in radiation pressure accelerated ion beams
New Journal of Physics **13**, 123003, 2011

C. Regan, T. Schlegel, V.T. Tikhonchuk, J.J. Honrubia, J.-L. Feugeas, Ph. Nicolai
Cone-guided fast ignition with ponderomotively accelerated carbon ions
Plasma Physics and Controlled Fusion **53**, 045014, 2011

V. T. Tikhonchuk, T. Schlegel
High-intensity laser plasma interactions and fast ignition
Proceedings SPIE **8080**, 80801G, 2011

N. Petridis, A. Kalinin, U. Popp, V. Gostishchev, Y. A. Litvinov, C. Dimopoulou, F. Nolden, M. Steck, C. Kozhuharov, D. B. Thorn, A. Gumberidze, S. Trotsenko
Energy loss and cooling of relativistic highly charged uranium ions interacting with an internal hydrogen droplet target beam,
Nuclear Instruments & Methods in Physics Research A **656**, 1, 2011

T. Eidam, C. Wirth, C. Jauregui, F. Stutzki, F. Jansen, H.-J. Otto, O. Schmidt, T. Schreiber, J. Limpert, A. Tuennermann
Experimental observations of the threshold-like onset of mode instabilities in high power fiber amplifiers
Optics Express **19**, 13218, 2011

U. Zastra, V. Hilbert, C. Brown, T. Doeppner, S. Dziarzhytski, E. Förster, S. H. Glenzer, S. Goede, G. Gregori, M. Harmand, D. Hochhaus, T. Laarmann, H. J. Lee, K. H. Meiwes-Broer, P. Neumayer, A. Przystawik, P. Radcliffe, M. Schulz, S. Skruszewicz, F. Tavella, J. Tiggesbaeumker, S. Toleikis, T. White

In-situ determination of dispersion and resolving power in simultaneous multiple-angle XUV spectroscopy

Journal of Instrumentation **6**, P10001, 2011

E. Kroupp, D. Osin, A. Starobinets, V. Fisher, V. Bernshtam, L. Weingarten, Y. Maron, I. Uschmann, E. Förster, A. Fisher, M. E. Cuneo, C. Deeney, J. L. Giuliani

Ion Temperature and Hydrodynamic-Energy Measurements in a Z-Pinch Plasma at Stagnation

Physical Review Letters **107**, 105001, 2011

A.V. Brantov, V.Yu. Bychenkov, K.I. Popov, R. Fedosejevs, W. Rozmus, T. Schlegel

Comparative analysis of laser triggered proton generation from overdense and low-density targets

Nuclear Instruments & Methods in Physics Research A **653**, 62, 2011

B. Aurand, J. Seres, V. Bagnoud, B. Ecker, D. C. Hochhaus, P. Neumayer, E. Seres, C. Spielmann, B. Zielbauer, D. Zimmer, T. Kühl

Laser driven X-ray parametric amplification in neutral gases - a new brilliant light source in the XUV

Nuclear Instruments & Methods in Physics Research A **653**, 130, 2011

D. F. A. Winters, T. Kühl, D. H. Schneider, P. Indelicato, R. Reuschl, R. Schuch, E. Lindroth, T. Stöhlker

Laser spectroscopy of the (1s(2)2s2p) P-3(0)-P-3(1) level splitting in Be-like krypton

Physica Scripta T **144**, 014013, 2011

K. S. Schulze, T. Kaempfer, I. Uschmann, S. Hofer, R. Loetzsch, E. Förster

Laser-excited acoustical phonons probed by ultrashort pulses from a laser-driven x-ray diode

Applied Physics Letters **98**, 141109, 2011

A. Gumberidze, S. Fritzsche, S. Hagmann, C. Kozhuharov, X. Ma, M. Steck, A. Surzhykov, A. Warczak, T. Stöhlker

Magnetic-sublevel population and alignment for the excitation of H- and He-like uranium in relativistic collisions

Physical Review A **84**, 042710, 2011

N. I. Shvetsov-Shilovski, A. M. Saylor, T. Rathje, G. G. Paulus

Momentum distributions of sequential ionization generated by an intense laser pulse

Physical Review A **83**, 033401, 2011

G. Weber, H. Braeuning, R. Maertin, U. Spillmann, T. Stöhlker

Monte Carlo simulations for the characterization of position-sensitive x-ray detectors dedicated to Compton polarimetry

Physica Scripta T **144**, 014034, 2011

- S. Haedrich, H. Carstens, J. Rothhardt, J. Limpert, A. Tuennermann
Multi-gigawatt ultrashort pulses at high repetition rate and average power from two-stage nonlinear compression
 Optics Express **19**, 7546, 2011
- F. Stutzki, F. Jansen, C. Jauregui, J. Limpert, A. Tuennermann
Non-hexagonal Large-Pitch Fibers for enhanced mode discrimination
 Optics Express **19**, 12081, 2011
- Y. Nakano, Y. Takano, T. Shindo, T. Ikeda, Y. Kanai, S. Suda, T. Azuma, H. Braeuning, A. Braeuning-Demian, T. Stöhlker, D. Dauvergne, Y. Yamazaki
Observation of intrashell radiative decay of Li-like uranium ($2p(3/2)-2s(1/2)$) using silicon drift detectors
 Physica Scripta T **144**, 014010, 2011
- A. V. Maiorova, V. M. Shabaev, A. V. Volotka, V. A. Zaytsev, G. Plunien, T. Stöhlker
Parity nonconservation effect in resonance recombination of polarized electrons with heavy hydrogen-like ions
 Journal of Physics B **44**, 225003, 2011
- F. Hebenstreit, R. Alkofer, H. Gies
Particle Self-Bunching in the Schwinger Effect in Spacetime-Dependent Electric Fields
 Physical Review Letters **107**, 180403, 2011
- F. Fratini, S. Trotsenko, S. Tashenov, T. Stöhlker, A. Surzhykov
Photon-photon polarization correlations as a tool for studying parity nonconservation in heliumlike uranium
 Physical Review A **83**, 052505, 2011
- D. B. Thorn, A. Gumberidze, S. Trotsenko, D. Banas, H. Beyer, C. J. Bostock, I. Bray, W. Chen, R. DuBois, C. J. Fontes, S. Fritzsche, D. V. Fursa, R. Grisenti, S. Geyer, S. Hagmann, S. Hess, M. Hegewald, C. Kozhuharov, R. Maertin, I. Orban, N. Petridis, R. Reuschl, A. Simon, U. Spillmann, A. Surzhykov, M. Trassinelli, G. Weber, D. F. A. Winters, N. Winters, H. L. Zhang, T. Stöhlker
Polarization and anisotropic emission of K-shell radiation from heavy few electron ions
 Canadian Journal of Physics **89**, 513, 2011
- A. M. Sayler, T. Rathje, W. Mueller, K. Rühle, R. Kienberger, G. G. Paulus
Precise, real-time, every-single-shot, carrier-envelope phase measurement of ultrashort laser pulses
 Optics Letters **36**, 1, 2011
- M. Moeller, A. M. Sayler, T. Rathje, M. Chini, Z. Chang, G. G. Paulus
Precise, real-time, single-shot carrier-envelope phase measurement in the multi-cycle regime
 Applied Physics Letters **99**, 121108, 2011
- T. Eidam, S. Haedrich, F. Jansen, F. Stutzki, J. Rothhardt, H. Carstens, C. Jauregui, J. Limpert, A. Tuennermann
Preferential gain photonic-crystal fiber for mode stabilization at high average powers
 Optics Express **19**, 8656, 2011

S. Keppler, R. Boedefeld, M. Hornung, A. Saevert, J. Hein, M. C. Kaluza
Prepulse suppression in a multi-10-TW diode-pumped Yb:glass laser
Applied Physics B **104**, 11, 2011

A. Buck, M. Nicolai, K. Schmid, C. M. S. Sears, A. Saevert, J. M. Mikhailova, F. Krausz,
M. C. Kaluza, L. Veisz
Real-time observation of laser-driven electron acceleration
Nature Physics **7**, 543, 2011

A. M. Saylor, T. Rathje, W. Mueller, C. Kuerbis, K. Ruehle, G. Stibenz, G. G. Paulus
Real-time pulse length measurement of few-cycle laser pulses using above-threshold ionization
Optics Express **19**, 4464, 2011

L. A. Gizzi, S. Betti, E. Förster, D. Giulietti, S. Hoefler, P. Koester, L. Labate, R. Loetzsch,
A. P. L. Robinson, I. Uschmann
Role of resistivity gradient in laser-driven ion acceleration
Physical Review Special Topics-Accelerators and Beams **14**, 011301, 2011

N. Medvedev, U. Zastra, E. Förster, D. O. Gericke, B. Rethfeld
Short-Time Electron Dynamics in Aluminum Excited by Femtosecond Extreme Ultraviolet Radiation
Physical Review Letters **107**, 165003, 2011

N. G. Johnson, O. Herrwerth, A. Wirth, S. De, I. Ben-Itzhak, M. Lezius, B. Bergues, M. F. Kling,
A. Senftleben, C. D. Schroeter, R. Moshhammer, J. Ullrich, K. J. Betsch, R. R. Jones, A. M. Saylor,
T. Rathje, K. Ruehle, W. Mueller, G. G. Paulus
Single-shot carrier-envelope-phase-tagged ion-momentum imaging of nonsequential double ionization of argon in intense 4-fs laser fields
Physical Review A **83**, 013412, 2011

F. Suessmann, S. Zherebtsov, J. Plenge, N. G. Johnson, M. Kuebel, A. M. Saylor, V. Mondes,
C. Graf, E. Ruehl, G. G. Paulus, D. Schmischke, P. Swrschek, M. F. Kling
Single-shot velocity-map imaging of attosecond light-field control at kilohertz rate
Review of Scientific Instruments **82**, 093109, 2011

A. Kumar, S. Trotsenko, A. V. Volotka, D. Banas, H. Beyer, H. Braeuning, S. Fritzsche,
A. Gumberidze, S. Hagmann, S. Hess, C. Kozhuharov, R. Reuschl, U. Spillmann, M. Trassinelli,
G. Weber, T. Stöhlker
Spectral distribution of the 2S → 1S two-photon transition in atoms and few-electron ions
Pramana-Journal of Physics **76**, 331, 2011

H. Redlin, A. Al-Shemmary, A. Azima, N. Stojanovic, F. Tavella, I. Will, S. Duesterer
The FLASH pump-probe laser system: Setup, characterization and optical beamlines
Nuclear Instruments & Methods in Physics Research A **635**, S88, 2011

M. Baumgartl, B. Ortac, T. Schreiber, J. Limpert, A. Tuennermann
Ultrashort pulse formation and evolution in mode-locked fiber lasers
Applied Physics B-Lasers and Optics **104**, 523, 2011

P. Hansinger, A. Dreischuh, G. G. Paulus

Vortices in ultrashort laser pulses

Applied Physics B-Lasers and Optics **104**, 561, 2011

M. Schulz, R. Riedel, A. Willner, T. Mans, C. Schnitzler, P. Russbueldt, J. Dolkemeyer, E. Seise, T. Gottschall, S. Haedrich, S. Duesterer, H. Schlarb, J. Feldhaus, J. Limpert, B. Faatz, A. Tuennermann, J. Rossbach, M. Drescher, F. Tavella

Yb:YAG Innoslab amplifier: efficient high repetition rate subpicosecond pumping system for optical parametric chirped pulse amplification

Optics Letters **36**, 2456, 2011

J. Rothhardt, S. Haedrich, H. Carstens, N. Herrick, S. Demmler, J. Limpert, A. Tuennermann

1 MHz repetition rate hollow fiber pulse compression to sub-100-fs duration at 100 W average power

Optics Letters **36**, 4605, 2011

J. Rothhardt, T. Eidam, S. Haedrich, F. Jansen, F. Stutzki, T. Gottschall, T. V. Andersen, J. Limpert, A. Tuennermann

135 W average-power femtosecond pulses at 520 nm from a frequency-doubled fiber laser system

Optics Letters **36**, 316, 2011

E. Seise, A. Klenke, S. Breilkopf, J. Limpert, A. Tuennermann

88 W 0.5 mJ femtosecond laser pulses from two coherently combined fiber amplifiers

Optics Letters **36**, 3858, 2011